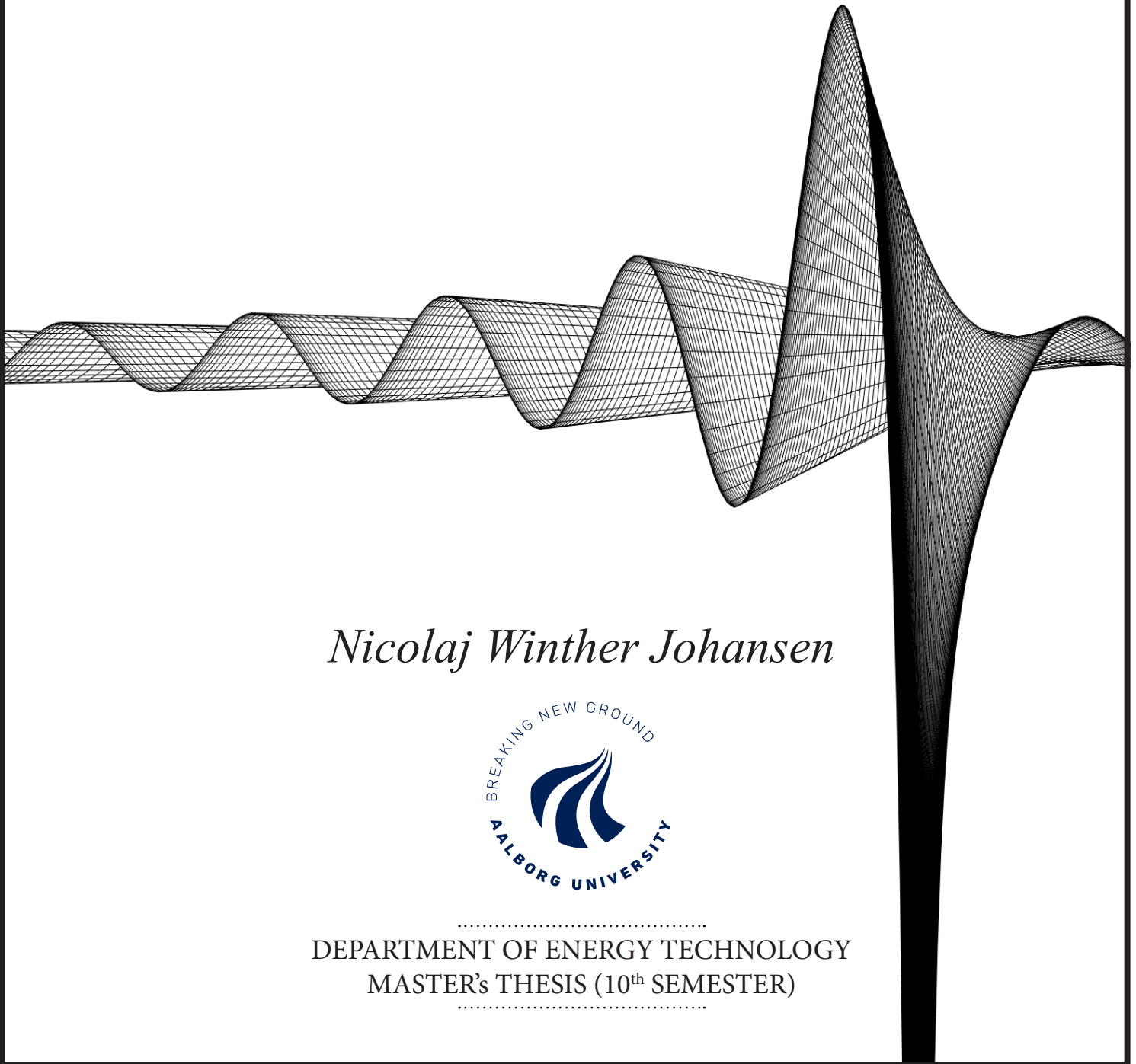


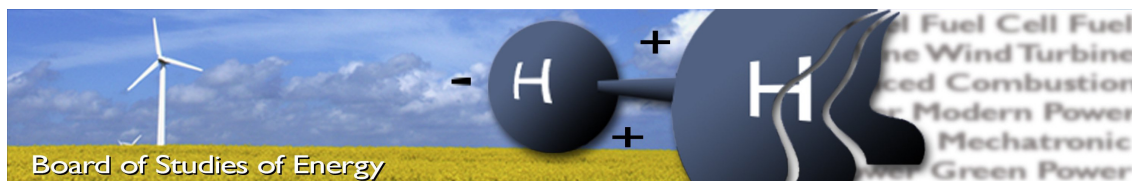
NUMERICAL STUDY OF AN ULTRASONIC MULTI-SCATTERING APPROACH FOR TURBIDITY MEASUREMENTS



Nicolaj Winther Johansen



.....
DEPARTMENT OF ENERGY TECHNOLOGY
MASTER'S THESIS (10th SEMESTER)
.....



Title: Numerical Study of an Ultrasonic Multi-Scattering Approach for Turbidity Measurements

Semester: Mechatronic Control Engineering: 10th Semester

Semester theme: Master's Thesis

Project period: 01.02.17 to 01.06.17

ECTS: 30

Supervisor: Per Johansen

SYNOPSIS:

In this Master's Thesis, a design tool to aid the design of an ultrasonic turbidity sensor has been conducted. A background study has shown that ultrasonic turbidity sensors might be used as an alternative to optical sensors commonly used for turbidity measurements. The benefits of using ultrasonic turbidity sensors have been identified as low maintenance and low cost. The modeling framework for the model-based design tool has been divided into two stages consisting of a CFD and particle tracing simulation and an acoustic simulation. A theoretical background study of a single particle scattering showed that particle size, material type, and ultrasonic wave frequency are primary parameters when anticipating a high scattering signal. It has been found that the particle positions depends greatly on the flow velocity, but that the measurable output signal depends mostly on the particle concentration, particle size, and particle material.

Nicolaj W. Johansen

Pages, total: 105, including
appendices

Appendices: 16 pages

By accepting the request from the fellow student who uploads the study group's project report in Digital Exam System, you confirm that all group members have participated in the project work, and thereby all members are collectively liable for the contents of the report. Furthermore, all group members confirm that the report does not include plagiarism.

Summary

Measuring water turbidity is often performed using high precision optical turbidity sensors, that measures the 90deg scattering of particles in water. One of the main drawbacks using optical sensors is the need for a transparent window into the water. A permanent turbidity measurement setup requires frequent maintenance to clear the window from biofilms and other layers that may obstruct the transparently of the window and potentially obscure the measurements. Ultrasonic sound waves do not require a transparent window and may be used as an alternative.

The standard unit within water turbidity measurements is the nephelometric turbidity unit (NTU), that is a qualitative unit defined from a nephelometric setup. The unit depends mainly on optical parameters like frequency, concentration, material type, shape, and size. The particles in the scope of this project are spherical with a radius of $5\mu\text{m}$ to $10\mu\text{m}$, a concentration of 100 particles per mL to 6000 particles per mL, and with the material property of rigid particles, Silica particles or Polystyrene particles.

The scattering response from an ultrasonic incident wave striking a single spherical particle can be expressed using analytical solutions to the surface boundary condition problem. The amplitude of the scattered wave depends on the frequency of the incident wave, the properties and size of the particle, and the distance from the particle.

The primary object in this project is to examine whether it is possible to create a design tool that can be used in the process of model-based design for a turbidity sensor. The modeling framework of the design tool consists of two main stages. In the first stage, the particle positions within a given sensor geometry are calculated utilizing CFD and particle tracing simulations. The second stage consists of an acoustic frequency simulation, simulating the scattering field from the particle distribution calculated in the first stage.

Due to a large numerical problem, the required frequency of the incident wave is lowered from 10MHz to 2MHz which, as a consequence, decreases the numerical problem but also reduces the particle multi-scattering amplitude. It is, however, found that upscaling the particle size can approximate the scattering amplitude of the original frequency with a 5% error assuming rigid particles and a minimum average distance between the particles of ten times the diameter of the particle.

Using the design tool, different sweeps of parameters has been investigated. It has been found that the RMS multi-scattering amplitude as a function of the particle concentration (particles per mL) scales with a one term power fit (Confidence level of $R^2 = 0.99$).

Also, the RMS multi-scattering amplitude using different material properties has been investigated, which can be seen in Figure 1.

The design tool has also been proven useful for visualization of the scattering pressure

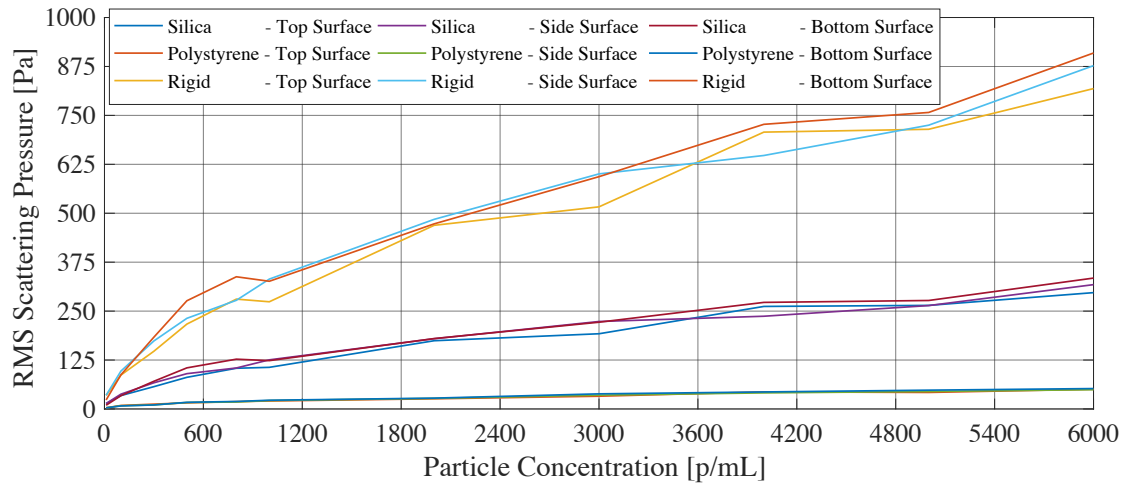


Figure 1. The average RMS scattering pressure on the top, side and bottom surface as a function of the particle concentration using the particle materials Silica, Polystyrene and rigid. The particle radius is $a = 5\mu\text{m}$ and the flow inlet velocity is 1m/s .

field. In Figure 2 the RMS scattering pressure can be seen for a particle concentration of 100 particles per mL and 6000 particles per mL.

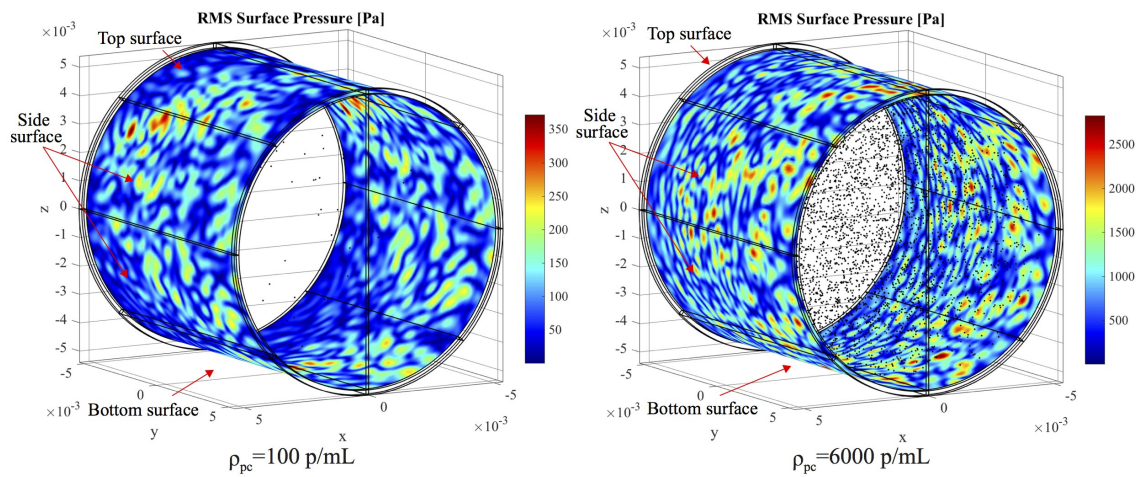


Figure 2. 3D mirrored acoustic solution-set with the RMS scattering pressure field on the outer fluid domain surfaces. The particle concentrations seen is 100 p/mL and 6000 p/mL, and an inlet flow velocity of 1m/s . Particles are assumed rigid and with a particles radius of $a = 5\mu\text{m}$.

Preface

This Master's Thesis within Mechatronic Control Engineering has been submitted to the Department of Energy Technology at Aalborg University in the spring semester 2017.

The project is the summit of experiences and knowledge gained during the Master program. Important issues such as reliability and diagnosis of hydraulic machines have been of particular interest throughout the master program. Ultrasonic methods have been investigated as a non-destructive way of detecting events that can influence the reliability of hydraulic machines, leading to this project.

Acknowledgment

I would like to thank my supervisor Per Johansen for the many inspiring discussion about the project and various other intriguing topics. I would also like to thank Sune Dupont and Jens Lykke Sørensen from Kamstrup A/S for the opportunity of working with the turbidity sensor. Also, special thanks go to Sergey Sorokin for the discussions about complex topics within wave theory.

Reader's Guide:

A list of the literature used in this report can be found in the bibliography on page 107, by the following format:

{ Author(s) (Year), *Title*, Publisher, Edition, ISBN, URL }

ISBN and URL are presented where applicable and available. The bibliography is sorted alphabetically by the surname of the first author and citations is given as: [Author's surname (et al.), Year, Page X]

For referencing figures, equations and tables in the report, they are numbered in the following manner: $(x.y)$, where x indicates the chapter and y indicate the number of the figure, equation or table. In addition, relevant captions for figures and tables can be found below the figure or table.

Bold variables denote vector notation, and bold capital letters denote matrices.

A number of appendices are included in this report, and they can be found subsequent the bibliography.

The software used in this project has primarily been COMSOL Multiphysics 5.2a/5.3, MATLAB, Maple and SolidWorks. Relevant COMSOL model files, Matlab scripts and digitally available literature cited in this project is submitted digitally together with the report.

NOMENCLATURE AND ABBREVIATIONS

Abbreviations

DoF	Degrees of Freedom
NoP	Number of Particles
NTU	Nephelometer Turbidity Unit
PML	Perfectly Matched Layers, used in the acoustic simulations to truncate the domain
SSC	Suspended Solids Concentration
UT	Ultrasonic Turbidity (UT) sensor

Nomenclature

γ	Separation Constant, used in the determination of the scatter wave
\hat{p}	Pressure peak amplitude
λ_0	Wavelength $\lambda_0 = c/f_0$
\mathbf{F}_D	Particle drag force
\mathbf{u}	Fluid velocity
\mathbf{v}	Particle velocity
\mathbf{x}	Particle position
μ	Fluid dynamic viscosity
∇	Gradient operator
∇^2	Laplace operator
ν	Fluid kinematic viscosity
ω	Angular wave frequency
ϕ	Spherical angle
ρ	Fluid density
ρ_0	Ambient density
ρ_{pc}	Particle concentration
ρ_{release}	Non-dimensional density proportionality factor for the particle release distribution
ρ_{total}	Total density
ρ_d	Disturbed density
ρ_p	Particle density
τ_p	Particle velocity time constant

\mathbf{v}_0	Ambient acoustic velocity vector. Assumed to be $\mathbf{v}_0 = \mathbf{0}$
$\mathbf{v}_{\text{total}}$	Total acoustic velocity vector
\mathbf{v}_d	Disturbed acoustic velocity vector
θ	Spherical angle
Re	Reynolds number
Re_r	Relative Reynolds number calculated using the absolute velocity difference $\mathbf{u} - \mathbf{v}$
A	Plane wave pressure amplitude
a	Particle radius
A_{in}	Inlet cross section area for the fluid flow model
A_{tube}	Measurement tube cross section area for the fluid flow model
a_s	Scaled particle radius
c	Speed of sound
C_n	Scatter wave coefficient
D_{hyd}	Hydraulic diameter used in the calculation of the Reynolds number
D_{in}	Inlet diameter
D_n	Flaw wave coefficient
d_p	Particle diameter
$h_n^{(1)}$	Hankel function of the first kind
j_n	Bessel function of the first kind
k	Wave number, given as $k = \omega/c$
l	Separation constant, used in the determination of the analytical scatter wave solution
L_{inlet}	Inlet domain length
L_h	Hydrodynamic entry length
m	An integer used in the determination of the scatter wave
m_p	Particle mass
N	Mesh scaling factor
n	An integer used in the determination of the scatter wave
N_{release}	Number of particles per release
n_n	Bessel function of the second kind
p	Time harmonic pressure disturbance $p = \hat{p} e^{ikr} e^{-i\omega t}$
p'	Complex pressure function
p_0	Ambient pressure
p_{flaw}	Flaw pressure disturbance $p_{\text{flaw,total}} = p_{\text{flaw},0} + p_{\text{flaw}}$
p_{inc}	Incident plane wave pressure disturbance ($p_{\text{inc,total}} = p_{\text{inc},0} + p_{\text{inc}}$)
p_{rms}	RMS pressure calculated as $p_{\text{rms}} = \sqrt{\frac{1}{2} p^* p}$
$p_{\text{sc},s}$	Scaled scatter pressure
p_{sc}	Scattering pressure disturbance ($p_{\text{sc,total}} = p_{\text{sc},0} + p_{\text{sc}}$)
p_{total}	Total pressure
p_b	Pre-known analytical expression of the background pressure field

p_d	Disturbed pressure
P_n	Legendre polynomials
p_t	Total pressure field in the numerical acoustic simulations
r	Spherical coordinate
R_{in}	Inlet radius
t	Time
t_{release}	Time between particle releases
t_{sim}	Particle tracing simulation time
U_0	Average inlet flow velocity
U_{tube}	Average measurement tube flow velocity for the fluid flow model
V_{inlet}	Inlet release volume
H	Length of the cylinder in the acoustic geometry
L	Thickness of the PML domain
R	Radius of the cylinder in the acoustic geometry

CONTENTS

Nomenclature and Abbreviations	ix
1 Introduction	1
1.1 Turbidity in Water	2
1.2 Using Ultrasound for Turbidity Measurements	3
1.3 The Main Concept	5
2 Background Analysis	9
2.1 Model Based Design	9
2.1.1 The Ultrasonic Turbidity Sensor Prototype	10
2.2 Governing Equations of Linear Acoustics	12
2.2.1 Acoustic Scattering from a Sphere	13
2.2.2 Far-Field Approximation	19
3 Problem Statement	21
3.1 Conditions for the Simulations	22
4 The Model Structure	23
5 Fluid Flow and Particle Tracing in the Sensor	25
5.1 Geometry Refinement	26
5.2 Flow Model	27
5.2.1 The RANS model	28
5.2.2 Turbulence Models	28
5.2.3 Meshing for Fluid Flow	30
5.2.4 Boundary Conditions	31
5.2.5 Solver for the Fluid Flow Problem	32
5.2.6 Results from Fluid Flow Model	33
5.3 Particle Tracing	35
5.3.1 Particle Release Strategy	38
5.3.2 Particle Tracing Results	41
6 Computational Acoustics	45
6.1 The Acoustic Frequency Domain Model	48
6.2 Analysis of Numerical Scattering	48

6.2.1	Meshing the Acoustic Domain	49
6.2.2	Perfectly Matched Layers	53
6.2.3	Solver Selection for the Acoustic Calculation	59
6.3	Particle Distribution and Acoustic Geometry Generation	61
6.3.1	Acoustic Domain and Particle Coordinates	61
6.4	Mesh in the Final Model	65
6.5	Scaled Scatter Solution	66
7	The Combined Simulation	73
7.1	Results from The Combined Simulation	75
8	Conclusion	83
9	Discussion and Future Work	87
A	Mathematics for the Derivation of the Scattering Problem	89
A.1	The Derivation of the Scatter Field Coefficients	89
A.2	Properties and Background for the Bessel functions, Hankel functions and Legendre functions	90
A.3	Some Useful Asymptotics	92
B	Geometry Simplification and Mesh Convergence for Flow and Particle Simulations	93
C	Flow Inlet Model	95
D	Relative Reynolds Number for Particle Tracing	97
E	Investigation of Mesh for Acoustic Simulations	99
F	Scripts and Algorithms	101
F.1	Particle Coordinate Selection Function	101
F.2	Acoustic Particle Geometry Generation Algorithm	101
F.3	Particle-Particle Interaction Analysis	103
	Bibliography	105

INTRODUCTION

Measuring the particle concentration in fluids is used in a broad range of industries including food process industry, system diagnosis, and water quality monitoring. In the food process industries is the cloudiness of the fluid used as a vital part of the process quality control. For example, it is important that the visual appearance and cloudiness of juice remain constant and tightly control for consumer acceptance [Linke & Drusch, 2016]. Equal criteria can be found within beverage industries [Bratby, 2015].

Within hydraulic fluid-power applications, particle contamination is known to be one of the leading causes of wear and failures [Fitch, 2011]. Hydraulic systems are often circulating closed systems, with high pressures and tight tolerances, and even small particles in the oil may, therefore, have a pronounced impact. Particle contamination in hydraulic machines can be a result of external pollution of dust and dirt or internal surface degradation. Internal degradation can be caused by friction and surface removals from particle plowing or cutting, which then leads to even higher particle contaminations in the system and therefore, even more, friction and more surface removal. The high particle contamination can then lead to an unexpected breakdown of essential components like electro-hydraulic valves that are blockaded due to small deposits of particles in pilot lines or a direct blockade of the spool [Fitch, 2011]. The measurement of particles within hydraulic components can, therefore, be an important part of the reliability and diagnosis of the system. A condition monitoring approach using particle concentration measurements can be seen in Figure 1.1.

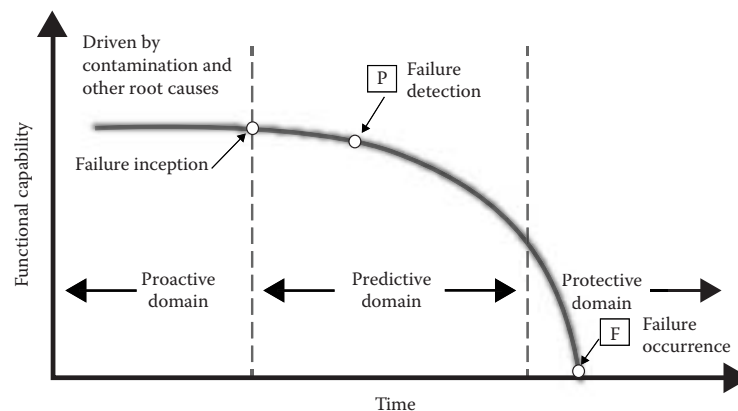


Figure 1.1. Monitoring the particle contamination level in hydraulic components may increase the reliability of the system and potentially reduce the downtime [Fitch, 2011].

Real-time detection of particle levels in hydraulic systems may even minimize the downtime and increase the lifetime of the system by intelligently executing an oil flooding procedure at an early stage when a certain contamination level is intercepted.

Water quality is an area that is of increased interest both in the US and EU [Kamstrup, 2014]. The water quality can be quantified through the degree of particle contaminations in the water with particles of sizes varying from a few nanometers to several millimeters. The large span in size makes it significantly challenging for water treatment engineers, to measure the particles [Bratby, 2015].

Real-time measurements of particle concentrations in utility water distribution network can also be used as an early-warning system, detecting polluted water before it reaches the end-user. Polluted water in the water distribution network can be a result of a broken pipeline or water flooding after a large rainfall where the waste water is mixed with the utility water. Particles from natural weathering may consist of a large variety of materials, among iron, silica, aluminum, clay and other minerals [Bratby, 2015]. The particles can also comprise of organic matter or algae fastened on the surface of existing mineral particles.

Stringent wastewater policies demand better characterization of the water contamination levels in sewer systems, and only a few existing monitoring techniques can be used in real-time [Pallarés et al., 2016; Abda et al., 2009].

Particles in water are often measured as total suspended solids or Suspended Solids Concentration (SSC) using a rinsed membrane with a known dry weight [Bratby, 2015]. Drying the membrane and the particles deposited on the membrane can be measured. Even though this method is simple, it has some significant drawbacks. The particle measurement is affected by the pore size of the membrane allowing smaller particles than the pore size to pass. Also, the particle mass removed in the drying of the membrane may result in erroneous measurements. But most of all, the method is rigorous, time-consuming and cannot be conducted real-time. Measurement of particle concentrations using optical scattering methods is often called turbidity measurements, which is described in the following.

1.1 Turbidity in Water

Turbidity is a quantitative measure of the water cloudiness, which from modern standards are defined by 90-degree light scattering of suspended solids. The original definition of turbidity was developed in early 1900, where the measurement unit was identified as x parts per million suspended silica in purified water [Sadar, 1999]. Because the unit did not relate to a specific matter in the sample, the unit where referred as Turbidity Unit (TU) [Sadar, 1999]. The apparatus that is associated with the measurement of turbidity is called a nephelometer why the standard unit for turbidity is referred as NTU [ISO

Standard, 2016]. A schematic of the apparatus can be seen in Figure 1.2.

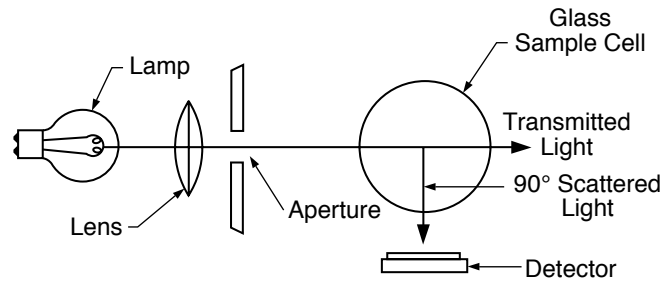


Figure 1.2. Schematic of the nephelometer to measure turbidity [Sadar, 1999]

Figure 1.2 shows the idea behind the turbidity measurement. A light beam propagates through the sample, which then scatters when the light strikes the particles in the sample. The scattered light is then measured at a 90 deg angle from the sample, as seen in Figure 1.2. The 90-degree measurement angle is chosen because the light scattering intensity in the 90-degree direction from the incident light beam is least sensitive to particle size variations in the sample [Bratby, 2015]. The particles can be in the form of suspended solids like sand, clay or organic matter, as described in the introduction. The measure of turbidity is, therefore, highly dependent upon properties like wavelength, particle size, particle shape, and other optical properties that influence the light scattering. Due to a large number of variables found in turbidity measurements, it is difficult to conduct a direct comparison between measurements taken with various samples and with different types of equipment [Sadar, 1999].

In the pursuit of obtaining a robust calibration method for turbidity sensors, a Formazin polymer suspension was proposed in 1926 and, again, in the 1960's [Sadar, 1999]. The Formazin suspension was found stable and reproducible enough to meet the requirements of a primary standard and have since been the standard for turbidity measurements. A Formazin suspension created by 0.5g/40mL hydrazine sulfate and 5g/40mL hexamethylenetetramine in 40mL water is by the standard ISO-7027-1 defined as 4000 NTU [ISO Standard, 2016].

1.2 Using Ultrasound for Turbidity Measurements

There can be found a large variety of precise optical turbidity instruments that can be used for real-time turbidity measures. Common for the optical turbidity sensors is, however, that they require a transparent detector window and fluid. Figure 1.3 shows an optical turbidimeter used for larger particles where the light is emitted to the sample with a 45-degree angle and a pair of photoreceptors at 90-degree and 140-degree are placed to intercept scattered signals from the particles. The sensor does also have a wiper to clean the window face from biological growth and dirt.

This kind of sensor can be used out of the laboratory, but is expensive, limited by mechanics in the fluid, and may require frequent service.

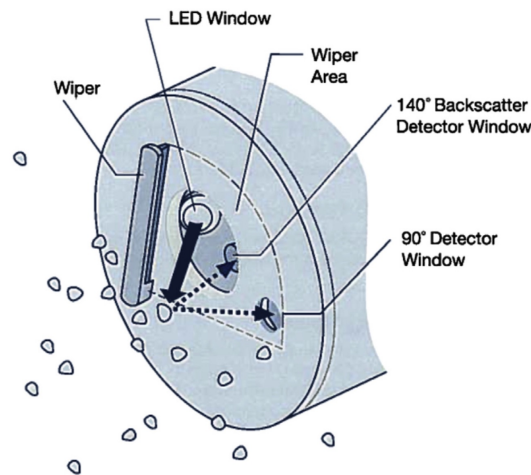


Figure 1.3. Schematic of an optical turbidimeter for large solids, with window wiper. [Bratby, 2015]

An alternative to the optical turbidity measurement methods is to use ultrasonic waves.

Only a small amount of literature can be found in the field of ultrasonic turbidity measurements. An ultrasonic device for real-time particle concentration measurement was presented in the study by Abda et al. [2009]. The instrument described in Abda et al. [2009] conducts measurements of fluid height, fluid velocity and particle concentrations in sewers and rivers. The sensor consists of three ultrasonic transducers, as seen in Figure 1.4.

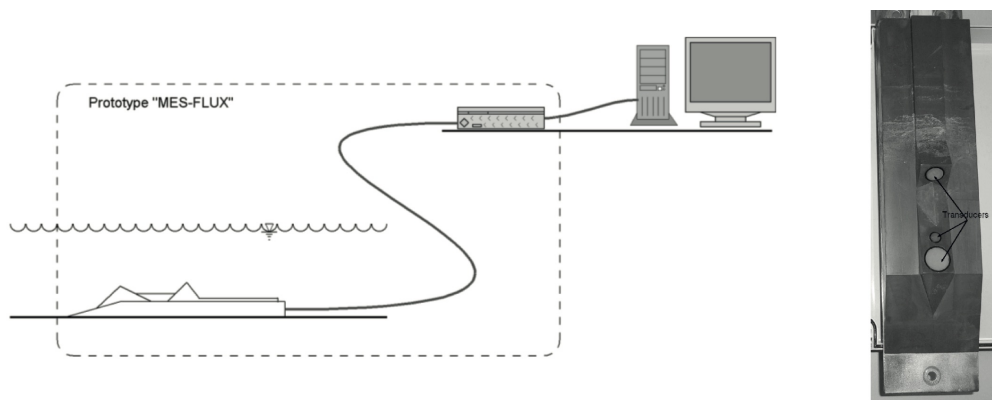


Figure 1.4. Schematic of an Ultrasonic particle concentration sensor. (Figure modified from Abda et al. [2009])

The larger transducer is a 1.8MHz broadband transducer to measure the monostatic velocity and water height. This transducer is placed with a slope of 75deg in the direction of the fluid stream, which increases the Doppler frequency that is used to measure

the flow velocity. A second sensor is oriented equally with the larger transducer and with a mean frequency of 9.2MHz, and the third transducer is a 4.5MHz transducer oriented 70deg towards the other transducers. The second and third transducer is used to measure the particle concentration in the fluid. The study shows that the particle concentration measurements in a wastewater collector follow rain events as expected, but actual verification of the measurement precision was not presented in Abda et al. [2009].

A similar device called UB-Flow F-135 profiler by Ubertone is presented in Fischer [2009]. The UB-Flow F-135 profiler has two transducers of 1.5MHz and 6MHz respectively. This frequency range matches a broad range of particle sizes, starting from 30 μm [Fischer, 2009]. The study concludes that the device can measure turbidity in the form of a turbidity ratio or turbidity profile. Another UB-Flow profiler by Ubertone can be found in Pallarés et al. [2016], where the acoustic turbidity was related to both SSC and NTU as seen in Figure 1.5.

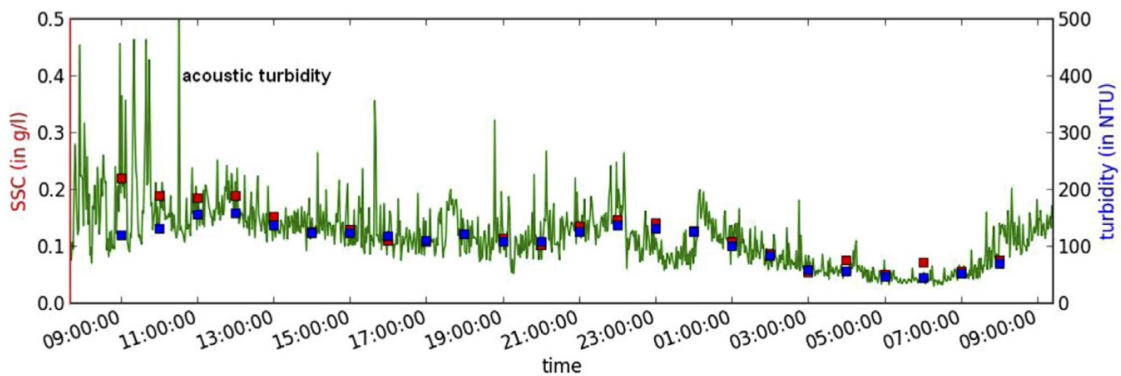


Figure 1.5. Acoustic turbidity as a function of time together with SSC measurements conducted using classical sampling and analyzing methods and the turbidity in NTU measured using an optical HACH turbidimeter [Pallarés et al., 2016].

The ultrasonic turbidity sensor in the scope of this work is primarily focused on the measurement of particle contaminations in utility water distribution systems.

1.3 The Main Concept

The Danish company Kamstrup A/S are developing a robust, sensitive and low-cost ultrasonic turbidity sensor [Kamstrup, 2014]. The main idea is to develop an acoustic turbidity sensor using the technology of existing ultrasonic flow velocity sensors. This ultrasonic turbidity sensor is the key focus of this work.

An ultrasonic flow velocity sensor uses the time it takes for a wave pack to travel from the transmitter (Tx) to the receiver (Rx₁) as illustrated in Figure 1.6.

Reversing the receiver to transmit ultrasonic wave packs in the counter flow direction, makes it possible to calculate the flow velocity without knowing the speed of sound in the

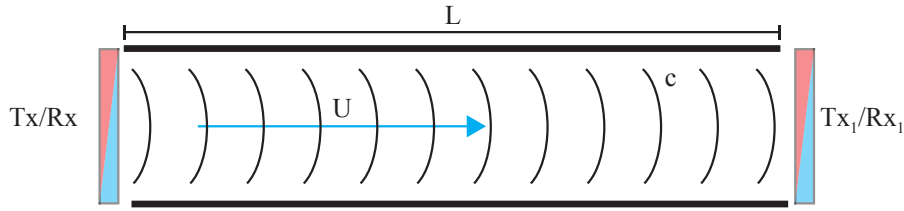


Figure 1.6. Main concept of ultrasonic flow velocity sensor

fluid c and the resulting expressions are simply two equations with two unknown:

$$c + U = \frac{L}{\Delta t_1} \qquad c - U = \frac{L}{\Delta t_2} \qquad (1.1)$$

$$U = \frac{L(\Delta t_2 - \Delta t_1)}{2\Delta t_1 \Delta t_2} \qquad c = \frac{L(\Delta t_2 + \Delta t_1)}{2\Delta t_1 \Delta t_2} \qquad (1.2)$$

where Δt_1 is the wave travel time from Tx to Rx₁, Δt_2 is the wave travel time from Tx₁ to Rx, L is the traveling length and c is the speed of sound in the fluid, that is temperature and pressure dependent.

Contaminated water that contains particles with an acoustic impedance different from the acoustic impedance of the fluid medium itself scatters waves when exposed to an acoustic background field. Adding an extra sensor Rx₂ in the middle section (see Figure 1.7) allow the scattering field to be measured, from which it is expected that the turbidity of the fluid can be calculated.

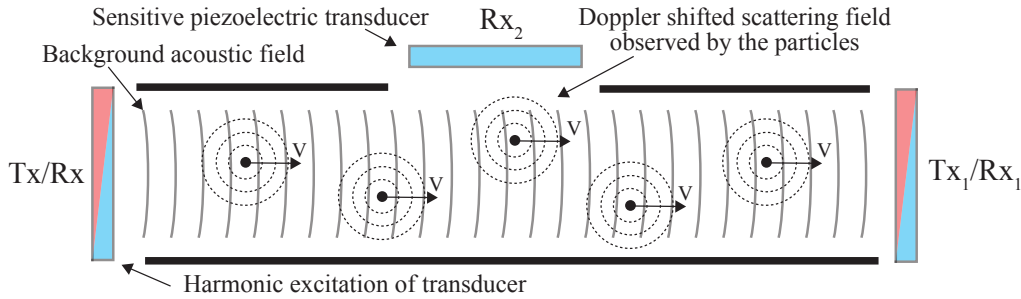


Figure 1.7. Schematic of particles scattering in a background acoustic field. Due to the relative movement of the particles in the stationary background field, the frequency observed by the particles is Doppler shifted.

If the particles are moving in the fluid, the scattering field is frequency shifted relative to the background field. This is due to the relative motion of the particles, and the speed of sound called a Doppler shift. A schematic of the particle scattering waves, observed from the perspective of the particles can be seen in Figure 1.7.

Assuming that the particles are moving in a subsonic homogeneous medium, the frequency of the background field f_b can be expressed in terms of speed of sound c and wavelength λ , by $f_b = \frac{c}{\lambda}$. The frequency observed by the particle can, likewise, be expressed as:

$$f_{sc} = \frac{c - V}{\lambda} = f_b \left(1 - \frac{c}{V}\right) \qquad (1.3)$$

where V is the velocity of the particle, and the negative sign is due to the movement in the direction away from the source.

The scattered waves of the moving particles are also Doppler shifted observed from the perspective of the receiver Rx_2 (see Figure 1.8).

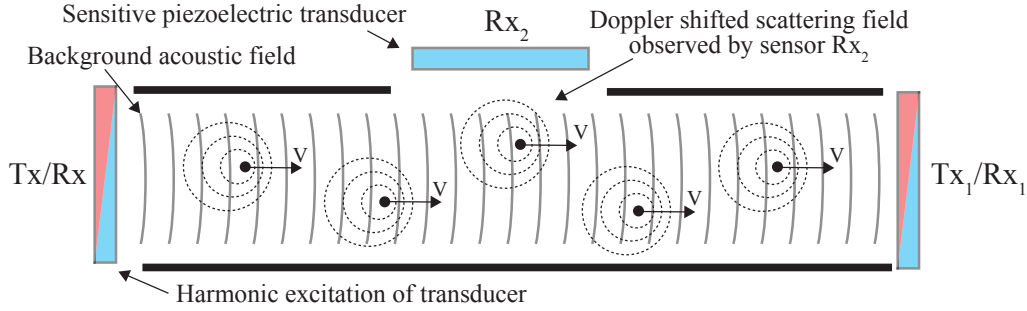


Figure 1.8. Schematic of particles scattering in a background acoustic field, observed from the transducer Rx_2

If the particle movement is assumed to be parallel to the flow direction, the relative velocity observed by the receiver can be expressed in terms of the angle between the sensor and the moving particle can be found as $V \cdot \cos(\theta)$. The Doppler shifted frequency of the scattered particle, observed by the receiver Rx_2 , can be calculated as:

$$f_r = \frac{c + V \cdot \cos(\theta)}{\lambda} = f_{sc} \left(1 + \frac{V \cdot \cos(\theta)}{c} \right) \quad (1.4)$$

where f_r is the Doppler shifted scatter frequency, and θ is the angle between the axis of the particle movement and the receiver Rx_2 .

In this work is it, however, assumed that the receiving transducer Rx_2 is only available to measure waves that travel perpendicular to the transducer [Kamstrup, 2017a]. Thus, only 90-degree waves can be observed by the transducer Rx_2 and Equation 1.4, therefore, reduces to $f_r \approx f_{sc}$.

The signal measured by the transducer Rx_2 contains both the signal from the background wave and the scattered wave. The frequency shift in the scattered wave makes it, however, possible to separate the scattered wave from the background wave through frequency analysis. Thus using this method only the scattering wave from moving particles can be measured.

Initial Statement

The preceding leads to the following initial statement: *How can the presented ultrasonic turbidity sensor be designed and what parameters are critical regarding the acoustic scattering?*

BACKGROUND ANALYSIS

This chapter contains some of the main ideas behind model-based design and a thorough description of the leading physics behind the ultrasonic turbidity sensor. Also, the classical theory of acoustic scattering is described in this chapter.

2.1 Model Based Design

Mechatronic sensors like the ultrasonic turbidity sensor described in the introduction, are sophisticated and multi-physical which makes it challenging to model. The design of complicated sensors is often developed using an experimental-based approach where a prototype is created from intuition and then optimized through a large number of iterations with new a prototype and new experiments for each iteration [Kaltenbacher, 2015]. The experimental-based approach can be incredibly tedious, time-consuming, and costly, especially the in the case where an important design feature fails at a late stage in the design process. Relevant design parameters that are difficult to measure can also be challenging to include in the design process when using the experimental-based approach.

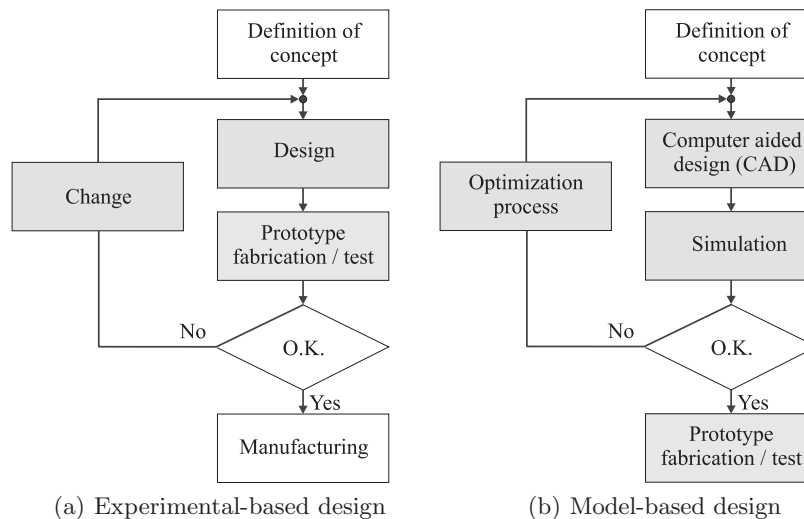


Figure 2.1. Design process using either the experimental-based approach or the model-based approach (figure edited from [Kaltenbacher, 2015])

More and more powerful computers have opened the possibility of designing complex sensors using a model-based approach through multi-physic simulations. Figure 2.1(a) shows a diagram of the experimental-based approach and Figure 2.1(b) shows a diagram the model-based approach.

The primary purpose of the model-based approach is to reduce the number of prototypes and the development time, thus also the final cost. Other, benefits like the visualization of the physics behind the sensor can further help the engineer to understand the sensor in depth. It is, however, important to comprehend the complexity of large models and the uncertainties that arise from numerical errors, wrong material parameters, and other uncertain physical parameters need in models.

The primary focus of this work lays in the development of a modeling framework, that can be used in the computer aided design and simulation blocks seen in Figure 2.1.

2.1.1 The Ultrasonic Turbidity Sensor Prototype

The prototype of the ultrasonic turbidity (UT) sensor in the scope of this work, can be seen in Figure 2.2. The UT sensor is based on the ultrasonic flow velocity meter Ultraflow 14 made by Kamstrup A/S. The passage in the middle section seen in Figure 2.2 is constructed for the purpose of turbidity measurements, and the measurement tube is as well altered. The first piezoelectric transducer seen from the inlet is a 10MHz resonance transducer that is used to generate the wave pack for the flow velocity and turbidity measurements, as described in Section 1.3. The center piezoelectric transducer is a highly sensitive transducer used to intercept the small scattering signals as seen in Figure 2.2. The last piezoelectric transducer is similar to the first transducer but mainly used for the measurement of flow velocity. The measurement tube (see Figure 2.2) is used to avoid flow vortexes in the middle section passage that may obstruct the turbidity measurements.

The UT sensor is, therefore, a highly mechatronic system that involves various physical fields. A piezoelectric transducer exposed by force produces a small charge that can be measured. This effect is called the direct piezoelectric effect. On the other hand, if a voltage is applied to the piezoelectric transducer, an inverse piezoelectric effect results in a mechanical deformation. The mechanism of the piezoelectric transducers is, therefore, an interaction between electric quantities like electric field intensity and electric induction, and mechanical quantities like stress and strain [Kaltenbacher, 2015]. A power electronic circuit has to drive the first and last piezoelectric transducer, and an electric measurement circuit has to measure the response from the middle piezoelectric transducer. The mechanical deformation of the piezoelectric transducer results in a force applied to the fluid, which propagates through the fluid as an acoustic pressure wave [Arnau Vives, 2008; Schmerr, 2016; Morse & Ingard, 1968]. The fluid flow as well interacts with the acoustic pressure wave through altered fluid properties like the speed of sound and the fluid density. The flow itself may also generate flow-induced sound that emerges in turbulent flows [Landau &

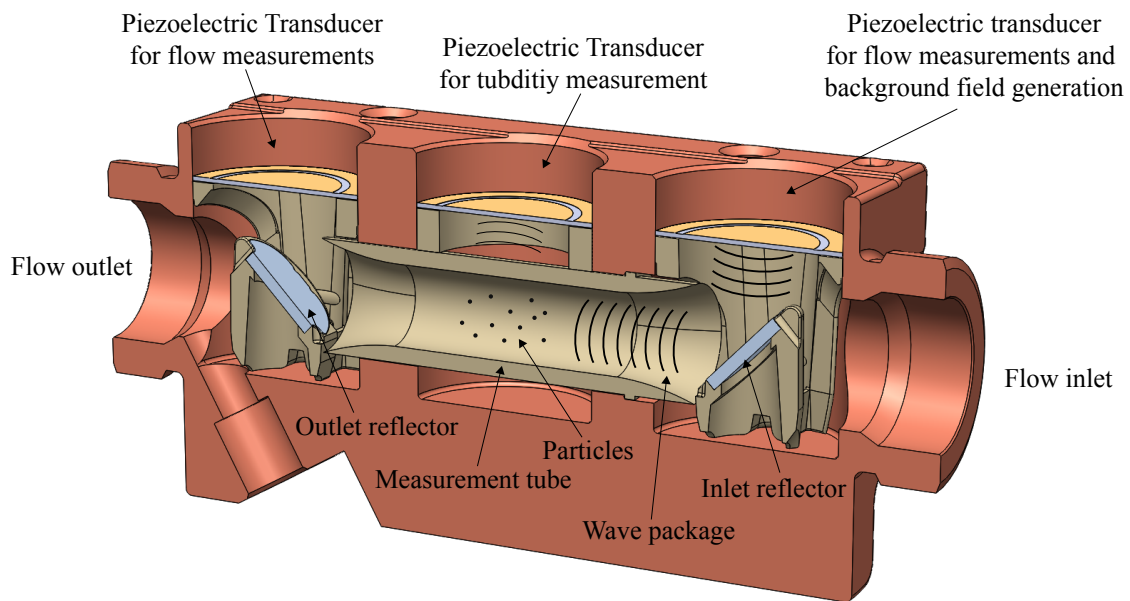


Figure 2.2. Geometry of the ultrasonic turbidity sensor with annotations

Lifschitz, 1987; Kaltenbacher, 2015]. And lastly, the particle trajectories through the sensor is highly dependent the fluid flow [COMSOL, 2017g]. When acoustic waves propagate through the sensor and strike the particles, the acoustic field itself exert a force on the particles in the fluid as described in Settnes & Bruus [2012]. This force is, however, assumed to be much smaller than the force from the fluid flow and, therefore, neglected in this work.

The physical interactions that can be found in the ultrasonic turbidity sensor can, therefore, be summarized as:

- Electrical \longleftrightarrow Mechanical interaction
An electrical voltage applied over the piezoelectric element leads to a mechanical deformation.
- Mechanical \longleftrightarrow Acoustical interaction
The force from the piezoelectric transducer has to equal the force imposed to the fluid.
- Fluid \longleftrightarrow Acoustical interaction
The fluid properties influence the acoustic wave propagation, and fluid vortexes generate sound waves to some extent.
- Fluid \longleftrightarrow Particle tracing interaction
Fluid forces affect the particle motion through the drag force.

The pressure on the piezoelectric turbidity transducer measures the acoustic field which is, thus the primary physical field affecting the output of the turbidity sensor. In the following section, a thorough description of the governing equations behind the acoustic motion is presented, together with the derivation of the solution for the scattering pressure for a single particle.

2.2 Governing Equations of Linear Acoustics

The theory behind acoustic motion is comprehensive but also a well-described topic. Classical literature such as Morse & Ingard [1968] and Pierce [1989], is widely cited in this section, but also newer literature like Schmerr [2016] and Kaltenbacher [2015] is used.

The analytical solution of the scattering field from a single particle struck by a plane wave is derived in this section together with a Far-Field approximation. From the solution of the scattering field and the Far-Field approximation, important properties of the scattering field are obtained. Also, the solution of the scattering field is used in later chapters as a reference for numerical simulations (see Chapter 6 on page 45).

In the governing equations of acoustics, the dependent variables are usually divided into an ambient variable and a disturbed variable. The variables for pressure, density, and acoustic velocity can, in this manner, be written as:

$$p_{\text{total}} = p_0 + p_d \quad \rho_{\text{total}} = \rho_0 + \rho_d \quad \mathbf{v}_{\text{total}} = \mathbf{v}_0 + \mathbf{v}_d \quad (2.1)$$

where $p_{\text{total}}, \rho_{\text{total}}, \mathbf{v}_{\text{total}}$ are the dependent variables, $p_0, \rho_0, \mathbf{v}_0$ are the ambient variables and $p_d, \rho_d, \mathbf{v}_d$ are the disturbed variables. It is assumed that $p_0 \gg p_d, \rho_0 \gg \rho_d$ and $c \gg \mathbf{v}_d$, with c being the speed of sound in the material [Kaltenbacher, 2015].

The ambient variables are defined by the medium of which sound propagates and in a homogeneous medium independent of the position, which is assumed in this work. It is further assumed that the ambient variables are independent of time, thus constant, and that the ambient acoustic velocity is zero ($\mathbf{v}_0 = \mathbf{0}$).

The acoustic field can be described by the continuity equation, the conservation of momentum and the pressure-density relation [Pierce, 1989]. Assuming a non-viscous media and no external forces, the continuity equation, the conservation of momentum (Euler equation) and the pressure-density relation, with the ambient and perturbed variables, can be written as [Pierce, 1989]:

$$\frac{\partial(\rho_0 + \rho_d)}{\partial t} + \nabla \cdot [(\rho_0 + \rho_d)\mathbf{v}_d] = 0 \quad (2.2)$$

$$(\rho_0 + \rho_d) \left(\frac{\partial}{\partial t} + \mathbf{v}_d \cdot \nabla \right) \mathbf{v}_d = -\nabla(p_0 + p_d) \quad (2.3)$$

$$p_0 + p_d = p_t(\rho_0 + \rho_d) \quad (2.4)$$

where ∇ is the gradient operator, t is the time, and $p(\rho_0 + \rho_d)$ is a thermodynamic relation of the pressure and density (see [Pierce, 1989, p. 15]).

A linear approximation of Equations 2.2 to 2.4, is called the acoustic approximation [Pierce, 1989]. In the linear approximation, higher-order terms are neglected which gives:

$$\frac{\partial \rho_d}{\partial t} + \rho_0 \nabla \cdot \mathbf{v}_d = 0 \quad (2.5)$$

$$\rho_0 \frac{\partial \mathbf{v}_d}{\partial t} + \nabla p_d = 0 \quad (2.6)$$

$$p_d = \rho_d c^2 \quad (2.7)$$

Equation 2.7 is only valid if $|p_d| \ll \rho_0 c^2$ [COMSOL, 2017b]. Taking the time derivative of the linear continuity equation (see Equation 2.5), yields:

$$\frac{\partial^2 \rho_d}{\partial t^2} + \frac{\partial}{\partial t}(\rho_0 \nabla \cdot \mathbf{v}_d) = 0 \implies \nabla \cdot \frac{\partial \mathbf{v}_d}{\partial t} = -\frac{1}{\rho_0} \frac{\partial^2 \rho_d}{\partial t^2} \quad (2.8)$$

Inserting the linear conservation of momentum in Equation 2.6 and the linear pressure-density relation in Equation 2.7 into Equation 2.8 yields the wave equation for the pressure disturbance p_d :

$$\nabla \cdot \frac{-\nabla p_d}{\rho_0} = -\frac{1}{\rho_0 c^2} \frac{\partial^2 p_d}{\partial t^2} \implies \nabla^2 p_d - \frac{1}{c^2} \frac{\partial^2 p_d}{\partial t^2} = 0 \quad (2.9)$$

where the Laplace operator ∇^2 is dependent upon the coordinate system of interest. As evident later, especially the spherical coordinate system is of interest in this work. The Laplace operator in spherical coordinates is given as [Morse & Ingard, 1968, p.308]:

$$\nabla^2 = \frac{1}{r^2} \frac{\partial}{\partial r} \left(r^2 \frac{\partial}{\partial r} \right) + \frac{1}{r^2 \sin(\theta)} \frac{\partial}{\partial \theta} \left(\sin(\theta) \frac{\partial}{\partial \theta} \right) + \frac{1}{r^2 \sin(\theta)^2} \frac{\partial^2}{\partial \phi^2} \quad (2.10)$$

Assuming that the wave contribution is only in the radial direction, thus independent of the spherical angles ϕ and θ , one can find the wave equation of simple source with waves moving spherically outward:

$$\frac{1}{r^2} \frac{\partial}{\partial r} \left(r^2 \frac{\partial p_d}{\partial r} \right) = \frac{1}{c^2} \frac{\partial^2 p_d}{\partial t^2} \quad (2.11)$$

The wave equation in Equation 2.11, has a general solution in the form:

$$p_d = \frac{1}{r} f(r - ct) + \frac{1}{r} g(r + ct) \quad (2.12)$$

where $f(r - ct)$ denote the wave in the positive direction and $g(r + ct)$ denote the wave in the negative direction. The general solution is close to the solution of plane waves [Pierce, 1989], but with a $\frac{1}{r}$ term showing that spherical waves decrease inverse proportional to r if the medium is infinite in extent.

2.2.1 Acoustic Scattering from a Sphere

The derivation of the scattering field presented in this subsection follows the approach found in Schmerr [2016], together with deviations from Morse & Ingard [1968].

Time-harmonic waves or monochromatic waves as called in Landau & Lifschitz [1987] are waves where the dependent quantities are periodic functions of time. It is often convenient to write these kinds of quantities as the real part of some complex quantity. The time-harmonic pressure can be written as:

$$p_d = \text{Re}\{p' e^{-i\omega t}\} \quad (2.13)$$

where ω is the angular wave frequency, the complex value $i = \sqrt{-1}$ and p' is a complex function independent of time. This can be $p' = \hat{p} e^{ikr}$ for radial waves, where $k = \omega/c$ is the wave number and \hat{p} is the peak amplitude.

Inserting the complex time-harmonic description of the pressure into the wave equation (see Equation 2.9) gives the following expression:

$$\nabla^2 \text{Re}\{p' e^{-i\omega t}\} - \frac{1}{c^2} \frac{\partial^2}{\partial t^2} \text{Re}\{p' e^{-i\omega t}\} = 0 \quad (2.14)$$

Since the sum of the real parts of several complex numbers is equal to the real part of the sum of the complex numbers [Pierce, 1989], Equation 2.14 can be written as:

$$\text{Re}\{\nabla^2 p' e^{-i\omega t} - \frac{1}{c^2} \frac{\partial^2}{\partial t^2} p' e^{-i\omega t}\} = 0 \quad (2.15)$$

$$\text{Re}\{(\nabla^2 p + \frac{\omega^2}{c^2} p)\} = 0 \quad (2.16)$$

where $p = p' e^{-i\omega t} = \hat{p} e^{ikr} e^{-i\omega t}$ which satisfies the equation

$$\nabla^2 p + \frac{\omega^2}{c^2} p = 0 \longrightarrow \nabla^2 p + k^2 p = 0 \quad (2.17)$$

Equation 2.17 is called the homogeneous Helmholtz equation and describes the harmonic pressure wave of $e^{-i\omega t}$ time dependency. It is expected that the particle shape differs from particle to particle. However, geometries that can be characterized by only one parameter, like spherical geometries, are often used as an approximation for simplicity [Pons & Dodds, 2015; Silva & Bruus, 2014], which is also the case in this study.

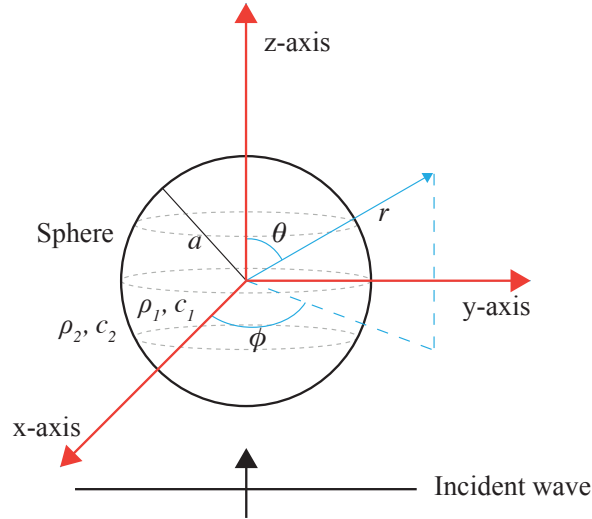


Figure 2.3. Incident plane wave in a fluid striking a solid sphere with radius a . The spherical coordinates (r, θ, ϕ) are also shown.

A particle sphere of radius a , immersed in a fluid with density and pressure both satisfying the homogeneous Helmholtz equation can be seen in Figure 2.3. The sphere density and

sphere speed of sound are denoted ρ_1 and c_1 respectfully, and the fluid density and fluid speed of sound are denoted ρ_2 and c_2 respectfully.

Rewriting the Helmholtz equation (see Equation 2.17) in spherical coordinates (r, θ, ϕ) using Equation 2.10 gives the following:

$$\frac{1}{r^2} \frac{\partial}{\partial r} \left(r^2 \frac{\partial p}{\partial r} \right) + \frac{1}{r^2 \sin(\theta)} \frac{\partial}{\partial \theta} \left(\sin(\theta) \frac{\partial p}{\partial \theta} \right) + \frac{1}{r^2 \sin^2(\theta)} \frac{\partial^2 p}{\partial \phi^2} + k_j^2 p = 0 \quad (2.18)$$

where $k_j = \frac{\omega_j}{c_j}$ ($j = 1, 2$). Equation 2.18 can be solved using separation of variables, where it is assumed that the pressure p can be factorized into a product of terms only dependent upon a single variable, that is $p = R(r)\Theta(\theta)\Phi(\phi)$ [Schmerr, 2016; Morse & Ingard, 1968]. Inserting the factorized product into the spherical Helmholtz equation (see Equation 2.18) gives:

$$\left\{ \frac{1}{R} \frac{d}{dr} \left(r^2 \frac{dR}{dr} \right) + \frac{1}{\Theta \sin(\theta)} \frac{d}{d\theta} \left(\sin(\theta) \frac{d\Theta}{d\theta} \right) + k_j^2 r^2 \right\} \sin^2(\theta) = -\frac{1}{\Phi} \frac{d^2 \Phi}{d\phi^2} \quad (2.19)$$

From Equation 2.19 it can be seen that the left-hand side is only a function of θ and r , thus a function $F(r, \theta)$ can be written and the right-hand side is only a function of ϕ , thus a function $G(\phi)$ can be written. Since the variables in Equation 2.19 are independent, they must be equal to a constant, thus $F(r, \theta) = G(\phi) = \gamma^2$ where γ^2 is chosen for convenience as evident later.

Taking basis on the right-hand side, the following expression can be written:

$$G(\phi) = \gamma^2 \longrightarrow \frac{d^2 \Phi}{d\phi^2} + \Phi \gamma^2 = 0 \quad (2.20)$$

that is of the same form as a harmonic oscillator with the solution:

$$\Phi = e^{im\phi} \quad (2.21)$$

where $\gamma = m$ is an integer because the pressure must be single valued in ϕ [Schmerr, 2016]. Using the same approach for the right-hand side ($F(r, \theta) = \gamma^2$), yields:

$$\frac{1}{R} \frac{d}{dr} \left(r^2 \frac{dR}{dr} \right) + k_j^2 r^2 = \frac{m^2}{\sin^2(\theta)} - \frac{1}{\Theta \sin(\theta)} \frac{d}{d\theta} \left(\sin(\theta) \frac{d\Theta}{d\theta} \right) \quad (2.22)$$

As before, since the variables in Equation 2.22 are independent the left-hand side can be written as $f(r) = l^2$ and the right-hand side can be written as $g(\theta) = l^2$. Assuming that $l^2 = n(n+1)$, where n is an integer, then $f(r)$ and $g(r)$ can be found in the following form:

$$f(r) = l^2 \longrightarrow \frac{d}{dr} \left(r^2 \frac{dR}{dr} \right) + (k_j^2 r^2 - n(n+1))R = 0 \quad (2.23)$$

$$g(\theta) = l^2 \longrightarrow \frac{1}{\sin(\theta)} \frac{d}{d\theta} \left(\sin(\theta) \frac{d\Theta}{d\theta} \right) + \left(n(n+1) - \frac{m^2}{\sin^2(\theta)} \right) \Theta = 0 \quad (2.24)$$

In the case of axial symmetry, the wave is independent of ϕ and therefore $m = 0$, which reduces Equation 2.24 to an equation that has the Legendre polynomials $P_n(\cos(\theta))$ as

the solution [Morse & Ingard, 1968]. Also, a solutions for $R(r)$ in Equation 2.23 can be found to be the spherical Hankel function of the first kind given as $h_n^{(1)}(kr)$ (with $e^{-i\omega t}$ time-dependency), where kr is the nominalized radius ($\frac{\omega}{c}r$). The spherical Hankel function can be described in terms of spherical Bessel functions using the following relation:

$$h_n^{(1)} = j_n + i n_n \quad (2.25)$$

where j_n is the spherical Bessel function of the first kind and n_n is the spherical Bessel function of the second kind. In Appendix A.2.1, some of the spherical Bessel and spherical Hankel functions be found.

The spherical Hankel function has the property of only describing outgoing waves and does, therefore, satisfy the Sommerfeld's radiation condition stating that the pressure should vanish at infinity, thus $p \rightarrow 0$ as $r \rightarrow \infty$ [Schmerr, 2016].

The scattering pressure can, therefore, be calculated by combining each of solutions for the factorized variables and summing up the infinite series, which gives:

$$p_{sc} = \sum_{n=0}^{\infty} C_n h_n^{(1)}(k_2 r) P_n(\cos(\theta)) \quad (2.26)$$

where C_n is the scatter wave coefficient that describes the influence of boundary conditions.

The scatter wave coefficient C_n can be found by relating the pressure and normal velocity at the surface of the sphere. The incident wave, as seen in Figure 2.3, travels along the z-axis and can be described in spherical coordinates as [Schmerr, 2016]:

$$p_{inc} = A e^{ik_2 z} = A \sum_{n=0}^{\infty} i^n (2n+1) j_n(k_2 r) P_n(\cos(\theta)) \quad (2.27)$$

where A is the plane wave pressure amplitude.

The flaw pressure wave inside the sphere can be found in the same manner as the scattering pressure and are given as [Schmerr, 2016]:

$$p_{flaw} = \sum_{n=0}^{\infty} D_n j_n(k_1 r) P_n(\cos(\theta)) \quad (2.28)$$

Thus, the pressures and normal velocities at the surface ($r = a$) can be related as:

$$p_{inc} + p_{sc} = p_{flaw} \quad (2.29)$$

$$\frac{1}{\rho_2} \frac{\partial p_{inc}}{\partial r} + \frac{1}{\rho_2} \frac{\partial p_{sc}}{\partial r} = \frac{1}{\rho_1} \frac{\partial p_{flaw}}{\partial r} \quad (2.30)$$

where the normal velocity is calculated as $\frac{1}{i\omega\rho} \frac{\partial p}{\partial r}$ which can be found using the conservation of momentum in Equation 2.6 and the monochromatic description of the acoustic velocity.

Using Equation 2.29 and Equation 2.30 the coefficients for the scatter wave (C_n) and flaw wave (D_n) can be solved (the derivation of the coefficients can be found in Appendix A.1). The solution for the scatter wave coefficient (C_n) is found as:

$$C_n = \frac{i^n(2n+1)}{\Omega} \left\{ \frac{j_n(k_2a)[j_n(k_1a)]'}{\rho_1c_1} - \frac{j_n(k_1a)[j_n(k_2a)]'}{\rho_2c_2} \right\} \quad (2.31)$$

$$\Omega = \frac{j_n(k_1a)[h_n^{(1)}(k_2a)]'}{\rho_2c_2} - \frac{h_n(k_2a)[j_n(k_1a)]'}{\rho_1c_1} \quad (2.32)$$

where the prime denote the derivative (see Appendix A.2.1), that can be found as:

$$[j_n(\zeta)]' = \frac{1}{2n+1} [nj_{n-1}(\zeta) - (n+1)j_{n+1}(\zeta)] \quad (2.33)$$

for both the spherical Bessel function and the spherical Hankel function.

The solution to the scattering problem for the rigid case $\rho_1c_1 \rightarrow \infty$, can be seen in Figure 2.4. The solution is found using a unit incident wave with a frequency of 10MHz, a radius of $a = 5\mu\text{m}$ and speed of sound of $c_2 = 1500\text{m/s}$.

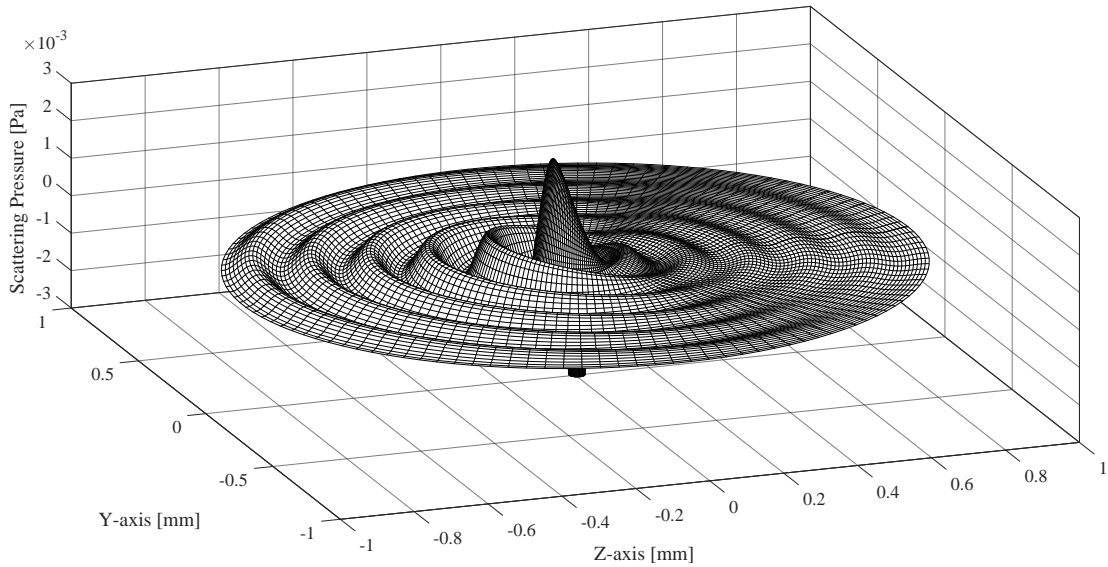


Figure 2.4. Scatter wave as a result of a unit amplitude 10MHz plane wave traveling in water ($c_2 = 1500\text{m/s}$) along the z-axis striking a sphere with radius $a = 5\mu\text{m}$. The solution is evaluated by truncating the solution to ten terms.

Figure 2.5 shows the scattering field solution for a 10MHz unit amplitude plane wave striking a non-rigid sphere with the material properties $c_1 = 2400\text{m/s}$, $\rho_1 = 1050\text{kg/m}^3$ and with a radius of $a = 5\mu\text{m}$. The fluid medium has the properties $c_2 = 1500\text{m/s}$, $\rho_2 = 1000\text{kg/m}^3$.

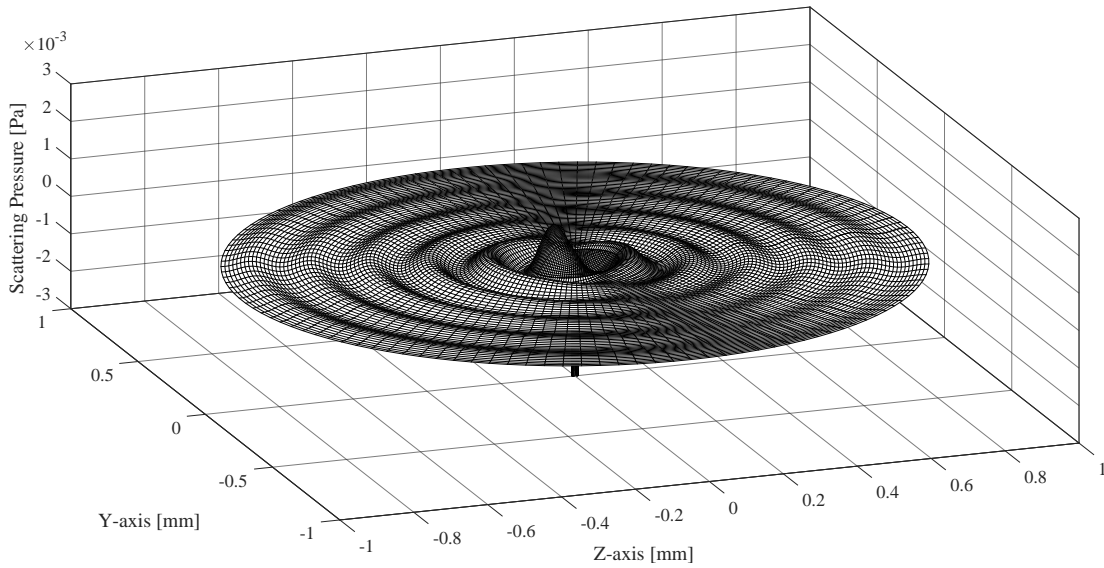


Figure 2.5. Non-Rigid Scatter wave as a result of a unit amplitude 10MHz plane wave traveling in water ($c_2 = 1500 \text{ m/s}$, $\rho_2 = 1000 \text{ kg/m}^3$) along the z-axis striking a sphere with the properties $c_1 = 2400 \text{ m/s}$, $\rho_1 = 1050 \text{ kg/m}^3$ and with a radius of $a = 5\mu\text{m}$.

Figure 2.6 shows the percentage of the scattering pressure related to the incident wave amplitude as a function of particle diameters calculated as $r/2a$. The scattering pressure in Figure 2.6 is calculated in the same manner as for Figure 2.4 with a rigid sphere, an incident wave frequency of 10MHz and a particle diameter of $a = 5\mu\text{m}$.

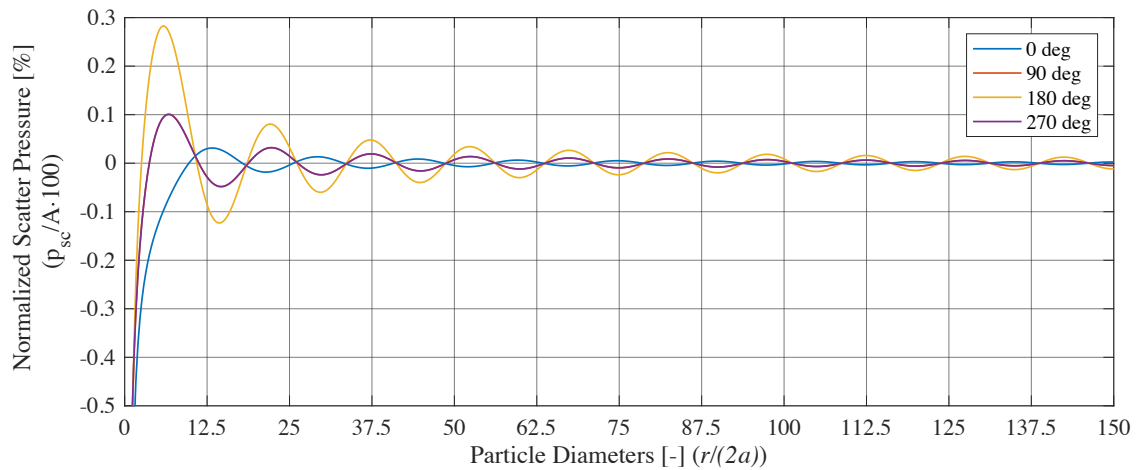


Figure 2.6. Normalized pressure (p_{sc}/A) as a function of particle diameters ($r/2a$), for different angles $\theta = [0\text{deg } 90\text{deg } 180\text{deg } 270\text{deg}]$. The particle is assumed rigid with a radius of $a = 5\mu\text{m}$ and the incident wave frequency is 10MHz.

The exact solution to the scattering field found in Equation 2.26 require numerical evaluation, and it is difficult to extract the relations between parameters like pressure amplitude and particle size or the influence of different material parameters. Using far-field approximations a more simple expression can be found for the scattering field.

2.2.2 Far-Field Approximation

The theory of asymptotics can be used to approximate complex functions, like the Bessel or Hankel functions, into more simple functions. Approximated functions are often seen in the analysis of scattering fields, and especially in classical literature such as Pierce [1989] or Morse & Ingard [1968] where the asymptotic approximations are used to describe the scattering field in closed form and numerical evaluations are, therefore, avoided. This subsection contains the derivation of the far-field approximation of the scattering field solution in Equation 2.26.

The Hankel function $h_n^{(1)}$, seen in Equation 2.26 has the following asymptotic behavior for the far-field ($kr \rightarrow \infty$) [Morse & Ingard, 1968, p.336]:

$$h_n^{(1)}(kr) \sim \frac{(-i)^{n+1}}{kr} e^{ikr} \quad \text{as } kr \rightarrow \infty \quad (2.34)$$

Inserting the asymptotic Hankel function into the expression for the scattering field (see Equation 2.26), yields:

$$p_{sc} = \frac{e^{ik_2 r}}{k_2 r} \sum_{n=0}^{\infty} (-i)^{(n+1)} C_n P_n(\cos(\theta)) \quad (2.35)$$

From Equation 2.35 it can be seen that the scattering wave decreases as a function of the radius r just as the solution to the pressure of a simple source in Equation 2.12.

A first order approximation of Equation 2.35 can be found using the first and second term of the Legendre functions (see Appendix A.2.2) which yields:

$$p_{sc} = \frac{1}{r} e^{ik_2 r} \left(\frac{-iC_0 - C_1 \cos(\theta)}{k_2} \right) \quad (2.36)$$

Since the sphere of interest is particles with sizes in the lower micron range and since the frequency of the transducer is in the lower MHz range, it is assumed that the short-wavelength limit $ka \ll 1$ is fulfilled. In this limit, the spherical Bessel and spherical Hankel functions found in the scatter wave coefficient C_n can be approximated by asymptotic descriptions. A list of relevant asymptotic descriptions of the spherical Bessel and spherical Hankel functions can be found in Appendix A.3. Inserting the asymptotic descriptions into Equation 2.31 and using a great deal of algebra together with the relation $k = \omega/c$, gives for the first and second term the following scatter wave coefficients, can be found:

$$C_0 \sim -i \frac{k_2^3 a^3}{3} \left(1 - \frac{\lambda_{b,2}}{\lambda_{b,1}} \right) \left\{ \frac{1}{1 - \frac{1}{3} \frac{\lambda_{b,2}}{\lambda_{b,1}} (k_2 a)^2} \right\} \quad \text{as } k_j a \rightarrow 0 \quad (2.37)$$

$$\approx -i \frac{k_2^3 a^3}{3} \left(1 - \frac{\lambda_{b,2}}{\lambda_{b,1}} \right) \quad \text{for } k_j a \ll 1 \quad \text{as } k_j a \rightarrow 0$$

$$C_1 \sim k_2^3 a^3 \left(\frac{\rho_2 - \rho_1}{2\rho_1 + \rho_2} \right) \quad \text{as } k_j a \rightarrow 0 \quad (2.38)$$

where $\lambda_{b,j} = c_j^2 \rho_j$ ($j = 1, 2$) is the bulk modulus¹ of the fluids.

Inserting the scatter wave coefficients into Equation 2.36 gives the far-field approximation of the scattering field:

$$p_{sc} = \frac{1}{r} e^{ik_2 r} \left(-\frac{1}{3} k_2^2 a^3 \left\{ \frac{\lambda_1 - \lambda_2}{\lambda_1} - \frac{3(\rho_1 - \rho_2)}{2\rho_1 + \rho_2} \cos(\theta) \right\} \right) \quad (2.39)$$

From Equation 2.39, it can be seen that the pressure scales with the wave number squared k_2^2 , thus scales with the angular frequency squared since $k_2^2 = \frac{\omega^2}{c_2^2}$. It can also be seen that the particle size scales with a^3 and an increase of particle size from $1\mu m$ to $10\mu m$, thus results in an amplitude gain of 1000. It can also be seen in Equation 2.39 that the compressibility difference between the materials scales the amplitude of the wave, while the density difference scales the amplitude of the wave as a function of the scattering angle θ .

¹Also referred as adiabatic bulk modulus

PROBLEM STATEMENT

Water quality measure is crucial in distribution networks, making sure that only high-quality water reaches the end-user. An ultrasonic Doppler multi-scattering method for measuring turbidity has by Kamstrup A/S, been found interesting due to the potentially low-cost solution compared to optical turbidimeters and due to the possibilities of incorporating the ultrasonic turbidity sensor into existing technologies by Kamstrup A/S. In order to exploit the full potential of the ultrasonic turbidity sensor, a thorough model of the sensor should be conducted allowing the sensor design to be model-based. Important relations between particle concentration, flow velocity, and the expected output is as well critical for the understanding of the sensor, which leads to the following problem statement:

How can an ultrasonic turbidity sensor be modeled such that the design can be model-based and how do critical parameters like the particle concentration and flow velocity, scale the expected output of the sensor?

The aim of this Master's Thesis is to create a design tool that can be used to optimize the design of the ultrasonic turbidity sensor. The design tool is conducted using a multi-physical approach combining different numerically based studies.

The design tool consists of Computational Fluid Dynamics (CFD) simulations, particle tracing simulations, and simulations of acoustic scattering fields, taking base in the geometry presented in Figure 2.2. As shown in the analysis, the acoustic scatter field of a single particle in an infinite medium can be modeled by means of analytical expressions. Relating the analytically calculated scattering field with the numerically calculated gives insight to the precision of the numerical model using different mesh sizes and other crucial parameters. A numerical multi-scattering simulation is conducted using the parameters found from the numerical analysis of a single particle. The particle positions for the multi-scattering simulations is calculated utilizing first a stationary CFD simulation of the flow field and then a transient particle tracing simulation with drag force as the coupling parameter between the flow field and the particle movement.

3.1 Conditions for the Simulations

To make the problem more tangible, a summary of the contamination levels, particle properties, flow conditions, and fluid properties expected for the sensor, is formed in cooperation with Kamstrup A/S:

Inlet flow velocity has been chosen in the range $0.5 \frac{m}{s}$ to $10 \frac{m}{s}$ since that is the expected flow velocities for the Ultraflow 14 [Kamstrup, 2004]

The fluid properties are water with a temperature of 10°C , a dynamic viscosity of $1.307 \cdot 10^{-3} \frac{kg}{m \cdot s}$, and a density of $999.7 \frac{kg}{m^3}$ [Çengel et al., 2012].

The transducer frequency is 10MHz in order to obtain a scattering pressure large enough to be measured [Kamstrup, 2017a].

The particle concentrations of interest in this study are between $100 \frac{p}{mL}$ and $6000 \frac{p}{mL}$ (particles per mL) [Kamstrup, 2017b]

The particle geometry is spheres with a diameter between 1μ and 20μ [Kamstrup, 2017b]

The particle material either silica balls with a density of $2500 \frac{kg}{m^3}$ and speed of sound $5960 \frac{m}{s}$ or polystyrene balls with a $1050 \frac{kg}{m^3}$ and speed of sound $2400 \frac{m}{s}$ [Kamstrup, 2017b]

THE MODEL STRUCTURE

This chapter gives an overview of the modeling framework for the simulation of the turbidity sensor (see Figure 2.2). The modeling framework is divided into two stages as shown in the diagram in Figure 4.1. The first stage consists of a CFD simulation and particle tracing simulation, which is described in Section 5. The second stage is described in Section 6, consisting of an auto-generation algorithm for the acoustic geometry and an acoustic frequency domain simulation to calculate the time-average RMS pressure field within a selected region of the sensor.

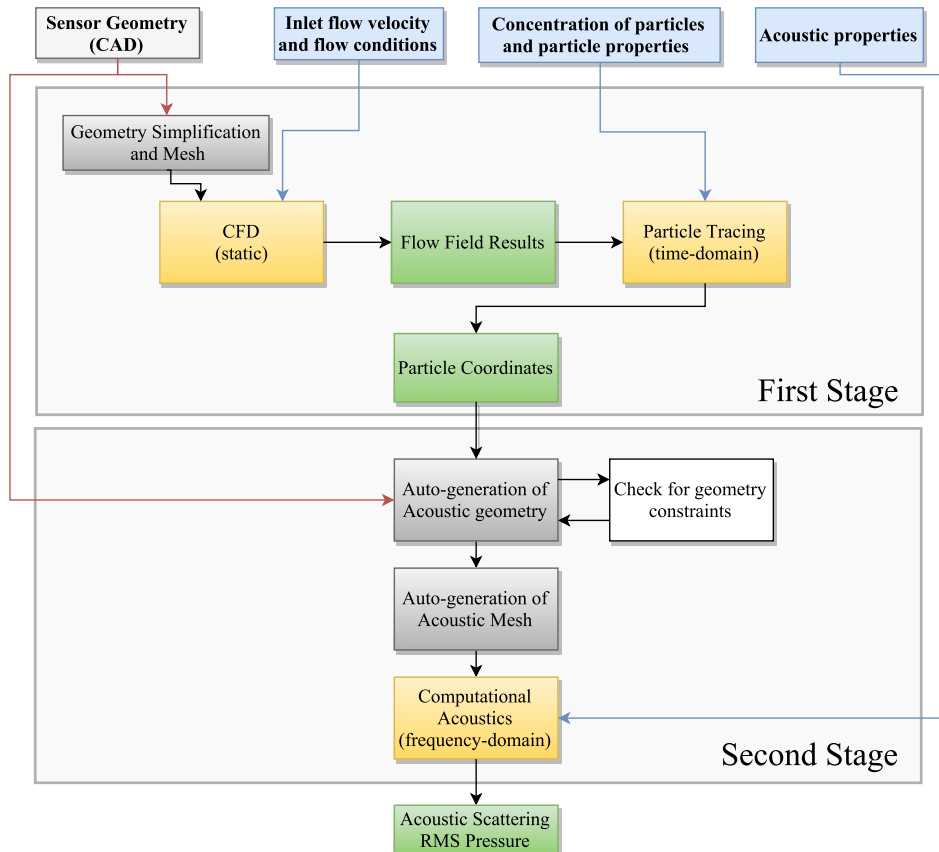


Figure 4.1. Diagram of the modeling framework used in this work. The modeling framework is divided into two stages, first a CFD and particle tracing stage and then a computational acoustic stage. Input parameters to the modeling framework is a sensor CAD, fluid properties, particle properties, and acoustic properties. The output of the modeling framework is the time-average RMS pressure field within a selected region of the sensor.

The input parameters needed for the modeling framework are sensor CAD geometry, inlet flow velocities, particle concentrations (p/mL), particle properties and acoustic properties such as acoustic frequency and pressure amplitude. Most of the properties can be found under the section Conditions for the Simulations (Section 3.1). A geometry simplification of the CAD geometry is needed in order to reduce the computational load of the CFD calculations. The simplified geometry is then meshed using appropriate meshing technics. The purpose of the CFD calculation is to calculate a static fluid flow field, that can be utilized in the particle tracing simulation. As evident later in Section 5, a turbulent fluid flow can be found for the geometry presented in Figure 2.2 and a turbulent model is, therefore, needed in the CFD simulation. Using a Newtonian description of the particle motion, the particle trajectories can be simulated within the simplified geometry. Adding the flow field to the particle simulation allow the motion of the particles to be affected by the flow field as a result of drag forces. A converged particle concentration is in Section 5.3 defined as the time instance where the particle concentration rate within some geometry feature of interest, does not change. Exporting the particle coordinates after particle concentration convergence then allows an acoustic geometry to be generated. The acoustic geometry consists of a symmetric cylinder embracing the exported particles which then allow acoustic high-frequency multi-scattering problems to be solved. The time-average RMS pressure field can then be extracted from the solution and related directly to the expected signal measured by the turbidity piezoelectric transducer (see Figure 2.2).

In the following section, the description of the first stage is presented.

FLUID FLOW AND PARTICLE TRACING IN THE SENSOR

In Section 2.2.2, it was found that the far-field acoustic pressure depends inverse proportional to the radius of radiation (see Equation 2.39). This makes the distance between the particles and the particle distribution an essential factor when determining the resulting multi-scattering pressure from the particle swarm inside the UT sensor. This chapter contains the theory behind the particle tracing simulation, and an overview of the theory behind the CFD calculations used to calculate the flow field within the UT sensor.

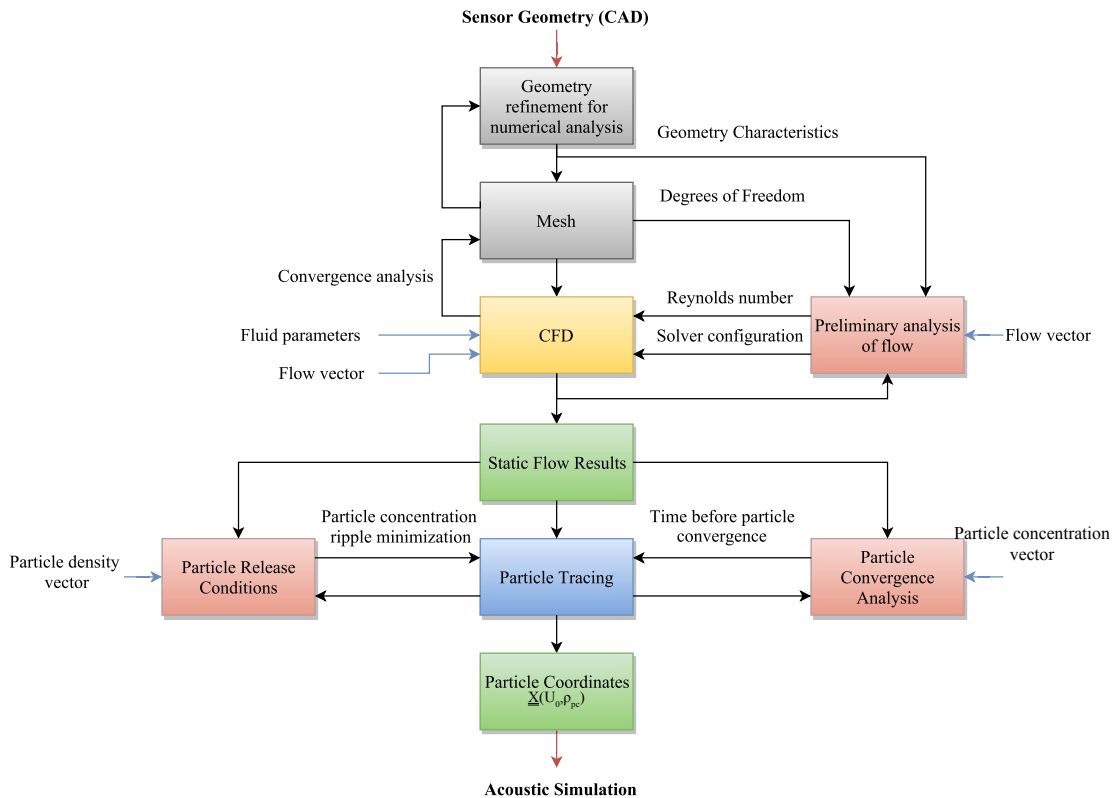


Figure 5.1. Modeling scheme for the first stage of the turbidity modeling framework.

The diagram in Figure 5.1 shows the modeling scheme for the first stage. The flow field for a simplified geometry is modeled using a turbulent CFD model, which is then used

to calculate the drag forces acting on the particles using a Newtonian description of the particle movement inside the geometry. The particle coordinates at a given time instance are then extracted from the particle trajectories, which is used to generate the acoustic geometry (see Section 6). This approach provides a more realistic distribution of particles, thus gives a better understanding of the acoustic field that can be expected when particles are present in a given section of the sensor geometry.

5.1 Geometry Refinement

Solving fluid flow problems are in general a very computational demanding problem especially in three dimensions. It is, therefore, crucial to determine whether it is necessary to include geometric characteristics like cosmetic features and manufacturing details that can be extraneous in numerical models. The geometry seen in Section 2.1.1 is therefore simplified as much as judged necessary to a limit where it is not expected that the fluid flow solution changes significantly. The main body of the sensor is not modified because the features of the main body (see Figure 5.2) affecting the flow domain are already simple. The inlet and outlet reflector modules and the measurement tube are, however, quite complex and are therefore streamlined and redrawn in SolidWorks. The simplifications reduce the total domain size and the number of sharp corners which lower the mesh requirements. The simplified geometry can be seen in Figure 5.2 and a comparison between the original CAD model and the simplified model can be seen in Appendix B.

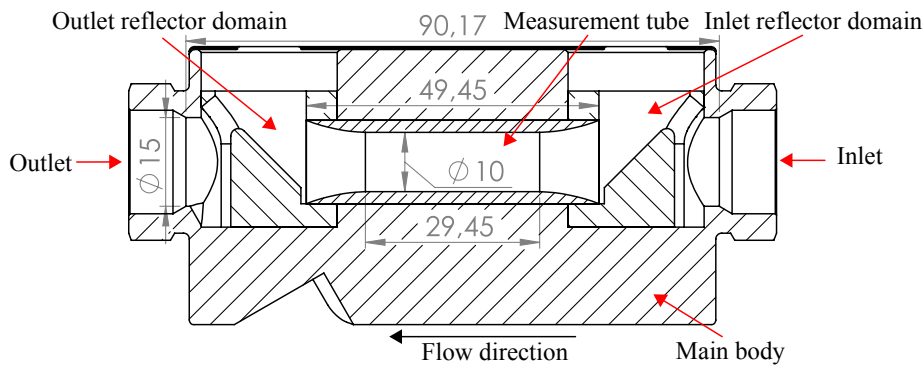


Figure 5.2. Side view of the simplified geometry used for CFD simulations and particle tracing simulations. All relevant geometry annotations used later can be seen in the figure, including geometry dimensions and domain tags.

Further simplifications are conducted in COMSOL after the SolidWorks CAD have been imported. Geometric symmetry can be found on two planes; the plane along the flow direction and the center plane orthogonal to the flow direction. It can, however, be found that the flow is only symmetric in one plane, namely the plane along the flow. Also, virtual operators like "Form Composite Domains" and "Form Composite Faces" are used in COMSOL to reduce the mesh by removing non-important help lines.

5.2 Flow Model

Fluid flow is, in general, characterized by dimensionless numbers like the Reynolds number or Mach number. The dimensionless numbers can be used to determine, preliminarily, what flow regime that can be expected for a given geometry. The Mach number is the ratio between the fluid velocity and the fluid speed of sound. Effects like shock waves and rarefaction may occur as the Mach number approaches one [COMSOL, 2017f]. The traditional CFD interface in COMSOL does only apply for Mach number below 0.3, which is well above the Mach number expected in this study ($\hat{M} = 10/1500 \sim 6 \cdot 10^{-3}$). The Reynolds number is the ratio between the inertia forces and the viscous forces. At large Reynolds numbers, the inertial forces dominate the viscous forces and the viscous forces cannot prevent random fluctuations in the fluid flow to occur, better known as turbulent flow. On the other hand, if the Reynolds number is small and the viscous forces dominate, then are random fluctuations suppressed, and the flow seems more ordered, called laminar flow.

For internal flow, the Reynolds number can be found as [Çengel et al., 2012]:

$$\text{Re} = \frac{\text{inertial forces}}{\text{viscous forces}} = \frac{U_0 D_{\text{hyd}}}{\nu} = \frac{\rho U_0 D_{\text{hyd}}}{\mu} \quad (5.1)$$

where ν is the kinematic viscosity, μ the dynamic viscosity, ρ the density and U_0 the average flow velocity and D_{hyd} the hydraulic diameter.

Using the measurement tube of the sensor as a reference (see Figure 5.2) and using the lowest expected average flow in the measurement tube, the smallest expected Reynolds number can be calculated. Assuming that the fluid is incompressible, the average flow velocity in the measurement tube U_{tube} can be related to the inlet flow velocity U_0 , using conservation of mass, thus:

$$\dot{m} = \rho \cdot U_0 \cdot A_{\text{in}} = \rho \cdot U_{\text{tube}} \cdot A_{\text{tube}} \quad (5.2)$$

$$\Rightarrow U_{\text{tube}} = \frac{A_{\text{in}}}{A_{\text{tube}}} \cdot U_0 \quad (5.3)$$

where A_{in} and U_0 are the inlet cross section area and inlet average flow velocity respectively, and A_{tube} and U_{tube} are the tube cross section area and tube flow velocity respectively. Using Equation 5.1 and Equation 5.3, together with the density and viscosity of water at 10°C [Çengel et al., 2012], the flow in the measurement tube of the sensor can be found to have a Reynolds number of approximately $\text{Re} \approx 8605$ at 0.5 m/s and $\text{Re} \approx 1.72 \cdot 10^5$ at 10 m/s. Flows in tubes with a Reynolds number over 4000-8000 is usually defined as fully turbulent and the flow in the proceeding is therefore treated as fully turbulent flow [Çengel et al., 2012].

5.2.1 The RANS model

The governing equations for fluid flow are the Navier-Stokes equations [Casey & Wintergerste, 2000]. Solving the Navier-Stokes equations directly would, however, be computationally tedious in the case of turbulent flow, because the random fluctuations in the turbulent flow would require an extremely high number of elements to be captured numerically. Common software packages for CFD like Ansys Fluent and COMSOL CFD does, therefore, use the Reynolds-averaged Navier-Stokes (RANS) models which are less computationally demanding. The Reynolds-average representation divides the flow quantities into a time-averaged mean flow with fluctuations [Casey & Wintergerste, 2000] [COMSOL, 2017c] (see Figure 5.3). The decomposition adds new variables to be solved, and additional information is therefore needed [Casey & Wintergerste, 2000]. Additional mathematical models have therefore been developed, known as turbulence models to close the RANS equations.

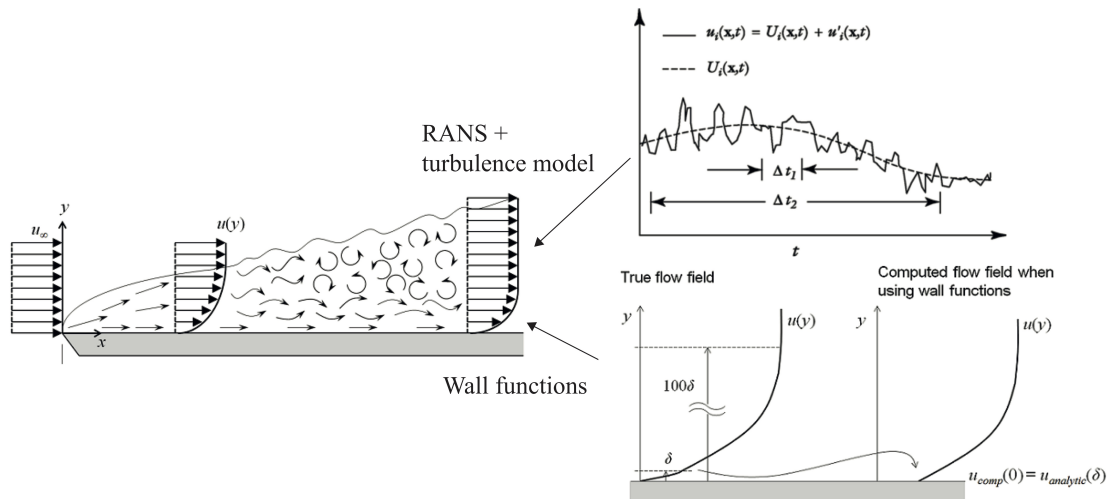


Figure 5.3. The fully turbulent region is calculated using the RANS model together with the turbulence models. The flow near walls are often calculated using an analytical wall function (Original figures from [Frei, 2013b] and [COMSOL, 2017c])

Turbulent flow is often the case in most industrial applications, and much work has been conducted in the last century to establish good turbulence models [Casey & Wintergerste, 2000]. Despite the extensive work on the subject carried out in literature, there is still no universal model that can describe all kinds of turbulent parameters [Homicz, 2004] [Menter, 1993] [Casey & Wintergerste, 2000] and determine the right turbulence model is often a highly non-trivial task that requires experimental validations to be truly trusted [Casey & Wintergerste, 2000].

5.2.2 Turbulence Models

There can be found several turbulence models in the literature, and they are often a trade-off between computational effort, robustness, and precision. The models are based on

heuristic arguments and empirical functions to supply the additional variables needed in the RANS model [Homicz, 2004]. The principal classes of turbulence models are Algebraic models, and Transport equation models. The Algebraic turbulence models describe the turbulent fluid motion using algebraic equations with only local properties of the fluid flow [Casey & Wintergerste, 2000]. The Algebraic models are computationally economic and robust, but they are also less accurate compared to Transport equation models [COMSOL, 2017f]. The main reason for the superior accuracy of the Transport equation models compared with Algebraic models is that they, in contrary to Algebraic models, does not depend purely on local flow conditions, but also the history of the flow [Casey & Wintergerste, 2000]. The turbulence models in the scope of this work are the Transport equation models k - ε , k - ω , and SST turbulence models, which are common turbulent models used in literature [Casey & Wintergerste, 2000].

The k - ε model is one of the most popular turbulence models for industrial applications due to its well-balanced compromise between accuracy, robustness and computational cost [COMSOL, 2017f]. It solves for the turbulent kinetic energy k and the rate of dissipation of kinetic energy ε , and performs well in free stream flows and for external flows but is generally not accurately for internal flows with flow fields that have adverse pressure gradient or large curvatures [Frei, 2013b]. The k - ε model in COMSOL's CFD Module utilizes wall functions to calculate the flow near the walls. Wall functions are analytical approximations of the flow near the walls and are, therefore, less computationally demanding. The principle of wall functions can be seen in Figure 5.3.

The k - ω model solves for the turbulent kinetic energy k and the specific rate of dissipation of kinetic energy ω . This model can be used in the case where the k - ε model cannot be used and are in general more accurate than the k - ε model. The k - ω model is often used when computing internal flows, flow near walls, flow with large curvatures and separated flows [Frei, 2013b] [Casey & Wintergerste, 2000]. The k - ω model is, however, not as robust as the k - ε , and is especially sensitive to initial guesses. Convergence problems are, therefore, common when using the k - ω model [Frei, 2013b]. The k - ω turbulence model in COMSOL uses wall functions in the same manner as the k - ε turbulence model.

The (shear stress transport) SST model is a combination of the two aforementioned turbulence models, exploiting the robustness and free stream features of the k - ε and the near wall features of the k - ω model [Menter, 1993]. The SST model implementation in COMSOL does not require wall functions and are therefore more precise around walls but does, as a consequence, also require a finer mesh near walls. Besides a larger mesh requirement for the SST model, the SST model also tends to converge slowly [Frei, 2013b] [COMSOL, 2017f].

Due to the superior accuracy when dealing with internal separated flows and strong streamline curvatures, the k - ω model is selected over the k - ε model. A preliminary study

using the SST model showed that the SST turbulence model tends to converge too slow to be practically usable for this study.

5.2.3 Meshing for Fluid Flow

Turbulent flow problems are often highly non-linear and computationally demanding and, therefore, very mesh sensitive. The mesh of fluid flow problems depend highly on the geometry and type of fluid flow, and it is always important to keep in mind that the accuracy of any numerical model is never better than the finite elements the geometry is divided into. As the element sizes get smaller, the problem tends to the actual solution even through the exact solution may not be reached due to non-linearities or convergence problems [Frei, 2013a]. Meshing 3D CAD geometries as the one in Figure 5.2 can be a tenuous task and a mesh analysis should be conducted to examine the accuracy of the model and minimize convergence problems. Unstructured meshes like the free tetrahedral (3D), and free triangular (2D) can be used discretize all kind of geometries, and the mesh-generating algorithms are highly automated [COMSOL, 2017c]. A mesh with fewer elements and equal quality can, however, be reached using structured mesh and should be utilized if applicable. The mesh types utilized in the fluid flow model of this work are; free tetrahedral, free triangular, swept mesh and boundary layer meshes.

Free tetrahedral and triangular mesh is an unstructured type mesh used in areas of the geometry where structured meshes do not apply. The mesh algorithms are highly automated but often results in a large number of elements.

Swept mesh is a particular kind of structured meshes that is structured in the direction of the sweep but unstructured in the direction of the source face.

Boundary mesh is also a structured mesh with an element distribution more dense in the direction normal to the surface of the boundary. The boundary mesh surface does not have to be structured.

The mesh used for the fluid flow can be seen in Figure 5.4.

The inlet and outlet reflector domains (see Figure 5.2) are meshed using the free tetrahedral mesh, that automatically generates free triangular meshes on all surfaces. The mesh in the measurement tube is a swept mesh with a free triangular source face. The mesh sizes for the entire geometry is based on COMSOL's automatic physics-based mesh sizes, with a normal size setting for the outlet reflector domain and a finer size setting for the inlet reflector domain and measurement tube domain. The boundaries are meshed using a boundary layer mesh with eight layers [COMSOL, 2017e] and automatic adjusted first layer thickness (thickness adjustment factor of one). Also, the corner refinement tool in COMSOL is used to reduce the elements size at sharp corner using the standard settings for the corner refinement tool [COMSOL, 2017d].

A comprehensive mesh convergence analysis has been conducted using mesh scaling

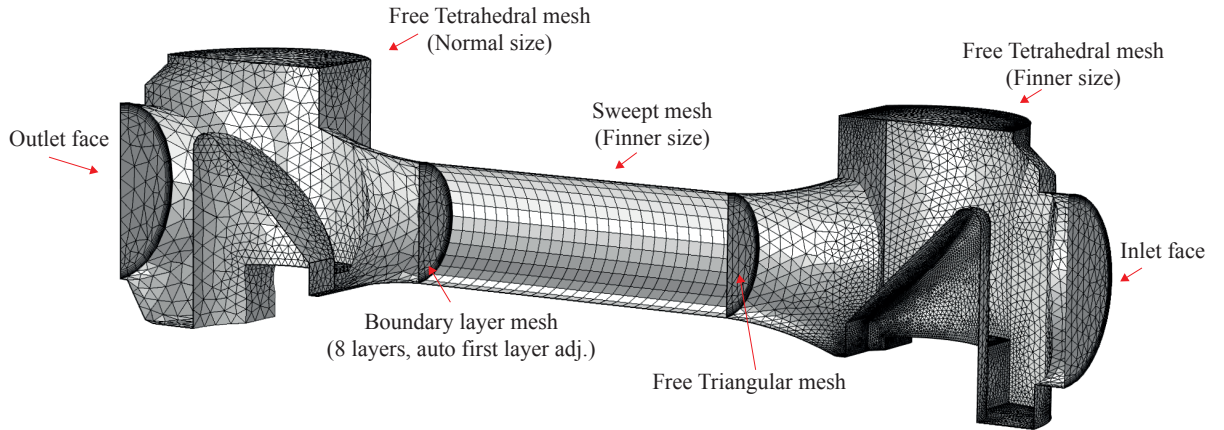


Figure 5.4. Mesh with annotations. The mesh types used are; free tetrahedral mesh, free triangular mesh, swept mesh, boundary layer mesh and corner refinement.

technics often seen in numerical studies. Even and uneven scaling (scaling in specific areas) of the mesh does result in convergence problems, which may be a result of unsteady flow. The convergence problems are discussed later in the discussion (see Chapter 9), but it is assumed that the solutions found using the mesh seen in Figure 5.4 is sufficient for the purpose of this work.

5.2.4 Boundary Conditions

The boundary conditions used for the fluid flow model can be seen in Figure 5.5. The outlet boundary conditions is a zero pressure boundary condition often used in internal flow simulations [COMSOL, 2017e]. Symmetry boundary condition is applied to the symmetry surface (transparent on Figure 5.5) and wall functions are employed to surfaces with no other prescribed boundary conditions.

Simple inlet boundary conditions like the circular (half) inlet as seen in Figure 5.5, can for laminar flows be described using parabolic expressions for fully developed laminar flow profiles. Analytical expressions for fully developed turbulent flow profiles are not as simple as for the laminar case, and often in the form of complicated semi-empirical functions [Çengel et al., 2012].

Instead of using analytical boundary conditions for the inlet, the boundary condition can be described by the solution of an secondary model mapped onto the original model. The secondary model is an easy to solve axis symmetric long tube with the same diameter as the inlet seen in Figure 5.5. The length of the tube has to be longer than the hydrodynamic entry length that describes the distance from the entrance of a pipe to the flow reaches its fully developed profile. The ratio between the hydrodynamic entry length L_h and the inlet pipe diameter D_{in} can, for turbulent flow, be approximated as [Çengel et al., 2012]:

$$\frac{L_h}{D_{in}} = 1.359\text{Re}^{1/4} \quad (5.4)$$

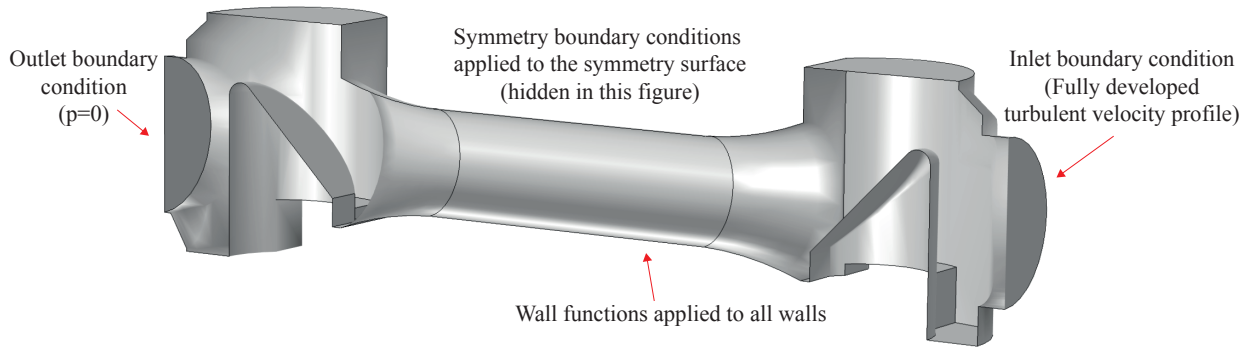


Figure 5.5. Boundary conditions used in the fluid flow model

Taking basis in the highest expected flow ($U_{in} = 10$ m/s) and using Equation 5.1 together with a inlet diameter of $D_{in} = 15$ mm, gives an inlet Reynolds number of $1.15 \cdot 10^6$. Using Equation 5.4, gives a non-dimensional hydrodynamic entry length of approximately 25. In the application note [COMSOL, 2017e], it is suggested to study the turbulent dynamic viscosity to observe when the turbulent profile is fully developed. The turbulent dynamic viscosity is one of the main parameters calculated in the turbulent fluid model, relating the turbulent kinetic energy k and the specific dissipation rate ω to the Reynolds stress tensor that is a key parameter in the RANS model [COMSOL, 2017c].

Figure 5.6 shows the simulated turbulent dynamic viscosity for a long tube with an inlet velocity of 10 m/s and a inlet diameter of 15 mm (see Appendix C for a further description of the inlet model and mesh). In Figure 5.6, it can be seen that the major changes in the turbulent dynamic viscosity are small after $z/D = 25$ as calculated in Equation 5.4. It can also be seen that there still are minor changes in the turbulent dynamic viscosity until approximately $z/D = 60-80$. To be certain that the turbulent flow is truly fully developed the length of inlet axis symmetric pipe are set to 80 times the inlet diameter. The fully developed turbulent outlet result from the 2D axis symmetric model is then mapped onto the 3D inlet face (see Figure 5.4) using the "General Extrusion" feature in COMSOL that can be used to couple the variables of different models and coordinate systems. Also, the initial Turbulent kinetic energy and specific dissipation rate are mapped using the General Extrusion feature as suggested in COMSOL [2017e] and as explained in Casey & Wintergerste [2000, p.39]. The inlet geometry and description of the inlet model mesh can be found in Appendix C.

5.2.5 Solver for the Fluid Flow Problem

The fluid flow problem is solved as a stationary problem using the default solver provided by COMSOL. Due to the relatively large problem is an iterative solver suggested by COMSOL. The memory requirements for iterative solvers are in general much less than the alternative direct solvers but also less robust. The Navier-Stokes (RANS) model and the turbulence model are solved using a segregated solution algorithm meaning that the equations are

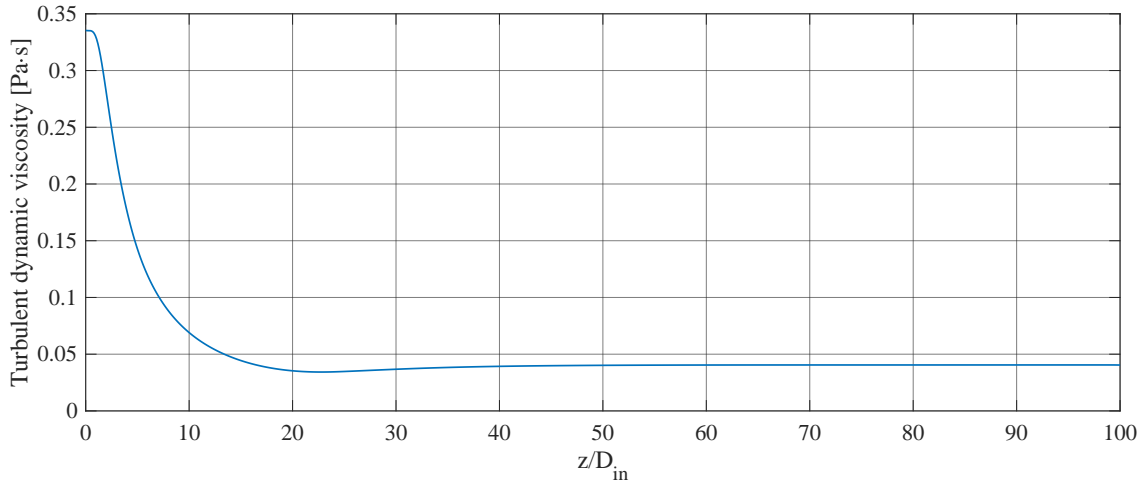


Figure 5.6. The turbulent dynamic viscosity as a function of the normalized length z/D . It can be seen that true hydrodynamic entry length for the fully developed is longer than calculated in Equation 5.4.

solved sequentially. Both the RANS model and the turbulence model are solved using the Algebraic Multigrid solver or Geometric Multigrid solver with GMRES as a preconditioner. The Geometric Multigrid solver for the turbulence model has two levels, and the Geometric Multigrid solver for the RANS model has one level, based on the Degrees of Freedom (DoF) of each model. Other settings are set as default by COMSOL.

5.2.6 Results from Fluid Flow Model

Side views of the fluid flows can be seen in Figure 5.7 for different flow velocities. Note that inlet geometry is extended with an extra length. The extra length is used in the particle tracing which is explained later (See Figure 5.14 in Section 5.3). In Figure 5.7, it can be seen that the flow have strong curvatures in both the inlet and outlet reflector domains and the $k - \omega$ turbulence model, therefore, applies to this problem (see Subsection 5.2.2). The fluid flow in the measurement tube is of most interest since it is here the particles are measured and, therefore, where the particle distribution has the greatest impact to the acoustic field measured by the turbidity transducer. In Figure 5.7, it can be seen that the flow streamlines in the measurement tube change significantly as a function of the flow velocity. A cut view made in the center of the measurement tube can be seen in Figure 4.9 for different inlet flow velocities. Figure 4.9 shows that the flow profile through the measurement tube depends on the flow velocity and it is expected that the particle distribution changes accordingly.

To investigate the actual particle distribution within the flows shown in Figure 5.7 and Figure 5.8, a particle tracing simulation is conducted which is described in the following.

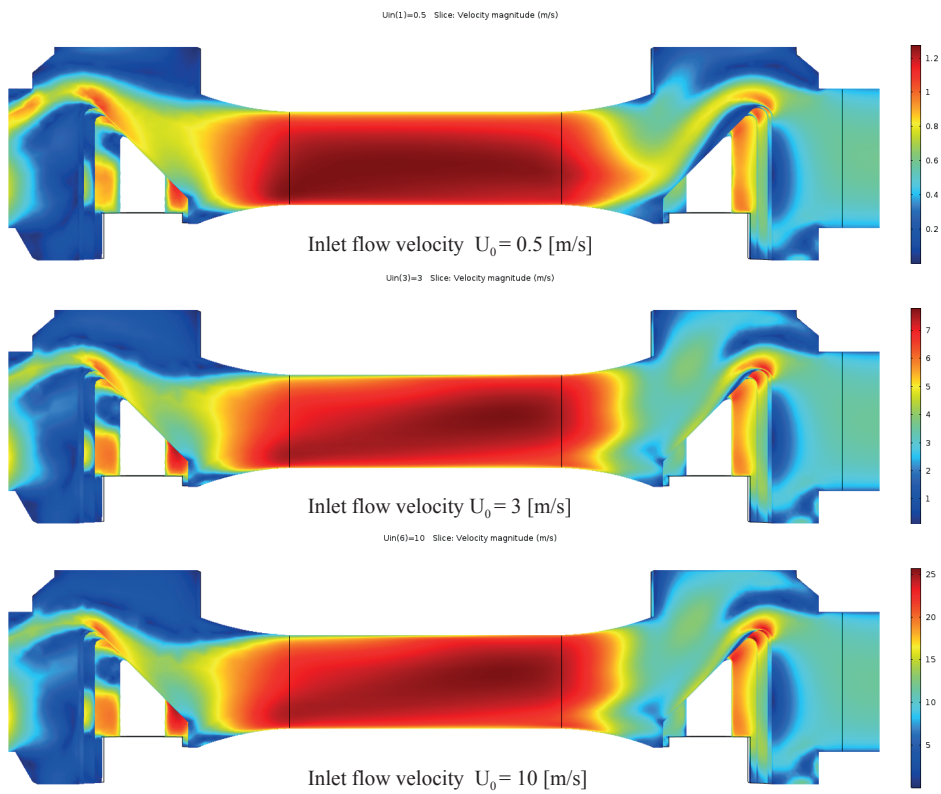


Figure 5.7. Side view of the resulting flow with different inlet flows.

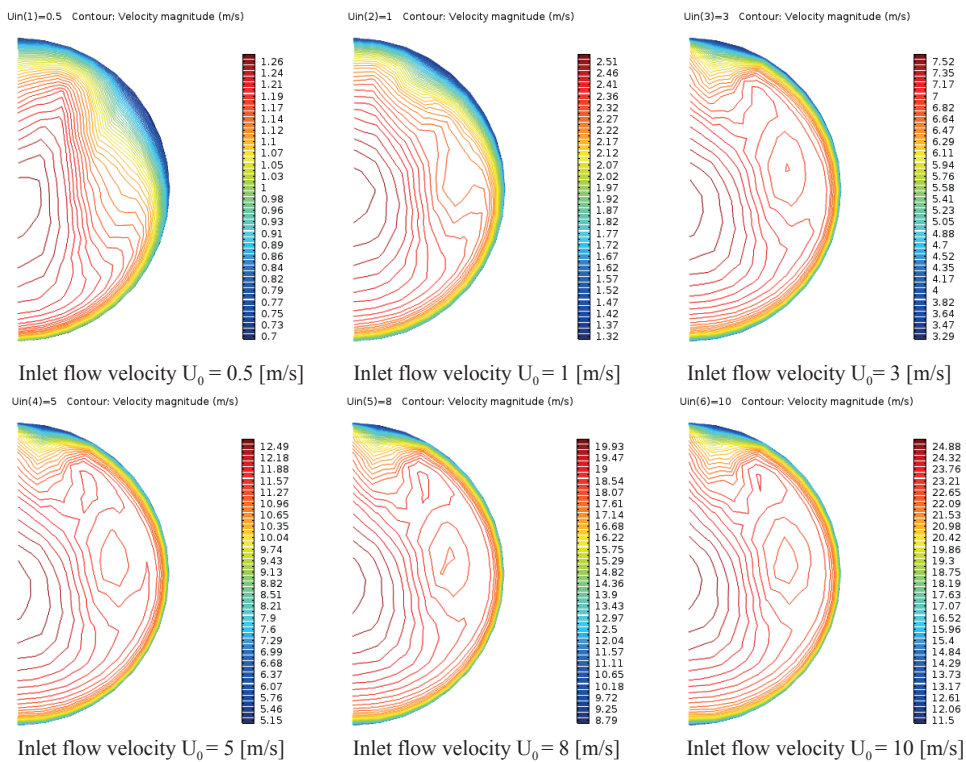


Figure 5.8. Cut view made in the center of the measurement tube, with different inlet flows.

5.3 Particle Tracing

The *Particle Tracing for Fluid Flow* module in COMSOL can be used to simulate the motion of the particles in a fluid flow. Using the Particle Tracing model gives the ability to track the position of the particles at a given time instance, which can then be mapped into an acoustic problem. The particle motion within fluid flows is primarily driven by drag forces if it is assumed that the particle mass is small [COMSOL, 2017g].

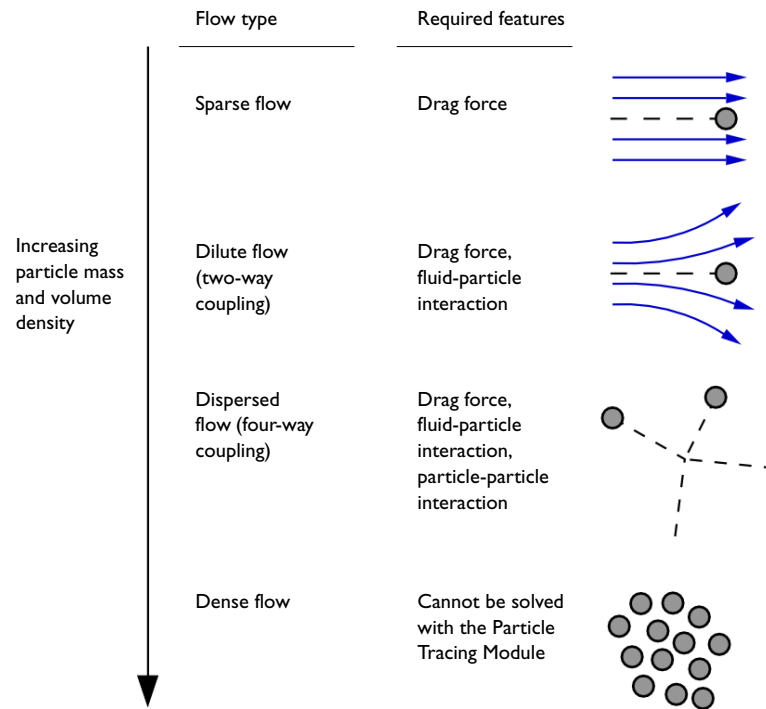


Figure 5.9. Particle-fluid interaction types [COMSOL, 2017g].

The flow type considered in this study is sparse flow meaning that the coupling between the flow and the particle is one-way. The particles in sparse flow does not affect the fluid flow, but the flow affects the particles through a drag force. Large particles or large concentrations of particles require dilute flow or dispersed flow calculations with couplings like the fluid-particles interaction and particle-particle interaction. The volume fraction of the fluid volume and the particle volume should be less than 1%. Larger volume fractions are called dense flows which are not supported in the *Particle Tracing for Fluid Flow* module (Version 5.2a) [COMSOL, 2017g].

The governing equations behind the particle tracing simulations are presented in the following, but a more in-depth explanation can be found in the Particle Tracing Module User's Guide [COMSOL, 2017g].

The particle motion is calculated using Newtons second law as:

$$m_p \frac{d^2}{dt^2} \mathbf{x} = \mathbf{F}(t, \mathbf{x}, \frac{d\mathbf{x}}{dt}) \quad (5.5)$$

where m_p is the particle mass, \mathbf{x} is the particle position and \mathbf{F} is the sum of all the forces acting on the particle.

The main forces acting on the particle are buoyancy force, drag force and gravity force. In this study, it is assumed that both the buoyancy force and gravity force can be neglected and only the drag force \mathbf{F}_D affects the particle trajectory, which is calculated as:

$$\mathbf{F}_D = m_p \frac{\mathbf{u} - \mathbf{v}}{\tau_p} \quad (5.6)$$

where \mathbf{u} is the fluid velocity, \mathbf{v} is the particle velocity, and τ_p is the particle velocity time constant.

The particle time constant τ_p can be calculated using different drag laws, which are valid within specific ranges of the relative Reynolds number Re_r . The relative Reynolds number Re_r is similar to the Reynolds number in Equation 5.1, but with the absolute velocity difference between the particle and fluid flow instead of just the flow velocity (see Equation 5.1). The relative Reynolds numbers Re_r is given as [COMSOL, 2017g]:

$$Re_r = \frac{\rho \|\mathbf{u} - \mathbf{v}\| d_p}{\mu} \quad (5.7)$$

where ρ is the fluid density, d_p is the particle diameter and μ is the fluid dynamic viscosity.

The drag laws investigated in this report are the Stokes drag law, Schiller-Naumann drag law, and COMSOL's Standard Drag Correlation.

The Stokes drag law is the simplest drag law since it does not explicit depend upon the relative Reynolds number. The Stokes particle time constant is given as:

$$\tau_p = \frac{\rho_p d_p^2}{18\mu} \quad (5.8)$$

where ρ_p is the particle density. Stokes drag law is applicable if $Re_p \ll 1$.

The Schiller-Naumann drag law is more sophisticated than the Stokes drag law, due to the explicit dependence on the relative Reynolds number. The Schiller-Naumann drag law can be applied for relative Reynolds number under 800 ($Re_p < 800$) and is given as:

$$\tau_p = \frac{4\rho_p d_p^2}{3\mu C_D Re_r^{0.687}} \quad (5.9)$$

where

$$C_D = \frac{23}{Re_r} (1 + 0.15 Re_r^{0.687}) \quad (5.10)$$

The Standard Drag Correlations consist of an extensive list of drag law relations at different relative Reynolds numbers which can be found in the Particle Tracing Module User's Guide [COMSOL, 2017g]. This drag law can, therefore, be used when the relative Reynolds numbers changes by several orders and can model drag at a higher Reynolds number than the Schiller-Naumann drag law. The Standard Drag Correlations is, however, computationally heavy compared to the Schiller-Naumann drag law and Stokes drag law.

A preliminary study of the relative Reynolds number using the flow field results from Section 5, can be found in Appendix D. In this study, the relative Reynolds number is modeled using the Standard Drag Correlation for different flow velocities. The Standard Drag Correlation is valid for the largest span of relative Reynolds numbers and the locally calculated relative Reynolds numbers can, therefore, be used as an indicator for the maximum expected relative Reynolds number in the model.

In Appendix D, it is found that the relative Reynolds number in this study does not exceed $Re_p = 10$ and the Schiller-Naumann drag law is, therefore, sufficient for this study.

The domain and boundary conditions used for particle tracing study can be seen in Figure 5.10. It can be seen that not the entire fluid domain is used in the particle tracing calculations. The sparse flow calculations only consist of one-way interactions and the particles in the measurement tube are, thus not affected by the particles in the outlet reflector domain (marked with gray in Figure 5.10).

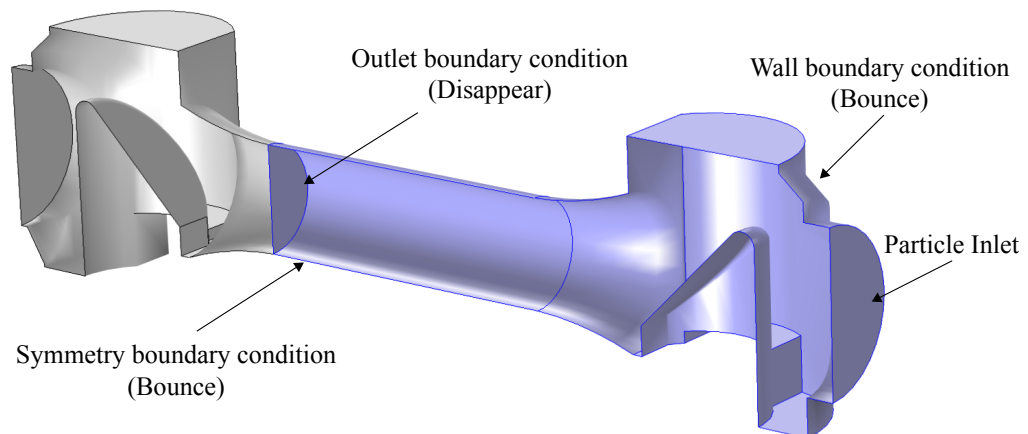


Figure 5.10. The domain for particle tracing simulations with boundary conditions

The boundary conditions for the walls and symmetry surface is a specular reflection (bounce), which means that the particle kinetic energy is conserved and specularly reflected from the wall. At the symmetry surface, a physical interpretation of the specular reflection is that for every particle exiting the surface another particle enters the surface at the same location with the same kinetic energy.

5.3.1 Particle Release Strategy

Simulation of particle trajectories require the particles to enter the domain through a given boundary. The particles can be released in different manners affecting the particle distribution in within the geometry. The particle release strategy, therefore, influences the particle distribution within the measurement tube used later in the acoustic simulations.

Releasing the particles in a structured manner result in particle lumps. The particle lumps are unwanted due to the idea that the particles should enter the domain in a random manner. Using an inlet boundary condition with a random distribution of particles or/and a random number of particle release per time instance would solve the problem if the particles were released at high frequency. The particle release positions are, however, based on the mesh and the particle release can, therefore, not directly be made random.

The approximated density of particles with a random normal disturbance is used to randomize the particle release positions on the inlet boundary. The particle density distribution is, furthermore, made proportional to the previously calculated flow velocity magnitude field. This means that the density of released particles is larger in regions with highest absolute flow velocity magnitude, as would be expected if a long inlet pipe was included in the simulation. Figure 5.11 shows the particle distribution using a freeze boundary condition in the long axes symmetric inlet model. In Figure 5.11, it can be seen that the density of particles is smaller at low flow velocities.

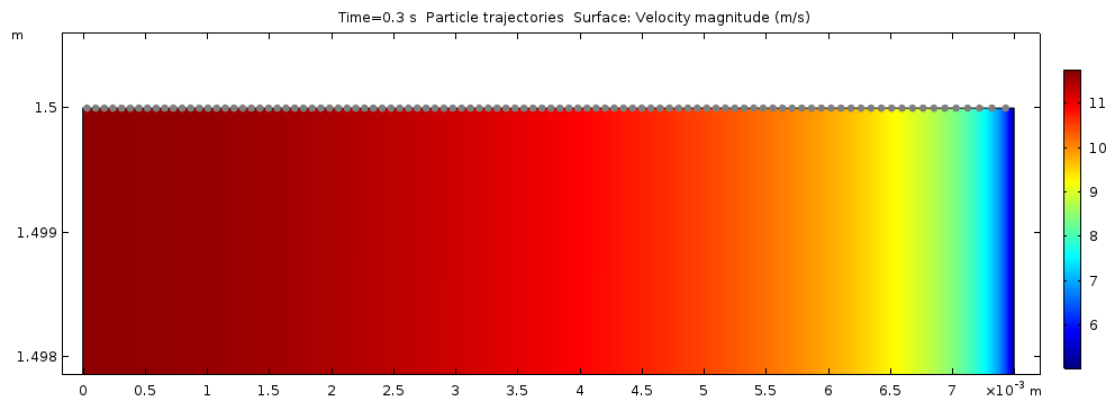


Figure 5.11. Particle distribution (gray dots) at the outlet of inlet model using the freeze boundary condition and a inlet flow boundary condition of 10 m/s . It can be seen that the density of particles is smaller at the low flow velocity then the high flow velocity.

The density of particles is controlled using the non-dimensional density proportionality factor ρ_{release} , which is calculated using the flow velocity amplitude $\text{spf}.\mathbf{U}$ and a random normal disturbance, thus:

$$\rho_{\text{release}} = [1 + \text{normrandom}(\text{spf}.\mathbf{U}, t)] \cdot \text{spf}.\mathbf{U} \quad (5.11)$$

where $\text{spf}.\mathbf{U}$ is a structure with flow velocities at each mesh node and $\text{normrandom}(\text{spf}.\mathbf{U}, t)$ is a normal distributed random function in both time and space. The initial velocity of

the particles is also set to the flow velocity magnitude. A boundary release of particles at the inlet using the random density proportionality factor in Equation 5.11 can be seen in Figure 5.12 and a side cut of the inlet can be seen to the right in Figure 5.12.

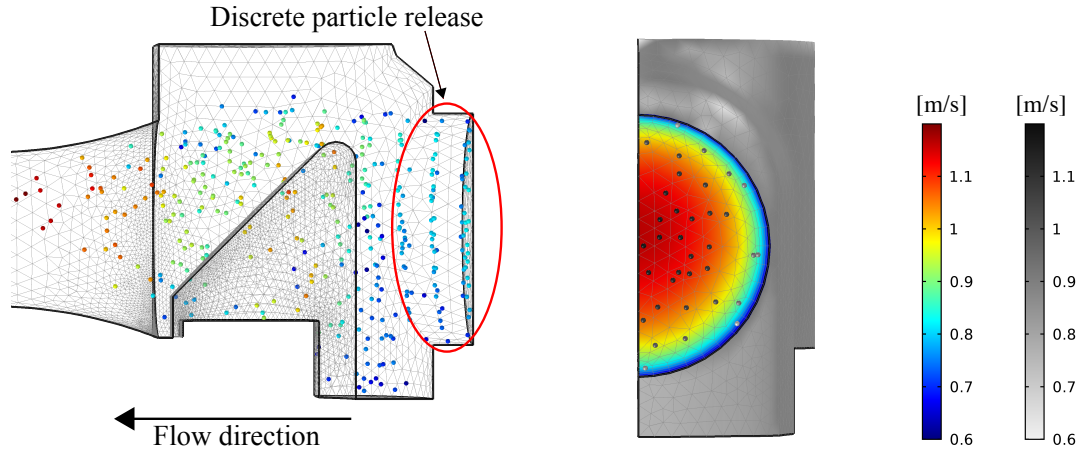


Figure 5.12. Particles ($a = 5 \mu m \times 30$, $N = 100$, $U_0 = 1 m/s$) released using the inlet boundary condition. The figure to the left shows the particle released in a discrete manner. In the figure to the right shows the distribution of particles that is mesh and flow velocity (with random disturbance) dependent. Note, the particle positions at next time instant is different (not shown), due to the random release.

From Figure 5.12, it can be seen that the particles are not released such that the stream of particles is continuous. This results in lumped distributions of particles in the measurement tube, which is not expected in a physical setup. The problem can be addressed by releasing a low amount of particles at a high frequency. This is, however, not computationally feasible.

Another way to make sure that the particles are released such that the particle stream is continuous is by extruding the inlet. Releasing the particles in the new extruded volume, results in a volume release instead of a boundary release. The volume release makes it possible to generate particles randomly both in the direction of the flow and tangent to the flow. The new inlet domain can be seen in Figure 5.13. The domain release node in the Particle Tracing for Fluid Flow module allow the user to release particles in the same manner as the inlet boundary condition, but with initial positions in three dimensions instead of two dimensions as for the inlet boundary condition. Figure 5.14 shows the volume release leading to a continuous stream of particles with an inlet velocity of $U_0 = 1 m/s$.

As described in the Problem Statement (see Chapter 3), it is desired to have a particle concentration ρ_{pc} from 100 p/mL to 6000 p/mL within sensor geometry. The time between each release $\Delta t_{release}$ and number of particles per release $N_{release}$ can be calculated using

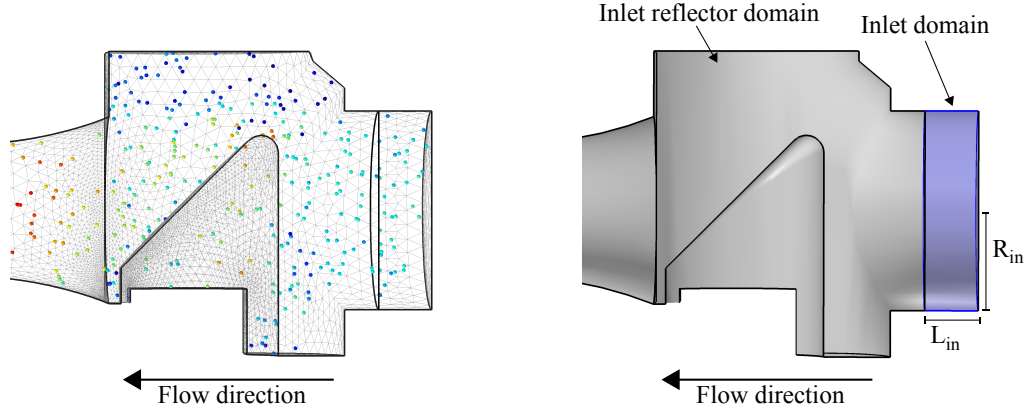


Figure 5.13. Inlet extruded into an inlet domain which is marked on the geometry.

Figure 5.14. Continuous random stream of particles using the inlet domain and a domain release node.

the mean inlet flow velocity, as:

$$N_{\text{release}} = V_{\text{inlet}} \cdot \rho_{\text{pc}} \quad (5.12)$$

$$\Delta t_{\text{release}} = V_{\text{inlet}} \cdot L_{\text{inlet}} \quad (5.13)$$

where $V_{\text{inlet}} = \pi R_{\text{in}}^2 L_{\text{inlet}}$ is the inlet release volume with inlet radius R_{in} , and inlet domain length L_{inlet} .

The particle simulation is a time-domain problem and only a single time instance is needed for the acoustic simulation where it is assumed that steady-state conditions have been reached. The average time it takes for the particles to pass the entire sensor geometry L_{sensor} can be calculated as $L_{\text{geom}}/\mathbf{v}_{\text{avg}}$, where \mathbf{v}_{avg} is the average particle velocity. It can be found that a proportion of the particles gets stocked in vortexes within the inlet reflector domain (see Figure 5.7) and different time constants for the number of particles (NoP) are observed when releasing the particles (see Figure 5.15).

The NoP in the measurement tube counted over a period of time can be used to find the time instance where the change in NoP is zero ($d\text{NoP}/dt = 0$) indicating that particle steady-state conditions has been reached. The time instance where NoP rate is zero is defined as the particle convergence time instance.

It is convenient to determine a non-dimensional factor that can be used to relate the simulation time t_{sim} independent of inlet flow velocities. The non-dimensional factor is calculated as:

$$N_{\text{sim}} = \frac{t_{\text{sim}}}{L_{\text{sensor}}/U_0} \Rightarrow t_{\text{sim}} = \frac{L_{\text{sensor}}}{U_0} \cdot N_{\text{sim}} \quad (5.14)$$

The desired number of particles within the measurement tube together with the counted number of particles in the measurement tube, for three different particle concentrations, can be seen in Figure 5.15. The desired number of particles within the measurement tube is calculated as $N_{\text{p,tube}} = V_{\text{tube}} \cdot \rho_{\text{pc}}$ with $V_{\text{tube}} = 1.155\text{mm}^3$.

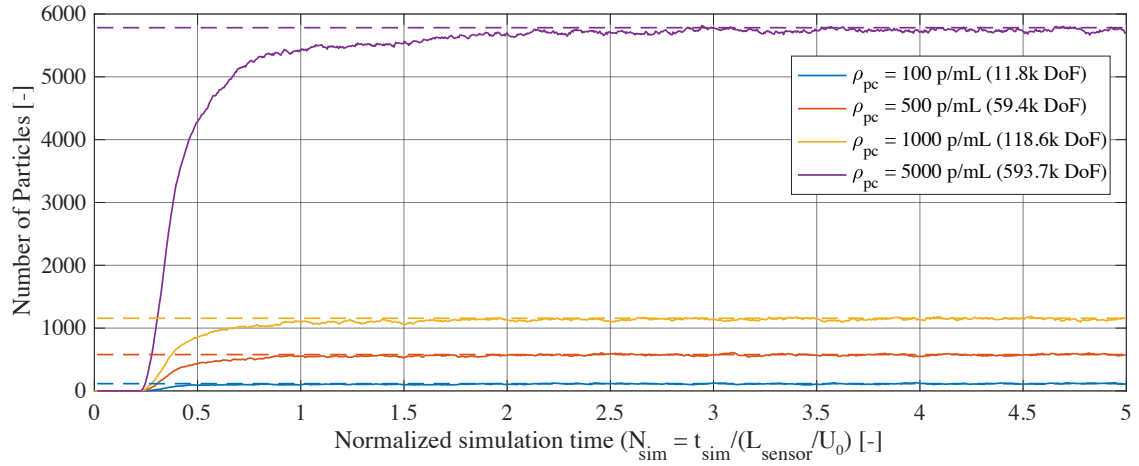


Figure 5.15. Number of particles in the measurement tube with different particle concentration levels

Figure 5.15 shows the NoP approximately converge after $N_{sim} = 3$. It can also be seen that convergence of the NoP is divided into two phases. The first phase from $N_{sim} = 0$ to approximately $N_{sim} = 1$ consist of the particles that follow the fast main flow and the second phase from approximately $N_{sim} = 1$ to $N_{sim} = 2$, where particles from slow flow regions are released into the main flow and therefore lastly encountered in the measurement tube. The main part of the slow flow regions can be found in the upper part of the inlet reflector domain (see Figure 5.2).

5.3.2 Particle Tracing Results

Using the flow field calculated in the CFD model as described in Section 5, the particle trajectories can be calculated. Figure 5.16 shows the particle positions at the particle concentration convergence time instance with different particle concentrations. The particles have a radius of $5 \mu m$ and are in Figure 5.16 upscaled 30 times, to make the particles more visible.

Figure 5.17 shows the particle trajectories at different inlet flow velocities and with a constant particle concentration of 100 p/mL. In Figure 5.17, it can clearly be seen that the particles circulate in the top region of the inlet reflector domain, which is the reason for the different time constants seen in the particle concentration convergence plot in Figure 5.15. It can also be seen that the particle trajectories rotates inside the measurement tube and that the particle trajectories rotation increases as the flow velocity increases.

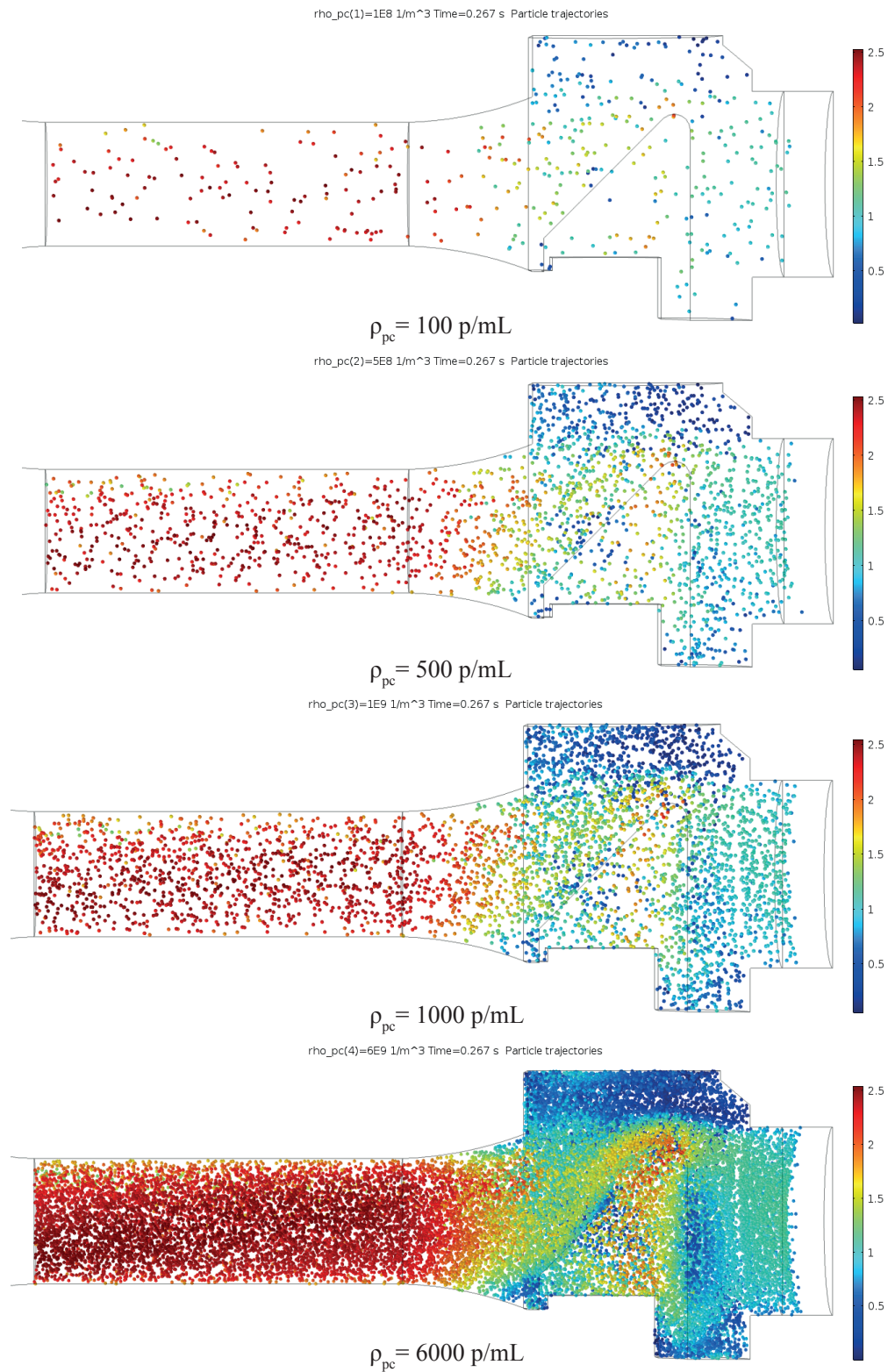


Figure 5.16. The simulated particles inside the UT sensor, seen from the side. The particle concentration ρ_{pc} is changed through each figure, but the flow velocity remains constant $U_0 = 1 \text{ m/s}$

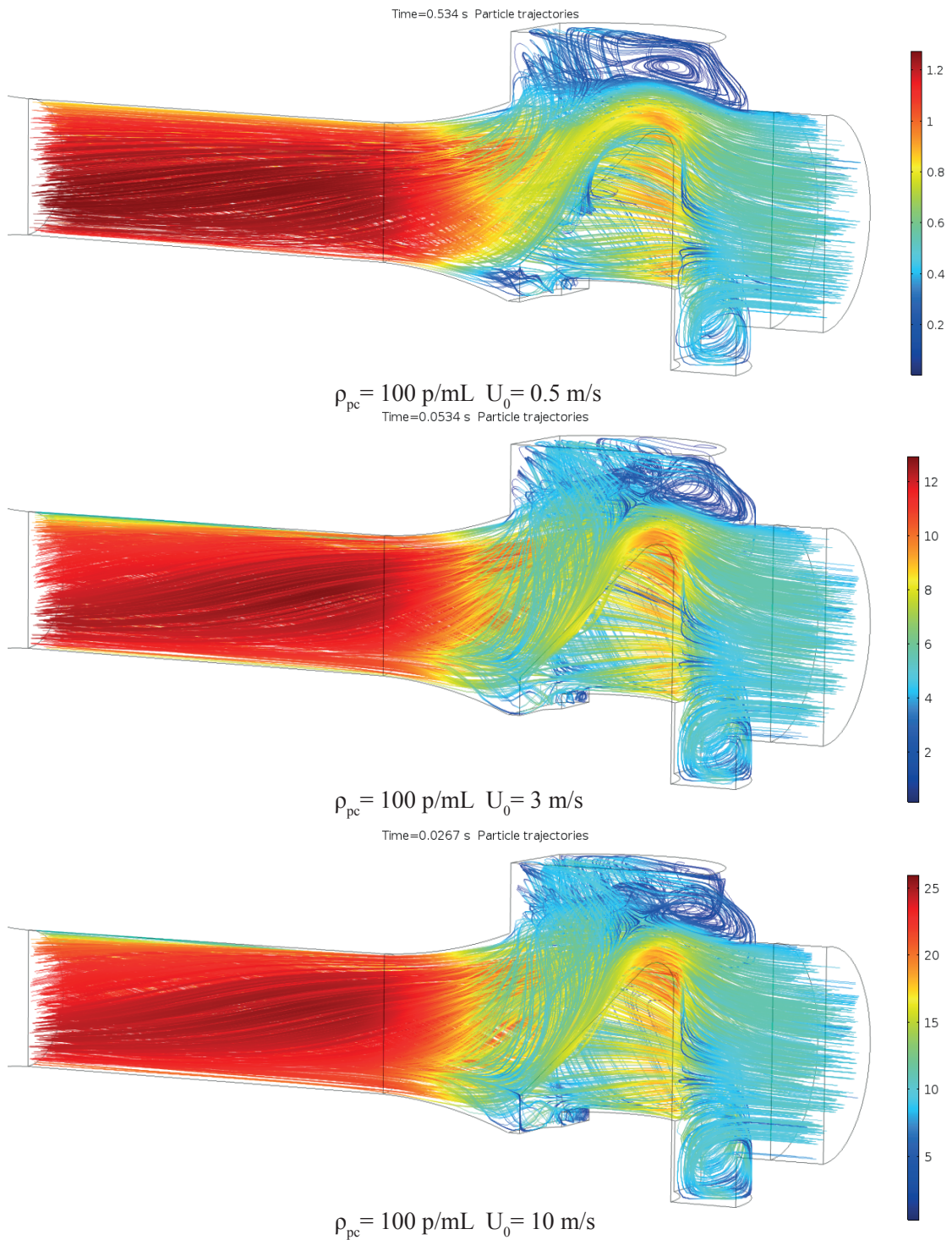


Figure 5.17. The particle trajectories with a particle concentration of 100 p/m^3 and different flow velocities. It can be seen that there are particle encirclements in the top region of the inlet reflector domain, as described in Subsection 5.3.1.

COMPUTATIONAL ACOUSTICS

The second stage of the modeling framework is the computational acoustics which can be seen in the diagram in Figure 6.1. This chapter contains an analysis of the acoustic numerical method used in this work, including a mesh analysis, solver analysis and a description of the domain truncation method utilized in this work. The numerical analysis is based on a simple geometry with only one particle, that can be related to the analytical solution found in Section 2.2.

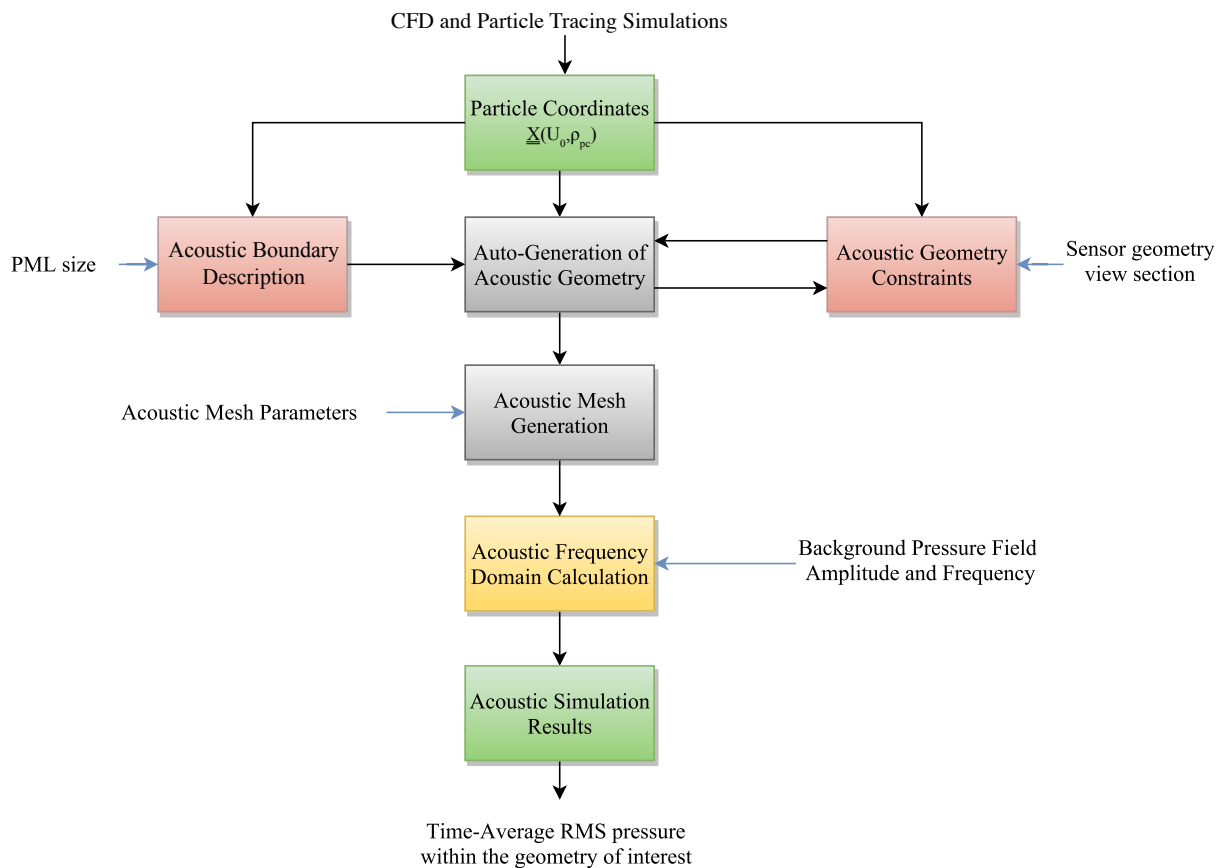


Figure 6.1. Diagram of the second stage, that contains the acoustic geometry generation, acoustic computation, and evaluation of the scattering pressure field. The inputs to the second stage are the particle coordinates, properties for the acoustic generation algorithm, mesh parameters, and background pressure field properties.

The sketch of the main principles behind the UT sensor as described in the introduction (see Chapter 1) is reshowed for convenience in Figure 6.2.

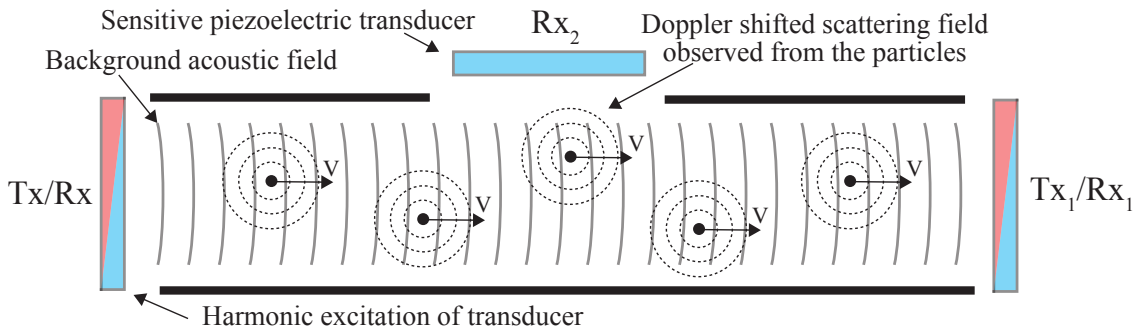


Figure 6.2. Particles scattering in a background acoustic field, where the scattering frequency is Doppler shifted due to the relative movement of the particles in the stationary background field.

As described in the introduction, the Doppler effect is crucial regarding the ability decouple the signal of the wave scattered by the particles from the background excitation wave. Modeling the Doppler effects seen in Figure 6.2 is a time-domain problem, with moving objects and high-frequency wave propagation. Moving the objects can be modeled numerically using a moving mesh approach. This method is, however, difficult due to ill-condition issues leading to numerical errors at the interface between the moving mesh and the stationary mesh. Another important point is the spherical geometry of the particle. A spherical geometry cannot be represented in two-dimensions (2D) or lower, and a three-dimensional (3D) simulation is, therefore, needed. Circles as illustrated in Figure 6.2, represent cylinders in space which has a very different scattering response compared to spheres. Spherical waves act much like plane waves as seen in Section 2.2 and do not change shape as they propagate far from the scattering, but only diminish in amplitude with the factor $1/r$. Cylindrical waves, on the other hand, both diminishes in amplitude and changes shape when propagating, leaving a wake behind.

A 3D time-domain acoustics simulation with moving mesh and high frequency wave propagation is a rather computationally expensive and numerically unstable task.

An alternative to the time-domain study is a frequency domain study. Assuming that the excitation of the background wave is time-harmonic, a frequency domain simulation of the scattering would lead to the same result as a time-domain solution. The Doppler effect can, however, not be represented in the frequency domain simulation, which is not a problem because the frequency domain simulation allow the scattering field to be decoupled directly from the background field making the Doppler effect unnecessary. In the frequency study, the background field can be applied as a pre-known analytical expression and the scattering field can, therefore, be calculated from the total acoustic field as:

$$p_t = p_b + p_{sc} \quad (6.1)$$

where p_t is the resulting pressure field, p_{sc} is the scattering pressure field, and p_b is the pre-known analytical expression of the background pressure field.

Numerical acoustic problems with frequencies in the MHz range have millions of DoF per mm^3 , due to strict requirements for the mesh size. Conducting an acoustic simulation of the entire UT sensor geometry is, therefore, not possible as this problem would have an extreme size. To reduce the size of the problem only the inner section of the measurement tube is considered for the analysis of the scattered field. The domain of interest is marked with a green color in Figure 6.3.

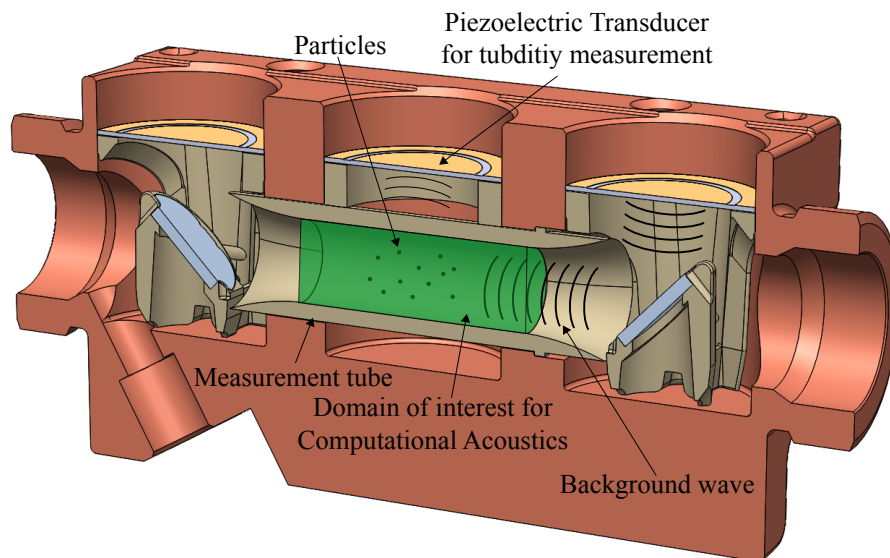


Figure 6.3. Turbidity sensor, with the acoustic computational domain marked with green.

The scattering pressure on the surface of the acoustic computational domain can be related directly to the scattering pressure experienced by the turbidity transducer seen in Figure 6.3. The surface scattering pressure is, hence the final product of the acoustic analysis as this reduces the problem significantly. The surface of the measurement tube is further assumed to be non-reflecting making it easier to determine the acoustic scattering field.

In the following, it is assumed that the background pressure wave propagating through the measurement tube is a perfect plane wave in the direction aligned with the inner part of the measurement tube.

6.1 The Acoustic Frequency Domain Model

The frequency domain or time-harmonic study branch in COMSOL utilizes the inhomogeneous Helmholtz equation given as [COMSOL, 2017b]:

$$\nabla \cdot \left(-\frac{1}{\rho_c} (\nabla p_t - \mathbf{q}_d) \right) - \frac{k^2 p_t}{\rho_c} = Q_m \quad (6.2)$$

where \mathbf{q}_d is the dipole domain source and Q_m is the monopole domain source. In the problem of this work, no sources are introduced, and Equation 6.2 reduces to the homogeneous Helmholtz equation

$$\nabla^2 p_t + k^2 p_t = 0 \quad (6.3)$$

which is equal to the Helmholtz equation found in Section 2.2 if p_t is replaced with p . The total pressure p_t is given in Equation 6.1 and the expression for the background pressure p_b utilized in this work, is a plane wave background field given by [COMSOL, 2017b]:

$$p_b = p_0 e^{-i\mathbf{k} \cdot \mathbf{x}} = p_0 e^{-ik \frac{\mathbf{x} \cdot \mathbf{e}_k}{\|\mathbf{e}_k\|}} \quad (6.4)$$

where \mathbf{k} is the wave number vector, $k = \frac{\omega}{c}$ is the wave number amplitude, \mathbf{e}_k is the wave direction and \mathbf{x} is the coordinate vector.

Geometries with a pressure background field applied to only some of the domains are controlled automatically by COMSOL using a continuity condition at the internal boundaries between domains with and without the pressure background field. This feature is used later for the damping layers.

6.2 Analysis of Numerical Scattering

The large computational domain seen in Figure 6.2 with the particles calculated from the combined fluid flow and particle tracing study (see Chapter 5) results in a large multi-scattering problem with millions of DoF, to be solved. Important aspects like geometry size, mesh size, and solver selection can significantly reduce the total computational time if chosen with care.

In order to analyze the numerical acoustic problem, a simplified version of the computational domain seen in Figure 6.2 is conducted. The simplified model consists of a single rigid particle placed in the center of the computational domain. The domain surrounding the particle has the form of a half cylinder with damping layers on the outer boundaries and the material properties of water are applied to both the damping layers and the fluid domain. The geometry of the simplified model can be seen in Figure 6.4. The damping layers in Figure 6.4 are used to emulate an open domain problem utilizing perfectly matched layers (PML). The PML damping layer is described more in depth in Subsection 6.2.2. In the analysis of this section, it is assumed that the background pressure

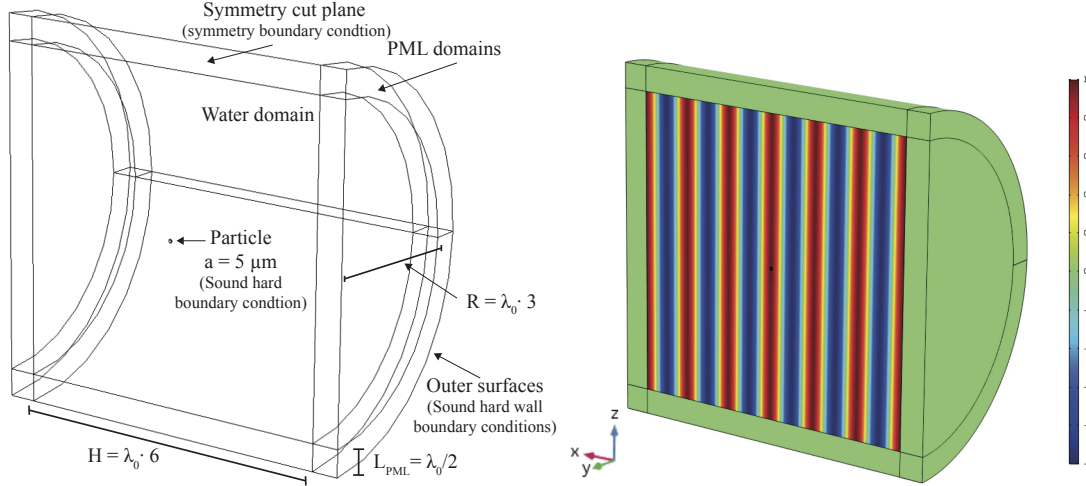


Figure 6.4. Geometry of the simplified model **Figure 6.5.** 10MHz plane background wave with an unit amplitude applied to the fluid domain.

wave is a 10MHz plane background wave with an unit amplitude, applied only to the fluid domain. The background wave can be seen in Figure 6.5.

Using the simplified model with a single particle only require a small computational domain, which reduces the computational time from hours to seconds. Also, the analytical solution to the scattering problem of a single sphere has already been shown in Section 2.2, which is utilized as a reference in various occasions throughout this section.

6.2.1 Meshing the Acoustic Domain

The three-dimensional geometry as seen in Figure 6.4 consists of a fluid domain and multiple PML domains. The fluid domain is discretized using the, by COMSOL, default free tetrahedral method which is a robust way of discretizing the geometry for computational acoustics. The fluid domain is meshed using a maximum element size n_{\max} , a minimum element size n_{\min} , a maximum growth rate of 1.2, a curve factor of 0.6 and resolution in narrow regions of 1. A comparison between different mesh curve factors and growth rates can be found in Appendix E. The maximum element size n_{\max} is determined using a Nyquist-like approach relating the maximum mesh-element size to some portion of the wavelength $\lambda_0 = c/f_0$, that is:

$$n_{\max} = \frac{\lambda_0}{N} = \frac{c}{N \cdot f_0} \quad (6.5)$$

where N is a mesh scaling factor, c is the speed of sound in the material and f_0 is frequency of the wave. The minimum element size is controlled by a proportion of particle size, through the following relation:

$$n_{\min} = \frac{a}{N} \quad (6.6)$$

where a is the particle size.

The PML domains in the simplified model has a thickness of $\lambda_0/2$ and are meshed using a structured swept mesh with 30 layers, giving a high performance of the PML (see Section 6.2.2) and the reflections from the PML can be treated as is minimal. At the boundaries between the PML domains and the fluid domain, a single-layered boundary layer mesh is utilized as suggested in COMSOL [2017b]. The boundary layer mesh is utilized to enhance the calculation of normal derivative of the pressure at the boundary, used in the calculation of the pressure level and acoustic intensity. The boundary layer thickness is chosen to be $\lambda_0/N/10$ as suggested in the application note COMSOL [2017a].

The simplified geometry with the mesh size parameters as explained before, $N = 8$ and $f_0 = 10\text{MHz}$, can be seen in Figure 6.6 and a zoom at the particle mesh can be seen in Figure 6.7.

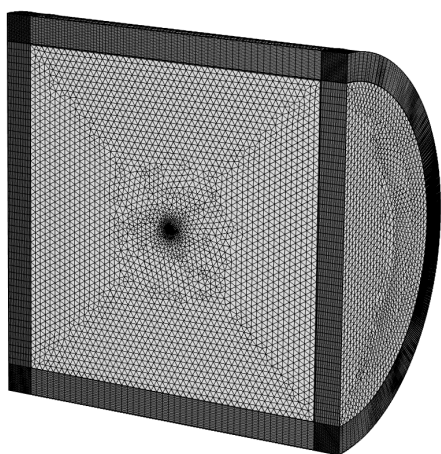


Figure 6.6. Free tetrahedral in the fluid domain and swept mesh in the PML domains. Important settings are $N = 8$, $f_0 = 10\text{MHz}$, $a = 5 \mu\text{m}$.

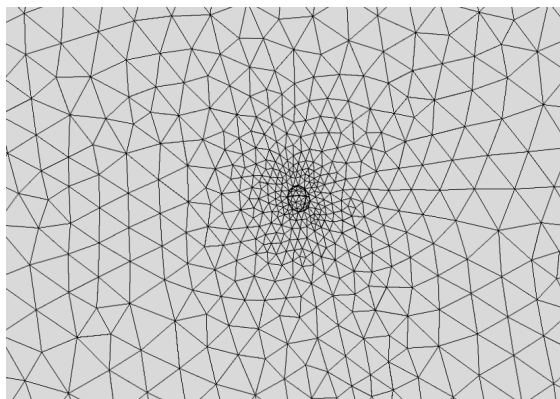


Figure 6.7. Zoom of the mesh around the particle, with a curvature factor of 1.2 and growth rate of 0.6. The mesh around the particle is controlled mainly by the minimum mesh size and the curvature factor.

From Figure 6.7, it can be seen that the mesh size close to the particle is finer than the mesh further away from the particle. A finer mesh is needed, due to large pressure gradients found near the particle. The mesh near the particle is mainly controlled by the minimum mesh size and the curvature factor (see Appendix E).

Mesh Convergence Analysis

In order to evaluate the precision of the model with different mesh settings, the solution of a numerical evaluation of the scattering problem using a single particle is compared to its analytical solution. Figure 6.8 shows the interpolated numerical scattering solution evaluated on the symmetry cut plane (see Figure 6.4) with the mesh shown in Figure 6.6.

Figure 6.9 shows the corresponding interpolated analytical solution. The green dots seen in Figure 6.8 and Figure 6.9 are the original numerical and analytical solutions respectfully.

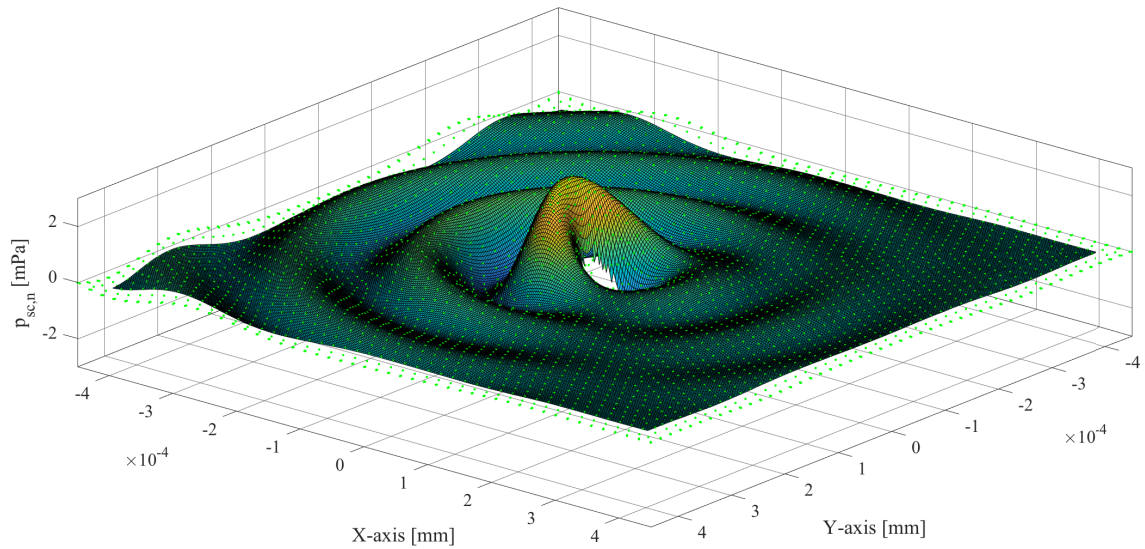


Figure 6.8. Scattering pressure on the symmetry cut plane, with background pressure of 10MHz, particle size of $5 \mu\text{m}$ and the mesh seen in Figure 6.6 ($N = 8$). Note the green dots are solutions points exported from COMSOL and the surface is the interpolated solution with a step size of $\lambda_0/50$

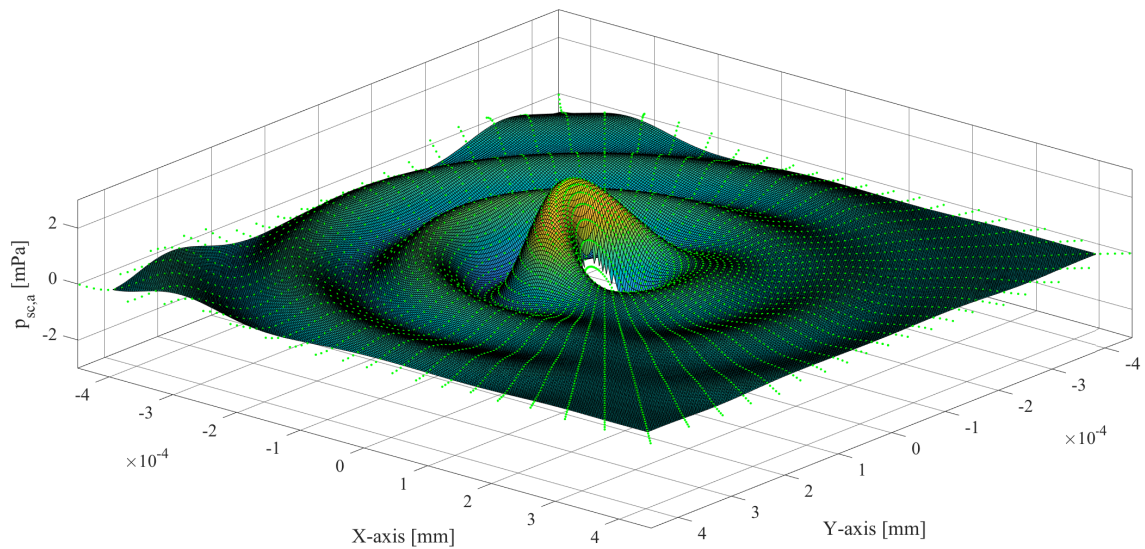


Figure 6.9. Analytical solution to the scattering problem using the same properties as the numerical. The green dots are the spherical solution points and the surface is the interpolated solution with step size of $\lambda_0/50$.

It can clearly be seen that the coordinates of the green dots in Figure 6.9 and Figure 6.8 does not match, making it difficult to relate the analytical solution with the numerical solution. A cubic interpolation of the original scattering solutions with a constant spacing of $\lambda_0/50$, using the *griddata* function in Matlab is, therefore, utilized. Using the interpolated data,

the numerical and analytical solutions to the scattering field can be related directly. The interpolated solution points in a circle with a radius of 5 times the radius of the particle are removed, due to interpolation problems close to the particle. The mesh near the particle is controlled by the curvature factor, thus not a function of N and the overall results of the mesh convergence analysis is not altered by the removing the points close to the particle.

The numerical error is evaluated using the relative accumulated error given as [Kaltenbacher, 2015]:

$$E_{\text{total}} = \sqrt{\frac{\sum_{i=1}^M (p_i^{\text{sc,a}} - p_i^{\text{sc,n}})^2}{\sum_{i=1}^M (p_i^{\text{sc,a}})^2}} \cdot 100\% \quad (6.7)$$

where M is the total number of interpolated element nodes, $p^{\text{sc,n}}$ is the interpolated analytical solution to the scattering field and $p^{\text{sc,n}}$ is the interpolated numerical solution to the scattering field. Note the notation $p^{\text{sc,n}} = p_{\text{sc,n}}$ and $p^{\text{sc,a}} = p_{\text{sc,a}}$.

The relative accumulated error as a function of the mesh scaling factor N can be seen in Figure 6.10, together with the total simulation time. In Figure 6.10, it can be seen that the relative accumulated error converges after approximately $N = 8$ and only a minimal enhancement in model precision is gained using a larger N .

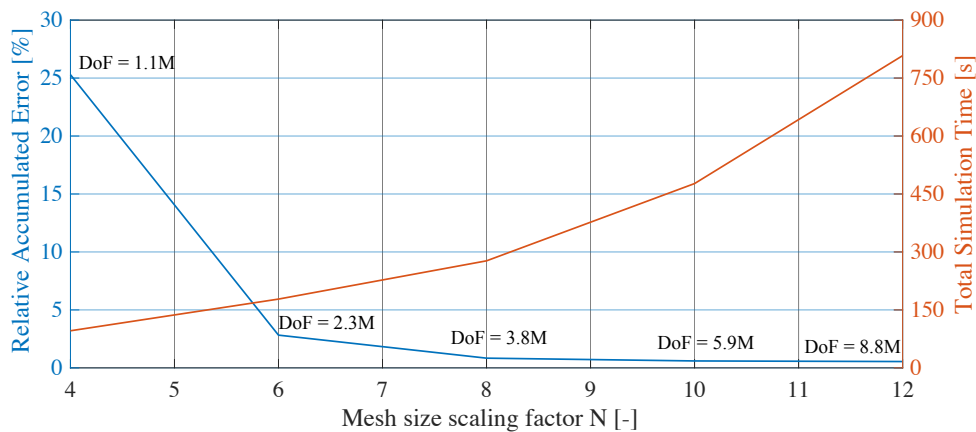


Figure 6.10. Relative Accumulated Error and Total Simulation Time as a function of the mesh scaling parameters N . The total simulation time is the simulation time plus the meshing time.

Examining Figure 6.10, it can be seen that the relative accumulated error does not decrease further to zero as the mesh size is made smaller. This may be a result of other numerical errors related to the computation of the scattering field or reflections from the PML that is not ideal. The numerical errors related to the computation of the scattering field is evident at low mesh resolutions. Figure 6.11 shows the difference between the analytical solution $p_{\text{sc,a}}$ and the numerical solution $p_{\text{sc,n}}$ with a mesh scaling factor of $N = 4$. In Figure 6.11, it can be seen that artifacts from the background plane wave can be found in the scattering solution.

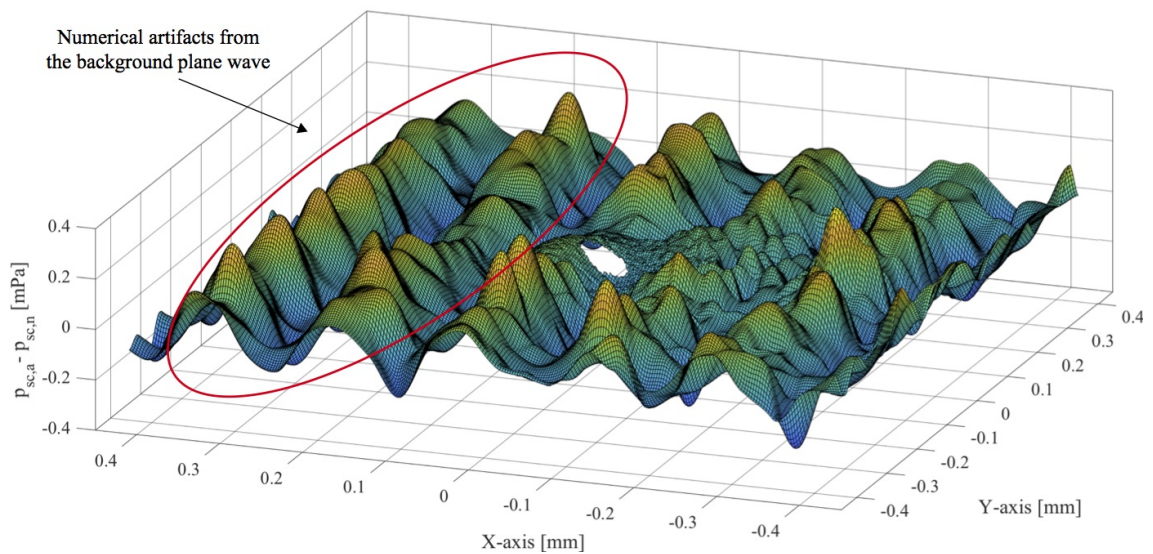


Figure 6.11. Difference between the numerical and analytical solution with a rigid particle of the size $a = 5\mu\text{m}$, a background frequency of 10MHz and with a mesh scaling factor of $N = 4$. Numerical artifacts are marked on the figure.

From Figure 6.10, it can be seen that a good compromise between simulation time and precision can be found using the mesh scale $N = 8$, thus used in the remaining of this work.

6.2.2 Perfectly Matched Layers

Acoustic problems involving scattering are often treated as open-domain problems, meaning that the domain is truncated using appropriate absorbing methods or boundary conditions. An outgoing wave not absorbed, influences the scattering field through reflections from the computational domain boundaries. Some of the methods used to absorb outgoing waves are matching layers, radiation boundaries, and perfectly matched layers (PML) [Berenger, 1994]. In this work, the PML method is of interest due to the robustness toward unknown wave types and unknown angles of incidence. The PML used in the simplified model has already been shown in Figure 6.4 and the principle is alike for the final model. In the following, a thoroughgoing description of the PML properties is presented. The deviations found in this subsection follows approaches found in [Berenger, 1994] and [Kaltenbacher, 2015].

An incident plane wave propagating along the x-axis and striking a boundary between two different mediums can be seen in Figure 6.12 to the left. Because of continuity across the boundary, a system of equations for the pressures and velocities can be set up from which it can be found that the proportion of the incident wave reflected can be calculated as:

$$R = \frac{\tilde{z} - z}{\tilde{z} + z} \quad (6.8)$$

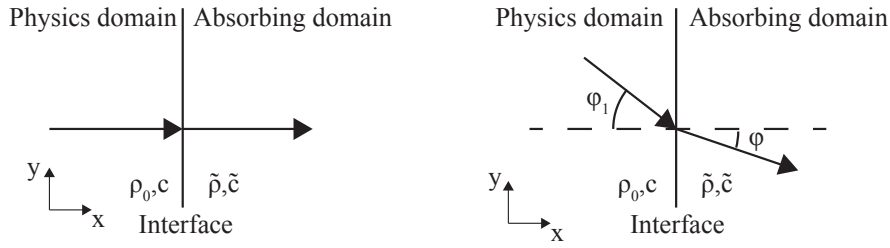


Figure 6.12. The left figure shows a plane wave normal to the interface and the right figure shows a plane wave oblique to the interface

where $z = \rho_0 \cdot c$ and $\tilde{z} = \tilde{\rho} \cdot \tilde{c}$ are the acoustic impedances on either side of the boundary. From Equation 6.8, it can clearly be seen that the wave reflected at the boundary is zero if $z = \tilde{z}$, meaning that the impedance in the two domains are matched. The absorbing domains seen in Figure 6.12, are outside the physics domain and, $\tilde{\rho}$ and \tilde{c} does not need to have any direct physical meaning. Assuming that the plane wave in Figure 6.12 to the left, travels along the x-axis, $\tilde{\rho}$ and \tilde{c} can be chosen as:

$$\tilde{\rho} = \rho_0(1 + i\sigma_0) \quad \tilde{c} = \frac{c}{1 + i\sigma_0} \quad (6.9)$$

where σ_0 is a damping coefficient or function.

Inserting the complex $\tilde{\rho}$ and \tilde{c} into the Helmholtz equation (see Section 2.2), yields:

$$\frac{\partial^2 p}{\partial x^2} + \frac{\omega^2}{\tilde{c}^2} p = 0 \implies \frac{\partial^2 p}{\partial x^2} + \frac{\omega^2}{c^2} (1 + i\sigma_0)^2 p = 0 \quad (6.10)$$

Assigning $\tilde{k} = \frac{\omega}{c}(1 + i\sigma_0)$ the complex wave number, the general solution to Equation 6.10 can be found to be:

$$p = \hat{p} e^{i\tilde{k}x} e^{-i\omega t} = \hat{p} e^{ikx} e^{-\sigma_0 x} e^{-i\omega t} \quad (6.11)$$

From Equation 6.11 it can be seen that the plane wave is damped by a factor σ_0 and both impedance matching and wave absorption is achieved. However, if the wave is traveling obliquely to the boundary as seen to the right in Figure 6.12, both impedance matching and damping cannot be conducted as for the perpendicular case.

To be able to conduct an impedance matched and damping absorption layer for oblique waves, the pressure p_d and velocity v_d are decomposed into its associated Cartesian components (other coordinate systems can also be used). In this derivation only two dimensions are considered, and the pressure and acoustic velocity is written as $p_d = p_x + p_y$ and $v_d = v_x + v_y$ respectfully. Introducing an artificial damping in the linear conservation of momentum (see Equation 2.6) and the linear continuity equation (see Equation 2.5), gives [Berenger, 1994]:

$$\frac{\partial p_x}{\partial t} + \sigma_x p_x = -\rho_0 c^2 \frac{\partial v_x}{\partial x} \quad \frac{\partial p_y}{\partial t} + \sigma_y p_y = -\rho_0 c^2 \frac{\partial v_y}{\partial y} \quad (6.12)$$

$$\frac{\partial v_x}{\partial t} + \sigma_x v_x = -\frac{1}{\rho_0} \frac{\partial (p_x + p_y)}{\partial x} \quad \frac{\partial v_y}{\partial t} + \sigma_y v_y = -\frac{1}{\rho_0} \frac{\partial (p_x + p_y)}{\partial y} \quad (6.13)$$

where σ_x and σ_y are damping functions. Taking only the equations for the pressure and acoustic velocity for the x-axis and setting the damping function $\sigma_x = c \cdot \sigma_0$, then the harmonic solution can be found to be as shown Equation 6.11. The decomposition of the pressure and velocity, allow the total pressure to be expressed in terms of its x and y components. Thus, a two-dimensional spherical wave as seen in Figure 6.13 can be treated as two individual one-dimensional plane waves of the form shown in Equation 6.11, which result in a theoretical reflectionless boundary [Berenger, 1994]. In Figure 6.13, it can be seen that the decomposition allow σ_x and σ_y to be assigned individually to domains with its associated component normal to the physical domain.

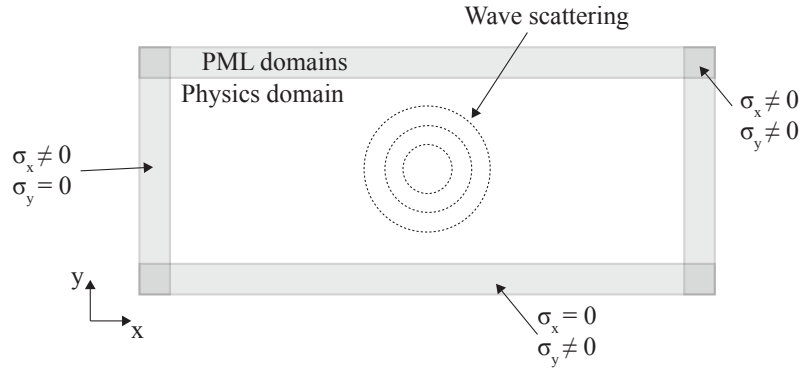


Figure 6.13. The decomposition allow individual assignments of the PML domains.

Assuming that the incident wave is a plane wave oblique to the boundary of the PML as shown to the right in Figure 6.12, a time harmonic description of the pressure and velocity with respect to the x-axis can be written as:

$$p_x = \hat{p}_x e^{i(\tilde{k}_x x + \tilde{k}_y y)} e^{-i\omega t} \quad p_y = \hat{p}_y e^{i(\tilde{k}_x x + \tilde{k}_y y)} e^{-i\omega t} \quad (6.14)$$

$$v_x = \hat{v} \cdot \cos(\varphi) e^{i(\tilde{k}_x x + \tilde{k}_y y)} e^{-i\omega t} \quad v_y = \hat{v} \cdot \sin(\varphi) e^{i(\tilde{k}_x x + \tilde{k}_y y)} e^{-i\omega t} \quad (6.15)$$

where \tilde{k}_x and \tilde{k}_y are the unknown complex wave numbers, \hat{p}_x and \hat{p}_y are pressure amplitudes and \hat{v} is the velocity amplitude.

Inserting the equations for the time-harmonic pressures (see Equations 6.14) into the linear continuity equations with damping (see Equations 6.12) and isolating for the pressure amplitudes \hat{p}_x and \hat{p}_y , yields:

$$\hat{p}_x = \frac{i c^2 \tilde{k}_x \rho_0 v_0 \cos(\varphi)}{i\omega - \sigma_x} \quad (6.16)$$

$$\hat{p}_y = \frac{i c^2 \tilde{k}_y \rho_0 v_0 \sin(\varphi)}{i\omega - \sigma_y} \quad (6.17)$$

Inserting Equation 6.16 and Equation 6.17 into the linear conservation of momentum with

damping (see Equations 6.13) gives:

$$\cos(\varphi)(-i\omega + \sigma_x) = c^2 \cdot \tilde{k}_x \left(\frac{\cos(\varphi)\tilde{k}_x}{i\omega - \sigma_x} + \frac{\sin(\varphi)\tilde{k}_y}{i\omega - \sigma_y} \right) \quad (6.18)$$

$$\sin(\varphi)(-i\omega + \sigma_y) = c^2 \cdot \tilde{k}_y \left(\frac{\cos(\varphi)\tilde{k}_x}{i\omega - \sigma_x} + \frac{\sin(\varphi)\tilde{k}_y}{i\omega - \sigma_y} \right) \quad (6.19)$$

The two equations Equation 6.18 and Equation 6.19, connects the two unknowns \tilde{k}_x and \tilde{k}_y [Berenger, 1994]. Taking the ratio of the two equations, yields:

$$\frac{\cos(\varphi)(i\omega - \sigma_x)}{\sin(\varphi)(i\omega - \sigma_y)} = \frac{\tilde{k}_x}{\tilde{k}_y} \quad (6.20)$$

Solving for the complex wave number \tilde{k}_y in Equation 6.20 and substituting the result into Equation 6.18 gives:

$$-\cos(\varphi)^2(i\omega - \sigma_x)^2 = c^2\tilde{k}_x^2 \quad (6.21)$$

where the positive solution for \tilde{k}_x gives

$$\tilde{k}_x = \frac{\cos(\varphi)(i\sigma_x + \omega)}{c} \quad (6.22)$$

Using the same approach for \tilde{k}_y , gives

$$\tilde{k}_y = \frac{\sin(\varphi)(i\sigma_y + \omega)}{c} \quad (6.23)$$

Substituting Equation 6.22 and Equation 6.23 into Equation 6.16 and Equation 6.17 gives:

$$\hat{p}_x = \frac{i\cos(\varphi)^2c(i\sigma_x + \omega)\rho_0v_0}{i\omega - \sigma_x} = \cos(\varphi)^2c\rho_0v_0 \quad (6.24)$$

$$\hat{p}_y = \frac{i\sin(\varphi)^2c(i\sigma_y + \omega)\rho_0v_0}{i\omega - \sigma_y} = \sin(\varphi)^2c\rho_0v_0 \quad (6.25)$$

Thus, the total pressure amplitude can now be found as:

$$\hat{p} = \hat{p}_x + \hat{p}_y = c\rho_0v_0(\cos(\varphi)^2 + \sin(\varphi)^2) = c\rho_0v_0 \quad (6.26)$$

which rearrange shows that the acoustic impedance experience by the incident wave is equal to the acoustic impedance from which the plane wave traveled from, by the pressure velocity relation [Pierce, 1989]:

$$z = \frac{p_0}{v_0} = c\rho_0 \quad (6.27)$$

This proof shows that a theoretical plane wave of any angle and any frequency is perfectly matched using a single PML layer. It can, however, be found that in practical numerical experiments, reflections may occur due to numerical artifacts. The numerical artifacts can, however, be reduced by tuning the damping factors [Berenger, 1994]. The PML method also works with waves other than plane waves with only a minimum of reflection [COMSOL, 2017b].

The PML implementation for the acoustic module in COMSOL has different geometry settings that automatically detects the local coordinate systems needed inside the PML domains. The geometry setting that fits the problem of this work is the cylindrical geometry setting. Other parameters like the damping factors are set to default.

PML Mesh

As the PML layers are actual domains, they have to be discretized in terms of mesh. The mesh in the PML layers is sensitive to coordinate scaling which may result in poor mesh qualities. Convergence problems for iterative solvers are likely to occur if poor mesh qualities exist in the PML domains. Hence, it is advantageous to use structured swept mesh in the direction normal to the direction of scaling as this minimizes the chance for low mesh qualities [COMSOL, 2017d]. In Figure 6.14, a cut view from the top of the simplified model can be seen together with annotations related to the PML mesh. The domain thickness of the PML is controlled as a proportion of the wavelength $L = \lambda_0/L_N$. The layer thickness is also controlled as a proportion of the wavelength $h = \lambda_0/h_N$.

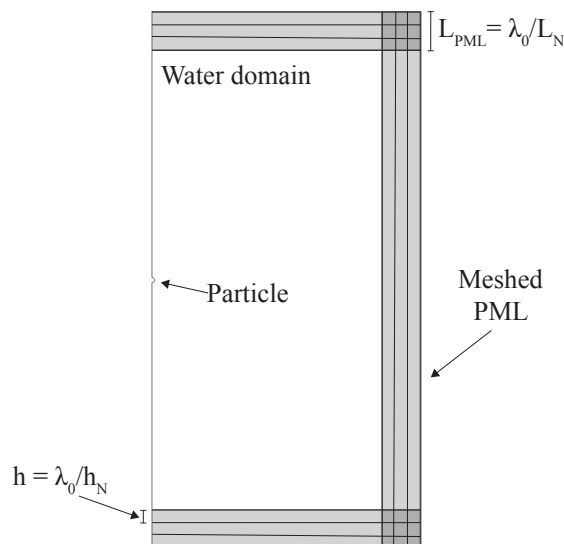


Figure 6.14. Cut view of the simplified model with PML annotations.

The nearest integer of the ratio of the PML domain thickness and the PML layer thickness, gives the number of layers in the PML domain. The number of layers is implemented in COMSOL using the distribution node under the swept mesh with a fixed number of elements by $n = \text{round}(L/h)$. Figure 6.15 show the scattered wave pressure level using different PML layer thickness h with a constant PML domain thickness of $L = \lambda_0/8$.

From Figure 6.15 to the left, it can clearly be seen that reflections from the boundaries affect the solution of the scattering pressure field. It can also be seen that a thinner PML layer thickness, thus increases the number of layers, reduces the reflections from the boundaries in the solution. Already from $h = \lambda_0/20$, it can be seen that the variation in

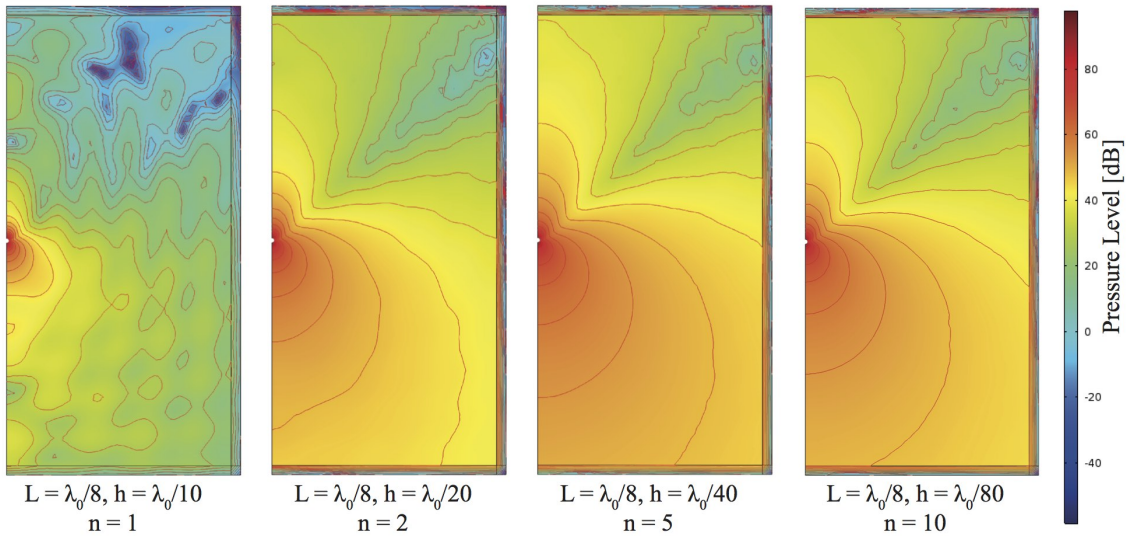


Figure 6.15. Acoustic scattering pressure sound level with different PML layer thicknesses. The frequency is $f_0 = 10\text{MHz}$, particle size $a = 5\mu\text{m}$ and the medium is water.

the solution settles as the layer thickness of the PML is decreased.

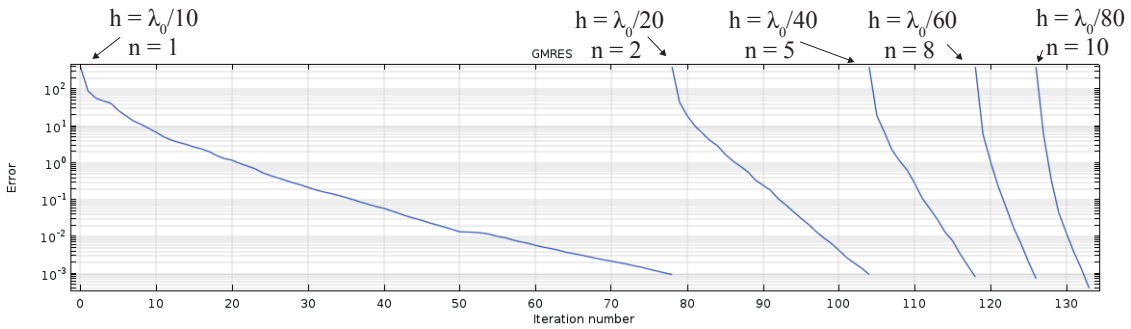


Figure 6.16. The convergence rate with different numbers of layers in the PML swept mesh ($L = \lambda_0/8$).

The PML settings does, however, also affect the numerical stability of the problem, which is evident in Figure 6.16 showing the number of iterations used by the iterative solver. The PML settings, therefore, both influences the precision of the solution and the stability of the problem. Using the approach of relating the numerical solution with the analytical solution as introduced in Section 6.2.1, the relative accumulated error is calculated for different values of L_N and h_N .

Figure 6.17 shows the relative accumulated error together with the total simulation time, the physical memory required and the problem size as a function of the number of layers in the PML domain. The results in Figure 6.17 shows that the principal parameter for the PML is the total number of layers used in the PML domain and that different PML domain thicknesses do not influence the solution significantly. From the total simulation time in Figure 6.17, it can be seen that simulation time has a U shape, with large simulation times

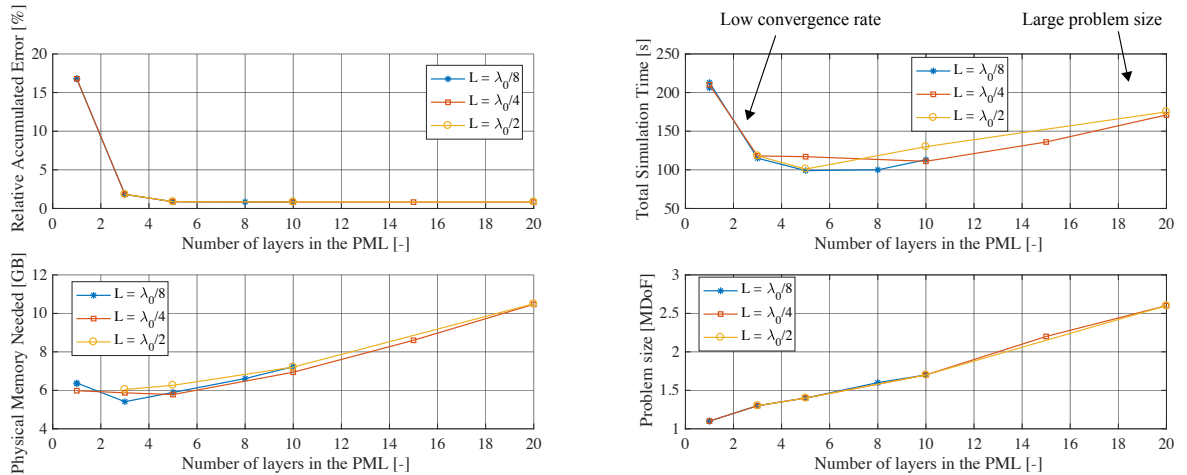


Figure 6.17. Relative accumulated error, total simulation time, the physical memory required and the problem size as a function of the number of layers in the PML domain n .

using only a few PML layers due to a low convergence rate and large simulation time using more than ten layers due to a larger problem size. Using the results from Figure 6.17, the number of PML layers is chosen to be approximately 8 layers.

6.2.3 Solver Selection for the Acoustic Calculation

In the Acoustic Module Users Guide [COMSOL, 2017b], a large range of direct and iterative solvers are suggested. Small acoustic problems (low number of DoF) are often solved using direct solvers like the MUMPS or PARADISO. But as seen in the maximum mesh element size relation $n_{max} = \frac{c}{f_0 N}$, high-frequency acoustic problems require small mesh elements which result in large problems requiring substantial memory resources when using direct solvers. Iterative solvers are, hence, often the only option when choosing solvers. The geometric multigrid as a solver is proposed in [COMSOL, 2017b] with various smoothers. Using geometric multigrid as the solver, require the Nyquist criterion to be satisfied in the entire geometry, otherwise, the solution may not converge [COMSOL, 2017b]. Especially edge and boundary nodes can be problematic regarding the Nyquist-criterion. Linear solvers like GMRES or FGMRES can, however, be used with the geometric multigrid as the preconditioner, even with elements not fulfilling the Nyquist criterion [COMSOL, 2017b].

Using the simplified model as shown in Figure 6.4, together with the mesh chosen in Section 6.2.1 and the PML settings found in Section 6.2.2, an investigation of different solver configuration is conducted. The problem is a Pressure Acoustic Frequency Domain Simulation, with the settings for the background pressure and materials as found in Section 6.2.1, giving a problem size of 1.59M DoF. The machine used has an Intel Xeon E5-2665 2.40 GHz CPU with 16 cores, 77.75 GB available memory and runs COMSOL 5.3 in Windows 7 (64bit).

Table 6.1 show the results of the investigation using different solvers and different solver set-ups.

Iterative Solvers		
Solver	Preconditioner	Results
Preconditioner	Geometric Multigrid (1 level) PARADISO as Coarse Solver	Maximum number of iterations reached (200 iter.)
Preconditioner	Geometric Multigrid (1 level) Krylov with GMRES as smoother PARADISO as Coarse Solver	6 Iter., Memory 14.38GB, Sim. time 51 min 39 sec
GMRES	Geometric Multigrid (1 level,V seq.) MUMPS as Coarse Solver	8 Iter., Memory 6.49 GB, Sim. time 90 sec
GMRES	Geometric Multigrid (1 level,V seq.) PARADISO as Coarse Solver	8 Iter., Memory 6.19 GB, Sim. time 75 sec
GMRES	Geometric Multigrid (1 level,W seq.) MUMPS as Coarse Solver	8 Iter., Memory 6.72 GB, Sim. time 90 sec
GMRES	Geometric Multigrid (1 level,F seq.) MUMPS as Coarse Solver	8 Iter., Memory 6.88 GB, Sim. time 92 sec
FGMRES	Geometric Multigrid (1 level) PARADISO as Coarse Solver	8 Iter., Memory 7.25 GB, Sim. time 86 sec
GMRES	Algebraic Multigrid PARADISO as Coarse Solver	>1000 Iter., Memory -GB, Sim. time >60 min
Direct Solvers (default solver in COMSOL)		
Solver	Preconditioner	Results
MUMPS	Solved directly	Memory 54.79GB, Sim. time 13 min 23 sec
PARADISO	Solved directly	Memory 45 GB, Sim. time 9 min 43 sec

Table 6.1. Comparison between different solvers and solver settings for an Acoustic Helmholtz problem with PML. Problem size 1.59M DoF.

From Table 6.1, it can be concluded that the GMRES linear solver with the Geometric Multigrid Preconditioner and PARADISO as the coarse solver, is the solver-setting that uses the lowest amount of memory and solves the problem at highest speed. This solver is, therefore, chosen for the final acoustic simulations.

6.3 Particle Distribution and Acoustic Geometry Generation

In the first part of the second stage, the particle positions are utilized in the particle geometry generation algorithm. The diagram in Figure 6.18 shows the first part of the second stage.

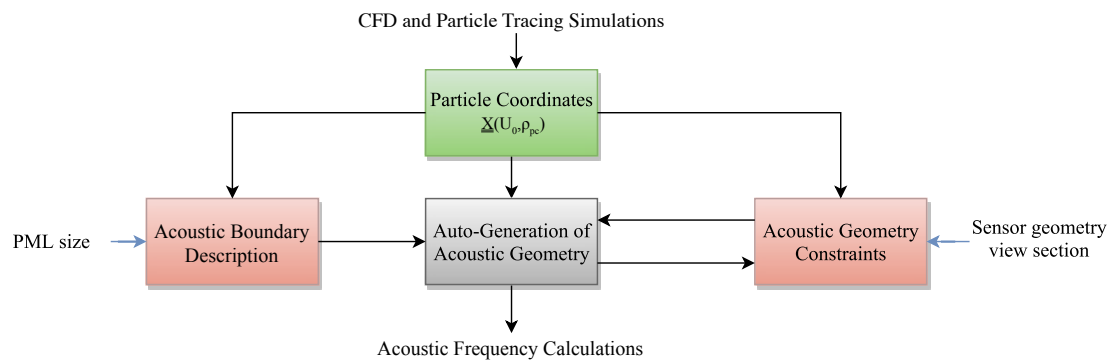


Figure 6.18. The first part of the second stage.

The particle coordinates are exported from the first stage of the modeling framework, which defines the size of the acoustic domain. The *Acoustic Boundary Description* box contains the algorithm that generates the outer domains of the system. The *Acoustic Geometry Constraints* box in Figure 6.18 holds constraints for the particle geometry generation algorithm and makes sure that no particles are placed within the PML domains and that particles on the boundaries are removed. The *Auto-Generation of Acoustic Geometry* box in Figure 6.18 then creates the particle geometry in an iterative manner from the particle coordinate matrix and combines the final acoustic geometry.

6.3.1 Acoustic Domain and Particle Coordinates

The geometry of the final model has the same shape as simplified model seen in Figure 6.4, thus a symmetrical cylinder with PML domains on the outer boundaries. The radius of the measurement tube is used as the radius of the cylinder in the final model. The available memory in the computer used for the acoustic simulations is the limiting factor for the size of the acoustic geometry, thus defines the length of the cylinder assuming constant radius.

When an ultrasonic wave propagates through a cloud of particles, produces each particle a scattered wave reinforcing the pressure field in some directions through multi-scattering. Assuming that the cloud of particles is of spherical form and that the particles are significantly smaller than the wavelength of the background wave. Also, assuming that the internal particle distances are less than a wavelength. Then the scattering of the particle cloud can be calculated using the scattering solution of a single particle as derived in Section 2.2, but with effective parameters such as effective radius, effective density, and

effective compressibility [Morse & Ingard, 1968]. It is, therefore, expected that the multi-scattering pressure primarily found some distance from the end of the cylindrical domain as shown in Figure 6.19. Using a too short cylinder domain as the computational domain and the multi-scattering effects are not captured.

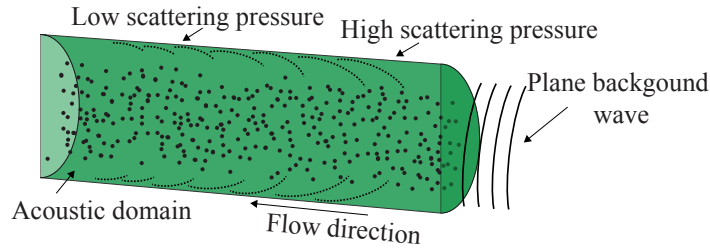


Figure 6.19. Non-uniform distribution of the particle scattering due to the angle influence in the scattering solution.

From preliminary numerical experiments, it has been found that a cylinder length of 10mm can be simulated with the 77GB of RAM available in this work, but only with a reduced background plane wave frequency of 2MHz. The reduced background frequency is treated later in Section 6.5.

Figure 6.20 shows the particle coordinates exported from the fluid flow and particle tracing simulation in stage one together with the particles selected for the acoustic geometry generation marked with orange.

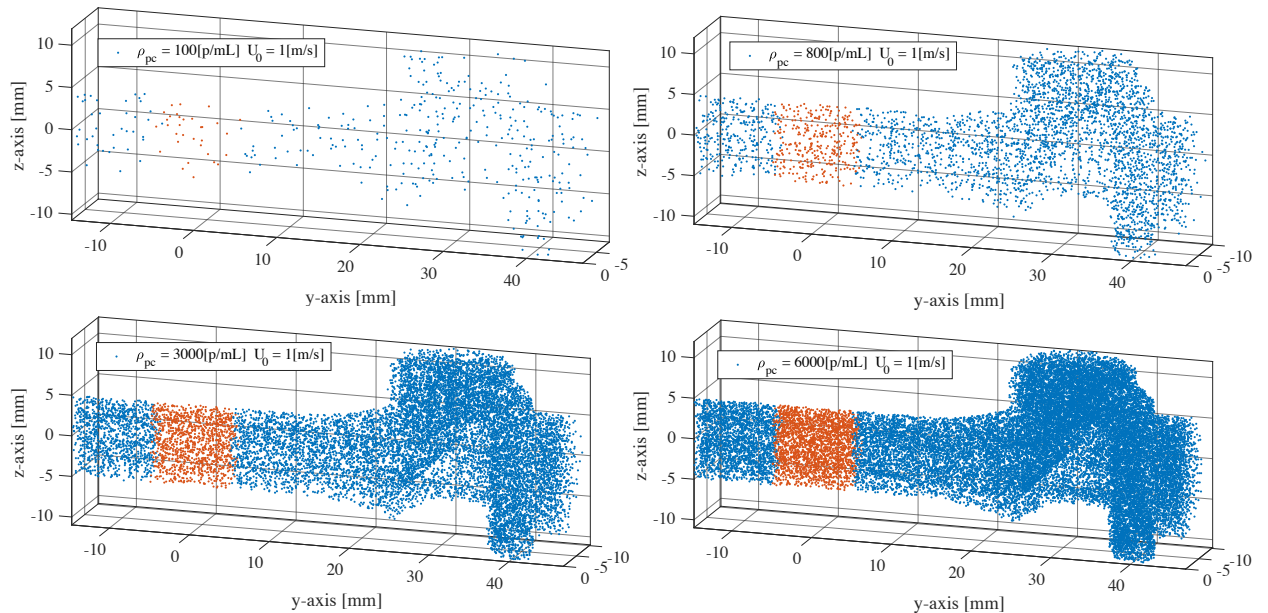


Figure 6.20. Particle coordinates exported from the fluid flow and particle tracing simulation, stage one. The orange particles are the particles selected for the acoustic geometry generation.

The particle selection is performed by searching through the particle coordinates and selecting only the particles $\pm 5mm$ from zero on the y -axis. Also, through preliminary numerical experiments, it has been found that inverted mesh problems occur if particles

are touching the symmetry surface. The particles with coordinates one particle diameter from the symmetry surface are, therefore, removed. However, this condition only affects a few particles, and the influence of the removed particles can be ignored. The Matlab script used to select the particles can be seen in Appendix F.1.

In Figure 6.21, a front view of the selected particles with different flow velocities and a constant particle concentration of $6000p/mL$, can be seen. The large difference particle distributions seen in Figure 6.21 is a consequence of the flow profiles seen in Figure 5.8.

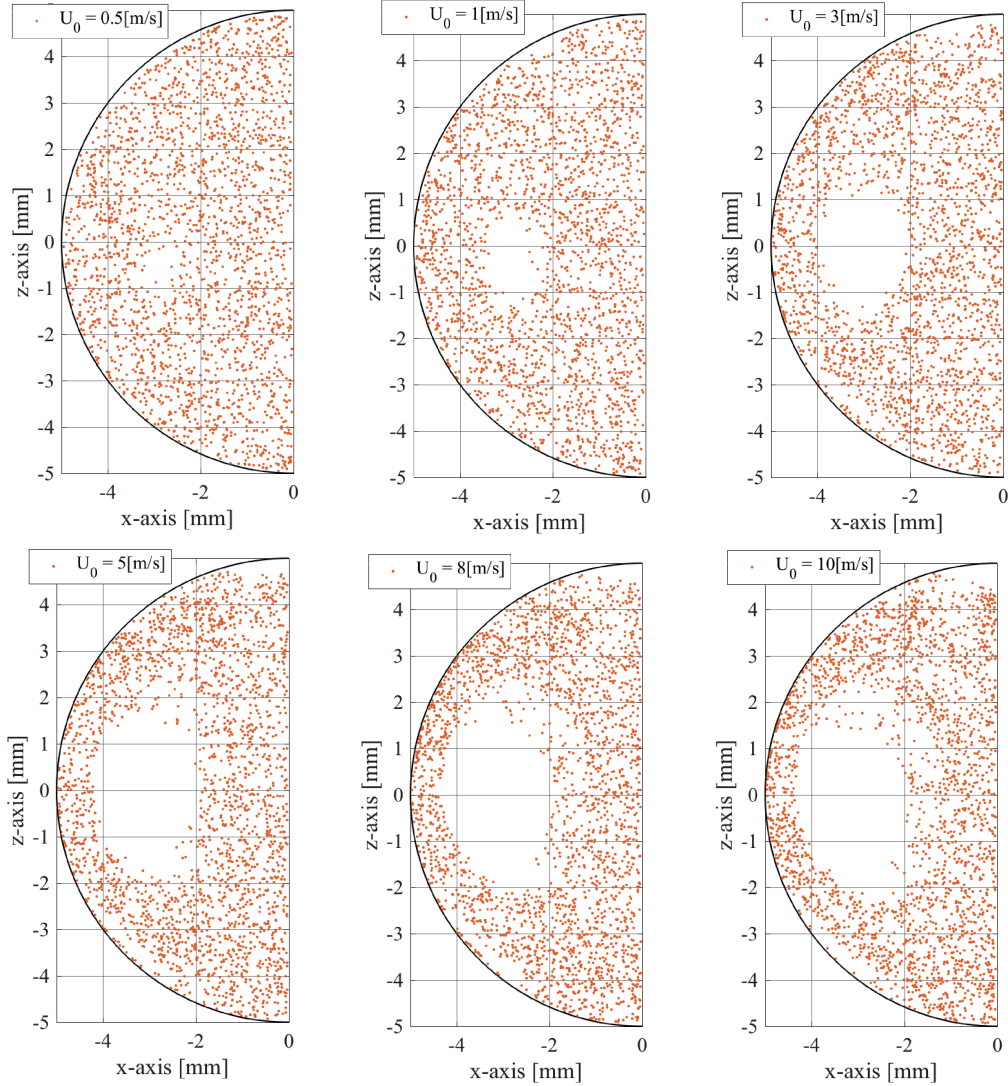


Figure 6.21. Cut-view of the particles selected for the acoustic geometry generation, with a constant particle concentration of $6000p/mL$ and different flow velocities.

The final acoustic geometry used for the acoustic simulations is created in two sequences. At first, a base geometry is defined without particles. The base geometry consists of a half cylinder with a radius of $R = 5mm + 0.2mm$, where the $0.2mm$ is an extra radius length ensuring that no particles encounter the outer boundaries. Particles on or adjacent to the

boundary may result in inverted meshes or failure in the automatic meshing algorithm. The length of the cylinder is chosen to be $H = 10\text{mm} + 2 \cdot 0.2\text{mm}$. The PML domain thickness is chosen to be $L = \lambda_0/4$.

The last part of the sequence is to create the particle geometry using Matlab LiveLink for COMSOL. The particle geometry is created by sweeping through all selected particles seen as the orange particles in Figure 6.20 and creating a spherical geometry with radius a at the, of each particle, associated coordinate sets. The particle geometry is then saved as a *.mphbin* file which can be imported into COMSOL. The acoustic particle geometry generation algorithm can be found in Appendix F.2.

The final acoustic geometry is then created by importing the particle geometry into the base geometry. Assuming rigid particles, the boolean operator "difference" is used to subtract the computational domain from the particle geometry. Using the difference operator permit the computational domain to be constructed without the internal domains of each particle, which for the rigid case is not need for the calculation of the scattering field, thus reduces the computational size. For non-rigid particles, the "difference" operator is disabled, allowing the material parameters to be assigned to the particles. An example of the final geometry with $5000p/mL$ at 0.5m/s can be seen in Figure 6.22.

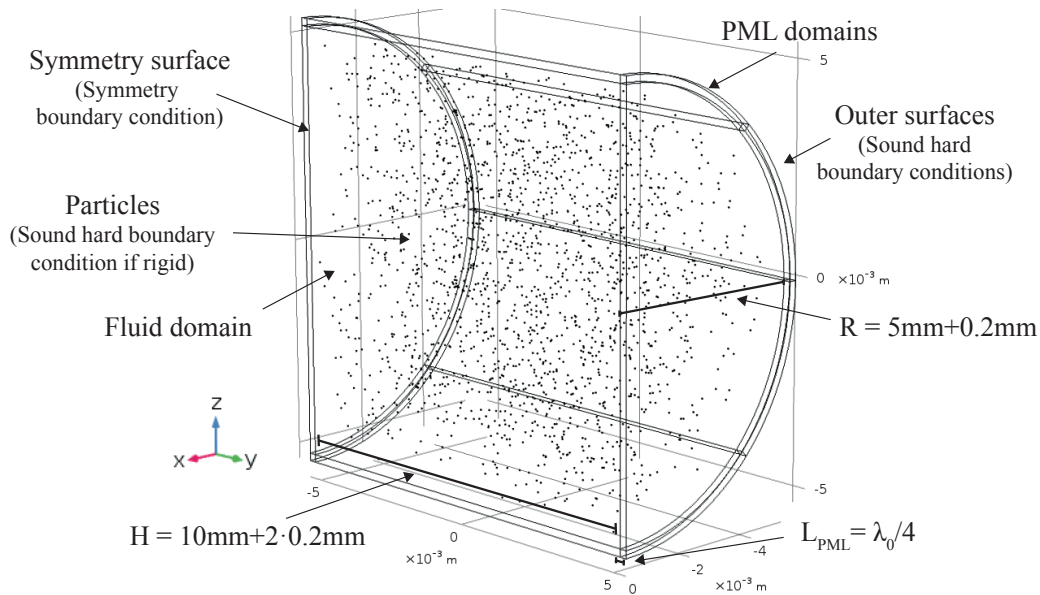


Figure 6.22. Final acoustic geometry using a particle geometry with with $5000p/mL$ at 0.5m/s .

The boundary conditions applied to the final model can also be seen in Figure 6.22. At the outer surfaces, a sound hard boundary condition is applied meaning that the normal velocity is zero. If rigid particles are assumed, the surface of the particles is also assigned with a sound hard boundary condition.

The geometric entities like surfaces, domains, edges, and points is assigned by COMSOL a unique number that is used to define to what entity a specific boundary condition or model

feature should apply. Since the surfaces and domains of each particle are assigned unique numbers, all the unique numbers changes when importing different particle geometries. An automation of the selection of the geometric entities is therefore needed. In COMSOL a large variety of selection tools based on geometric features can be found. A "selection box" is used to select the fluid domain, a "complement selection" is used to select the PML domains, a "selection cylinder" is used to select the particle boundaries or domains (depending on rigid or non-rigid particles), a "selection box" is used to select the symmetry boundary, and a "difference selection" is used to select the internal boundaries between the fluid domain and the PML domains.

6.4 Mesh in the Final Model

The final model mesh is made similar to the mesh for the simplified model (see Section 6.2.1). The fluid domain is discretized using a free tetrahedral mesh with maximum element size $n_{\max} = \frac{c}{N \cdot f_0}$, a minimum element size $n_{\min} = \frac{a}{N}$, a maximum growth rate of 1.5, a curve factor of 1 and resolution in narrow regions of 1. The PML domains are meshed using swept mesh with a layer thickness of $h = \lambda_0/30$, which gives 7 PML layers, using a PML thickness of $L = \lambda_0/4$. A boundary layer mesh is applied to the internal surface between the fluid domain and the PML domains, which increases the precision of the normal gradient of the pressure at the boundary [COMSOL, 2017b].

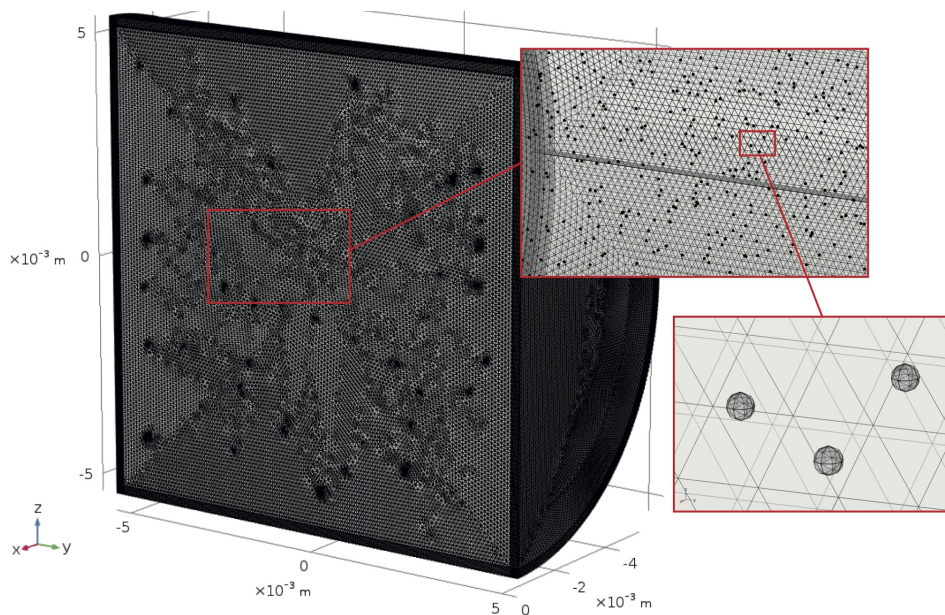


Figure 6.23. Final mesh using the final geometry seen in Figure 6.22. The background wave frequency is 2MHz.

Figure 6.22 shows the mesh using a 2MHz background wave. The meshing algorithm took 5min and 15sec to generate the mesh consisting of 13.1M elements which result in a problem size of 19.5M DoF.

6.5 Scaled Scatter Solution

The simulation conditions found in the Problem Statement (see Chapter 3) states that the simulation should be conducted using a background frequency of 10MHz. It can, however, be found that the resulting mesh is too large to be built and consists of more than 100M elements. The frequency is, therefore, reduced to 2MHz as described in Section 6.4.

In Section 2.2.2, the far-field approximation was derived, which in short can be written as:

$$p_{sc} = \frac{e^{ik_2 r}}{r} k_2^2 a^3 A(\theta) \quad (6.28)$$

where $A(\theta)$ is an amplitude function and $k_2 = \frac{\omega}{c_2}$ is the fluid domain wave number.

The wave number and particle radius relation can be rewritten as:

$$k_2^2 a^3 = \left(\frac{k_2}{q}\right)^2 (a \cdot v)^3 \implies v = q^{2/3} \quad (6.29)$$

where v and q are positive constants.

Inserting the relation seen in Equation 6.29 into the far-field approximation in Equation 6.28, yields the scaled far-field solution:

$$p_{sc,s} = \frac{e^{ik_2 r}}{r} \left(\frac{k_2}{q}\right)^2 (a \cdot q^{2/3})^3 A(\theta) \quad (6.30)$$

Since the frequency is reduced from 10MHz to 2MHz, the scaling factor q is equal $q = \frac{10MHz}{2MHz} = 5$ and the particle size should, therefore, be scaled by the factor $5^{2/3} = 2.92$. Inserting the scaled particle with radius $a_s = a \cdot q^{2/3}$ and a frequency of 2MHz into the scattering solution found in Section 2.2, together with the solution of the non-scaled particle and frequency the two solutions can be related. In Figure 6.24, both the scaled backscattering ($\theta = 180deg$) solution and the non-scaled backscattering solution can be seen as a function of radius normalized with the scaled particle diameter $d_s = 2 \cdot a_s$. In Figure 6.24 it is assumed that the particle is rigid with an original size of $a = 5\mu m$, a non scaled frequency of 10 MHz and an incident wave amplitude of $1MPa$, in both cases.

The RMS pressure of both the scaled and non-scaled solution can also be seen in Figure 6.24. The RMS pressure for time-harmonic waves is equal to the time-average pressure and can be used to describe the effective pressure of the wave. Two waves with different wave frequencies can, therefore, easily be related as shown in Figure 6.24. The RMS pressure is calculated as:

$$p_{rms}^2 = \frac{1}{T} \int_0^T p_d^2 dt \quad (6.31)$$

where $T = \frac{1}{f} = \frac{2\pi}{\omega}$ is the time interval. Assuming that the pressure is described by the time-harmonic disturbance $p_d = \text{Re}\{p e^{-i\omega t}\} = \text{Re}\{p_0 e^{ik} e^{-i\omega t}\}$, then the RMS pressure can be found as:

$$p_{rms}^2 = \frac{1}{2} p_0^2 = \frac{1}{2} |p|^2 \implies p_{rms} = \sqrt{\frac{1}{2} |p|^2} = \sqrt{\frac{1}{2} p^* p} \quad (6.32)$$

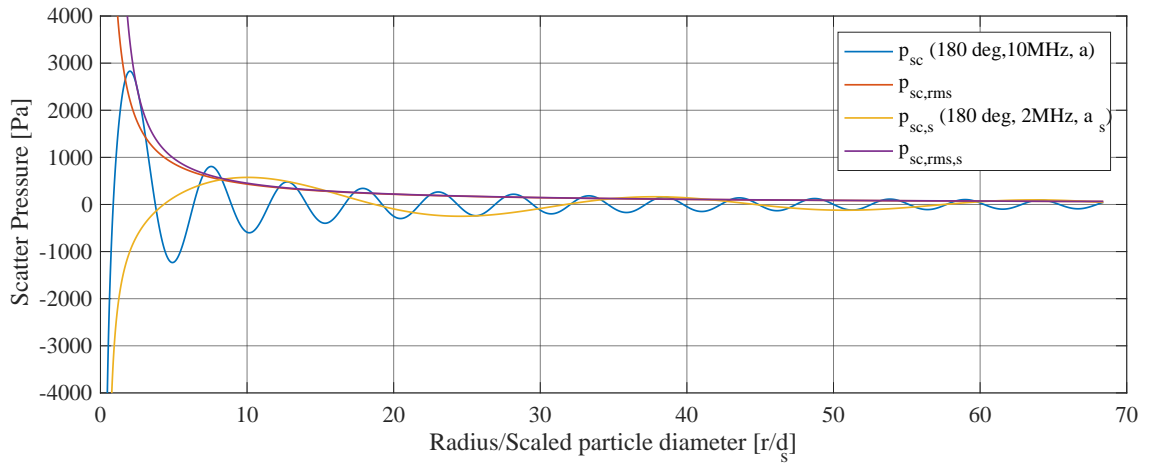


Figure 6.24. The scaled backscattering ($\theta = 180deg$) solution with $a_s = a \cdot 5^{2/3}$ and associated non-scaled solution, together with the RMS pressures of the two waves as a function of the radius normalized with the scaled diameter $d_s = 2 \cdot a_s$. The incident wave has an amplitude of $1MPa$ and the particle is assumed rigid.

where p^* is the complex conjugated of the pressure p .

In Figure 6.25 and Figure 6.26, the absolute error and the relative error¹ in four different directions can be seen respectfully as a function of the normalized radius. From Figure 6.26,

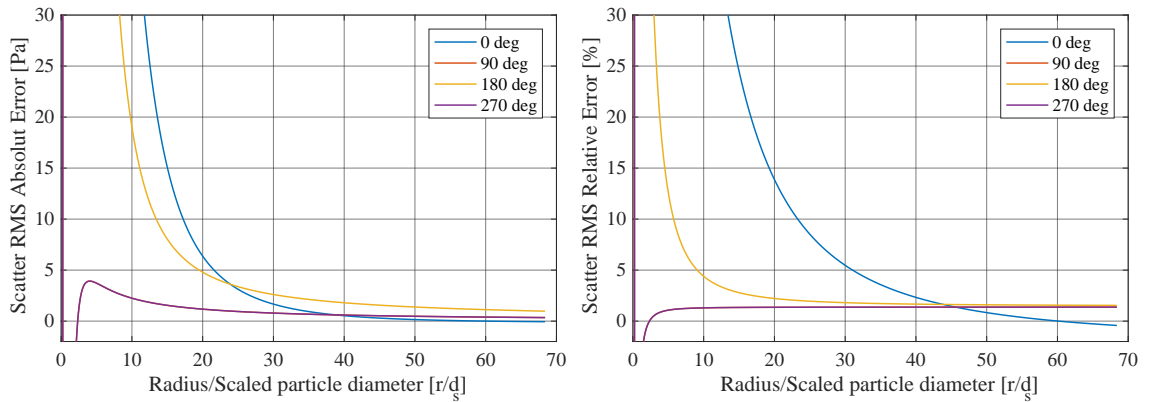


Figure 6.25. Absolute error between the scaled and non-scaled scatter solution in four directions.

Figure 6.26. Relative error between the scaled and non-scaled scatter solution in four directions.

it can be seen that the relative error is large close to the particle and for the backscattering (180deg), the error decreases under 5% after ten times the scaled particle diameter (d_s) and settles to an error of approximately 2.5 % error after 20 times d_s . It can also be seen that the 90deg and 270deg scattering error is small already from 5 times d_s and that the forward scattering (0deg) decreases under 5% after 32 d_s .

¹The relative error is calculated as $p_{\text{error}} = \frac{p_{\text{sc}} - p_{\text{sc},s}}{p_{\text{sc}}} \cdot 100[\%]$

From Figure 6.25 and Figure 6.26, it can be seen that the scaling of the particle size to achieve the same effective pressure at a lower frequency, is only, to some extent, valid if the particles are far from each other.

Note that in Appendix F.3, the scripts used in the following analysis can be found. Using the particle coordinates found in Section 5.3, the distance between all particles can be calculated. The distance between two particles $q_i^{(x,y,z)}$ and $q_j^{(x,y,z)}$ can be found using the Euclidean distance:

$$d_{ij} = \sqrt{(q_i^x - q_j^x)^2 + (q_i^y - q_j^y)^2 + (q_i^z - q_j^z)^2} \quad (6.33)$$

Sweeping through all the particles for a given flow and particle tracing solution (the solution set), the following particle distance matrix can be found:

$$\mathbf{D} = \begin{bmatrix} 0 & d_{12} & d_{13} & \dots & d_{1j} \\ d_{21} & 0 & d_{23} & \dots & d_{2j} \\ d_{31} & d_{32} & 0 & \dots & d_{3j} \\ \vdots & \vdots & \vdots & \ddots & \vdots \\ d_{i1} & d_{i2} & d_{i3} & \dots & 0 \end{bmatrix} \quad (6.34)$$

where $i = j = N_{\text{particles}}$ and $N_{\text{particles}}$ is the total number of particles in the given solution set. The matrix in Equation 6.34 is clearly symmetric since the distance $d_{i,j}$ is equal to the distance $d_{j,i}$ and only half of the distances seen in Equation 6.34 needs to be calculated. In the following, Figure 6.27 is used as an example for the analysis of the particle distances and it is assumed that the particles has an radius of $a = 5\mu\text{m}$.

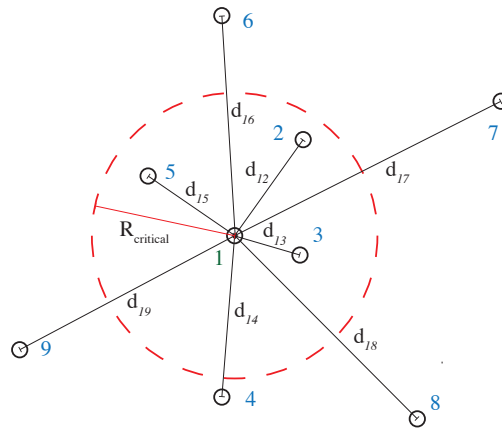


Figure 6.27. Particle cloud taking basis in the particle number 1 in the center used for the explanations in this section.

Further, it is assumed that a unit diagonal matrix of the size $N_{\text{particles}} \times N_{\text{particles}}$ is added to the matrix in Equation 6.34 and it is assumed that the distance between the particles is less than 1m . Taking basis in the system in Figure 6.27, the distances vector for the first particle $\mathbf{d}_{i=1,j=1..9}$ can be described as

$$\mathbf{d}_{i=1,j=1..9} = [1 \ d_{12} \ d_{13} \ d_{14} \ d_{15} \ d_{16} \ d_{17} \ d_{18} \ d_{19}] \quad (6.35)$$

Taking the minimum of the vector $\mathbf{d}_{i=1,j=1..9}$, gives the distance to the nearest particle.

$$d_{\text{next},i=1} = \min(\mathbf{d}_{i=1,j=1..9}) = d_{13} \quad (6.36)$$

Doing the same for all particles ($i = 1..N_{\text{particles}}$) and taking the mean of the resulting vector \mathbf{d}_{next} , gives the mean distance to the nearest particle for the given solution set. Figure 6.28 shows a contour plot of the mean distance to the nearest particle d_{next} normalized with the particle diameter d_s for different particle concentrations and different flows. Taking only the nearest particle may, however, give an inaccurate picture of the mean distance to the nearest particles. Instead, taking the mean of the distances of the nearest four particles may give a better picture. The mean of the distances between the nearest four particles in the system seen Figure 6.27 can be found as:

$$d_{\text{next4},i=1} = \text{mean}(\mathbf{d}_{i=1,j=1..9}^{\text{sorted}}(1:4)) \quad \text{where} \quad \mathbf{d}_{i=1,j=1..9}^{\text{sorted}} = \text{sort}(\mathbf{d}_{i=1,j=1..9}) \quad (6.37)$$

$$= \text{mean}([d_{13} \ d_{15} \ d_{12} \ d_{14}]) \quad (6.38)$$

where *sort* is a descending order sort function. Repeating this for all particles and taking the mean of the resulting vector, gives the mean of the particles mean distance of the nearest four particles $d_{\text{next4}} = \text{mean}(\mathbf{d}_{\text{next4}})$, for the given solution set. Where it is assumed that at least five particles can be found in the solution set. The mean of the mean distance to the nearest four particles d_{next4} normalized with the scaled particle diameter d_{next4}/d_s with different particle concentrations and different flows can be seen in Figure 6.29.

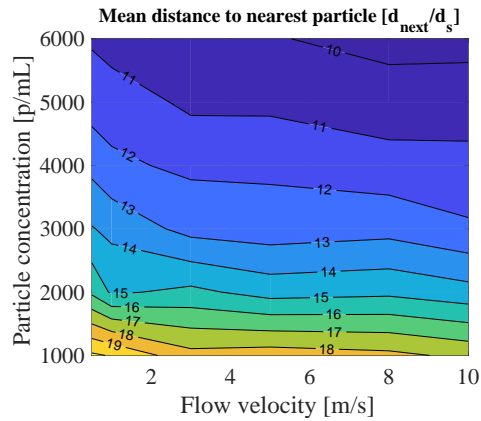


Figure 6.28. The normalized mean distance to the nearest particle, with different particle concentrations flow velocities.

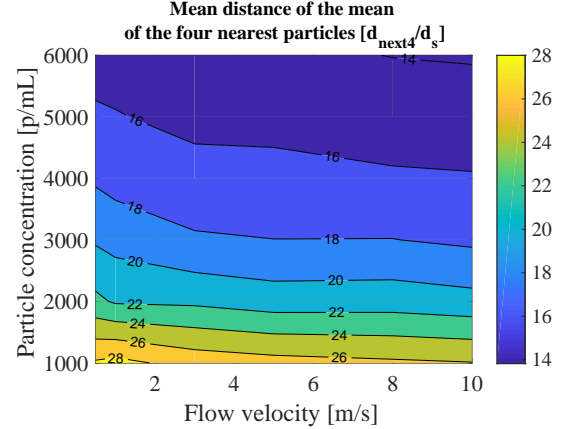


Figure 6.29. The normalized mean distance of the mean of the nearest four particles, with different particle concentrations flow velocities.

From Figure 6.28 and Figure 6.29, it can be seen that the mean distance of the nearest particle or the mean of the mean of the nearest four particles are in the worst case $10 \cdot d_s$ and $14 \cdot d_s$, thus the particle-particle interaction distance for the nearest four particles is at most $14 \cdot d_s$. Relating the results to Figure 6.26, shows that the nearest four particle-particle interactions contributes with a scaling error in the backscattering direction of 4% to 3%.

The number of nearest particles may, however, vary depending on the region of interest and the solution set. Referring to the system seen in Figure 6.27, a critical radius R_{critical} has been defined. The particles within the critical radius R_{critical} can be calculated using the boolean operator $<$ as:

$$N_{\text{critical},i} = \text{sum}(\mathbf{d}_{i=1,j=1..9} < R_{\text{critical}}) \quad (6.39)$$

$$= \text{sum}([0 \ 1 \ 1 \ 0 \ 1 \ 0 \ 0 \ 0 \ 0]) = 3 \quad (6.40)$$

The mean of the number of nearest particles over all particles ($\text{mean}(\mathbf{N}_{\text{critical}})$) within the critical distances $R_{\text{critical}} = 10 \cdot d_s$ and $R_{\text{critical}} = 20 \cdot d_s$ can be seen in Figure 6.30 and Figure 6.31 respectively, for different particle concentrations and flow velocities.

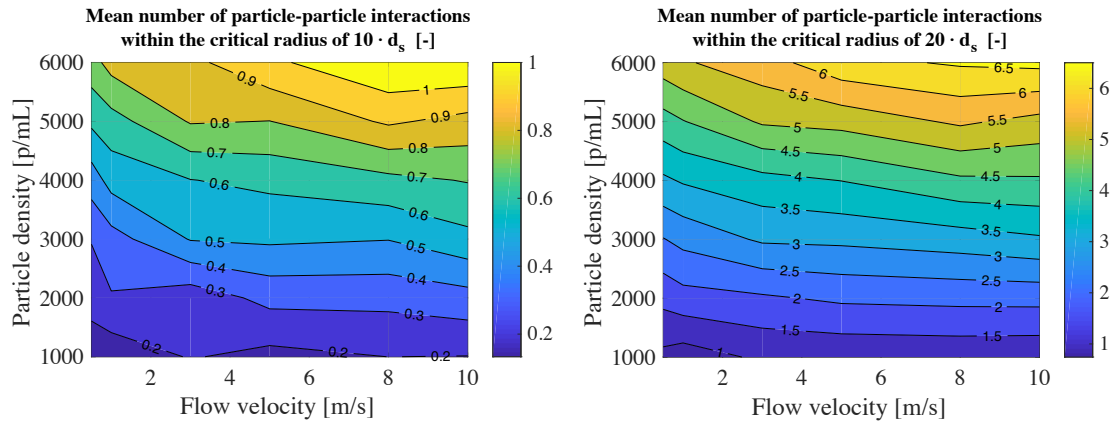


Figure 6.30. The mean of the number of particle-particle interactions over all particles with $R_{\text{critical}} = 10 \cdot d_s$ for different particle concentrations and flow velocities.

Figure 6.31. The mean of the number of particle-particle interactions over all particles with $R_{\text{critical}} = 20 \cdot d_s$ for different particle concentrations and flow velocities.

Figure 6.30 and Figure 6.31 shows that there is at maximum one particle-particle interaction within a critical region of $R_{\text{critical}} = 10 \cdot d_s$, from each particle and that there is multiple particle-particle interactions if the critical region is extended to $R_{\text{critical}} = 20 \cdot d_s$, from each particle.

Taking the sum $\mathbf{N}_{\text{critical}}$ vector gives the total number of particle-particle interactions N_{critical} within the R_{critical} distance, for the given solution set. The possible number of particle-particle interactions for a given solution set can be found as:

$$N_{\text{possible}} = N_{\text{particles}}^2 - N_{\text{particles}} \quad (6.41)$$

Dividing the total number of particle-particle interactions N_{critical} within R_{critical} with the total possible interactions N_{possible} times 100 gives the percentage of possible particle-particle interactions. The percentage of possible particle-particle interactions can be seen in Figure 6.32 and Figure 6.33 for $R_{\text{critical}} = 10 \cdot d_s$ and $R_{\text{critical}} = 20 \cdot d_s$, respectively.

In Figure 6.30, it was found that the worst case mean number of particles-particle interactions within a critical radius of $10 \cdot d_s$ was one particle-particle interaction. In Figure

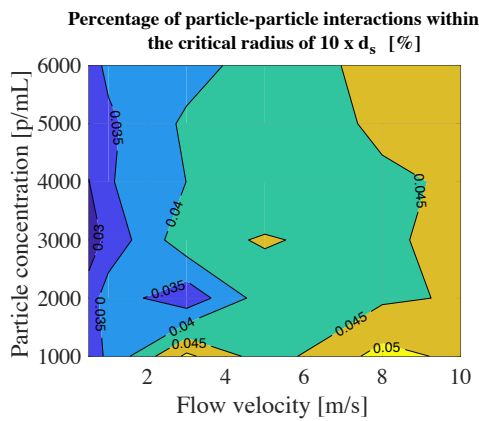


Figure 6.32. The percentage of possible particle-particle interactions for the critical radius of $R_{\text{critical}} = 10 \cdot d_s$.

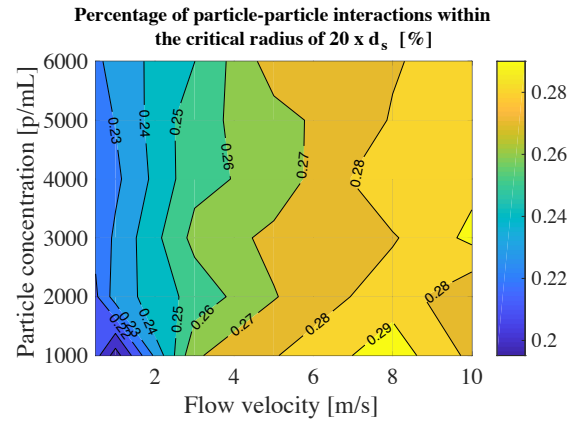


Figure 6.33. The percentage of possible particle-particle interactions for the critical radius of $R_{\text{critical}} = 20 \cdot d_s$.

6.28, it was found that nearest particle distance is a worst case $10 \cdot d_s$. It can, therefore, be concluded that the scaling error related to particle-particle interactions under $10 \cdot d_s$ results in a scaling error of at most 5% for the backscattering (see Figure 6.26). In Figure 6.31, it was found that the mean number of particles-particle interactions within a critical radius of $20 \cdot d_s$ was at worst 6.5 and best less than 1, depending on the solution set. It is difficult to conclude how the larger number of particle-particle interactions affects the scaling error. Figure 6.29, does, however, give a picture of how four particles affect the error through the mean distance of the four particles which at worst is $14 \cdot d_s$, thus resulting in a scaling error of at most 3% for the backscattering. Figure 6.32 and Figure 6.33 shows that the percentage of particle-particle interactions within the critical radius of $10 \cdot d_s$ and critical radius of $20 \cdot d_s$ compared to the total possible number of particle-particle interactions which is in general low.

For the given solution sets and with rigid particles, scaling the frequency and particle size are, hence, assumed to be a good approximation for the non-scaled solution.

THE COMBINED SIMULATION

In this chapter, the combined model constituting the model framework presented in Chapter 4 is presented together with the results of different sweeps using rigid and non-rigid particles and particles with different sizes. The combined model is implemented in Matlab using COMSOL LiveLink for Matlab. In Figure 7.1, the computational routines for the combined model can be seen.

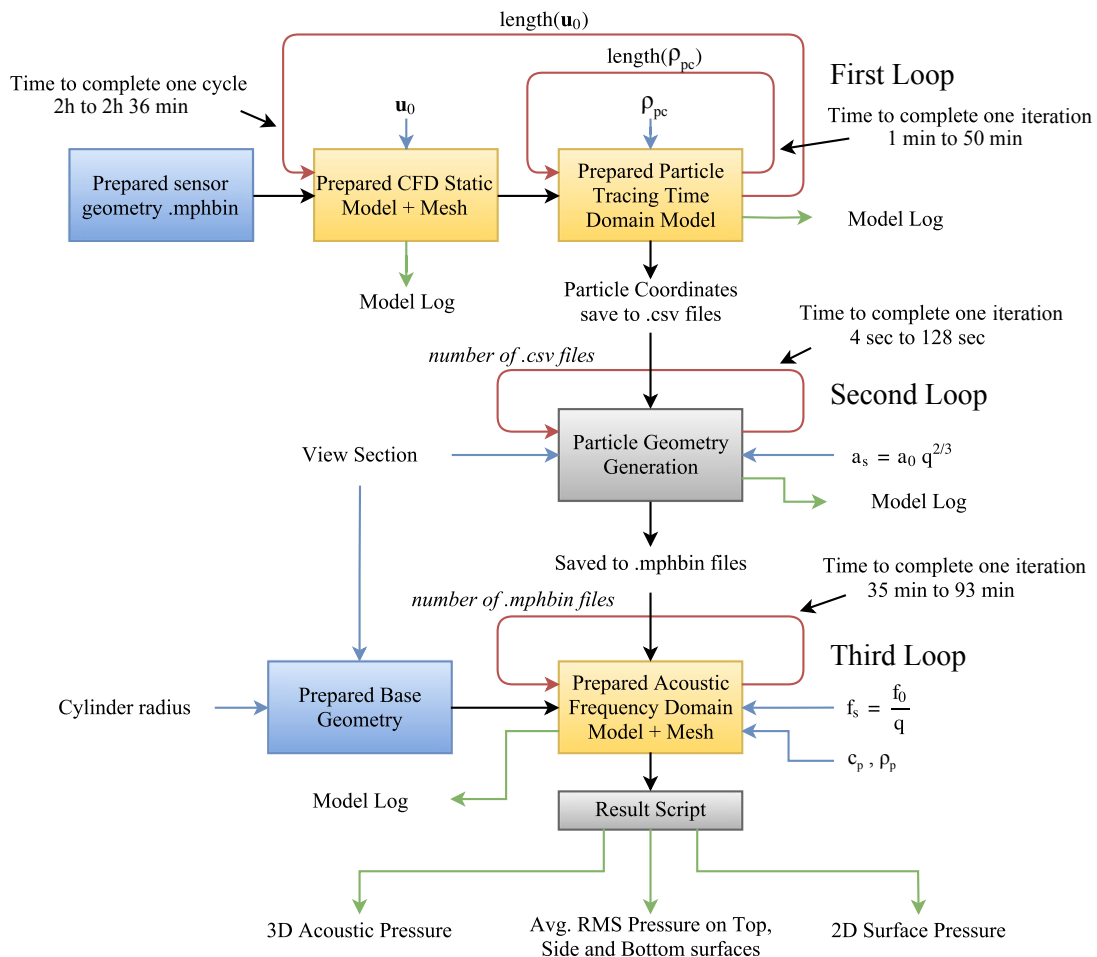


Figure 7.1. Diagram of the computational routines implemented in Matlab using COMSOL LiveLink for Matlab. The computational simulation times are examples from Section 7.1 and varies depending on the input and the computational power available.

Examining the diagram in Figure 7.1, it can be seen that the combined model is divided into three main loops. The first loop contains the static CFD simulation and particle tracing simulation. Beside the prepared sensor geometry as presented in Section 5.1, the flow velocity vector \mathbf{u}_0 and the particle concentration vector ρ_{pc} are inputs for the first loop. The number of iterations is defined by the length of the flow velocity vector and the particle concentration vector. After the first iteration of the outer loop, the solution of the static CFD is used multiple times to simulate the particle trajectories. This cascaded approach reduces the computational time significantly compared to a sequential approach. After particle concentration convergence (see Section 5.3), the particle coordinates is then exported to a .csv file. The first loop is then repeated until all flow velocities, and particle concentrations have been simulated. In the second loop, as seen in the diagram in Figure 7.1, the particle coordinate files are then used to construct the particle geometry that is utilized in the acoustic simulations. At each iteration of the second loop, the particle coordinates of a specific combination of flow velocity u_0 and particle concentration ρ_{pc} , together with a chosen particle size, is used to generate the particle geometry. After each iteration is the particle geometry saved in the COMSOL geometry format .mphbin. The second loop is repeated for all combinations of flow velocities and particle concentrations. The third loop consists of the acoustic meshing sequence and frequency domain simulation. The particle geometries are first loaded into the base geometry (see Section 6.3.1), then the acoustic mesh is created using the settings found in Section 6.2.1. After meshing, the acoustic scattering field is calculated, and critical properties are then exported into .mat and .fig files for later analysis and visualization. As for the second loop, this process is repeated for all flow velocities and particle concentrations. The three step method presented in the diagram in Figure 7.1 has the advantage of both allowing the entire modeling framework to be simulated without user interference, but also re-simulations of later loops to be conducted without needing the first loops to be re-simulated. An example could be that the user wants to find out how the particle size scales the RMS pressure at the surface of the sensor and the first loop has already been calculated. Then the user skips the first loop and creates another loop around the second and third loop sweeping through different particle sizes.

A few of such sweeps has been conducted which is presented in the following.

7.1 Results from The Combined Simulation

In the combined CFD and particle tracing simulation (loop one in Figure 7.1), the following inlet flow velocity vector \mathbf{u}_0 and particle concentration vector ρ_{pc} used:

$$\mathbf{u}_0 = [0.5 \ 1 \ 3 \ 5 \ 8 \ 10] \left[\frac{m}{s} \right] \quad (7.1)$$

$$\rho_{pc} = [10 \ 100 \ 300 \ 500 \ 800 \ 1000 \ 2000 \ 3000 \ 4000 \ 5000 \ 6000] \left[\frac{p}{mL} \right] \quad (7.2)$$

The inlet flow velocity vector, and particle concentration vector in Equation 7.1 and Equation 7.2 are utilized in all sweeps within this section. The results from the CFD simulations and particle tracing simulations have already been shown in Section 5.2.6 and Section 5.3.2 respectfully, and the results of these simulations are, therefore, not re-shown in this section. In the following, it is assumed that the speed of sound in the fluid medium is $1500m/s$, the density of the fluid medium is $1000kg/m^3$ and that the background plane wave has an amplitude of $1MPa$. The scaling approximation presented in Section 6.5 is also applied to all simulations, thus with a scaled background frequency of $2MHz$, and a scaled particle size as $a_s = a \cdot q^{2/3}$, where $q = 10MHz/2MHz = 5$.

Rigid particle and $a = 5\mu m$

In this sweep, it is assumed that the particle is rigid and has a size of $a = 5\mu m$. Figure 7.2 shows the total simulation time for the acoustic simulation including the meshing sequence. In Figure 7.3 the acoustic problem size can be seen as a function of the particle concentration for different flow velocities. Figure 7.3 shows that the problem size is directly proportional to the particle concentration and that the flow velocity influence is small mainly due to the small change in the total number of particles.

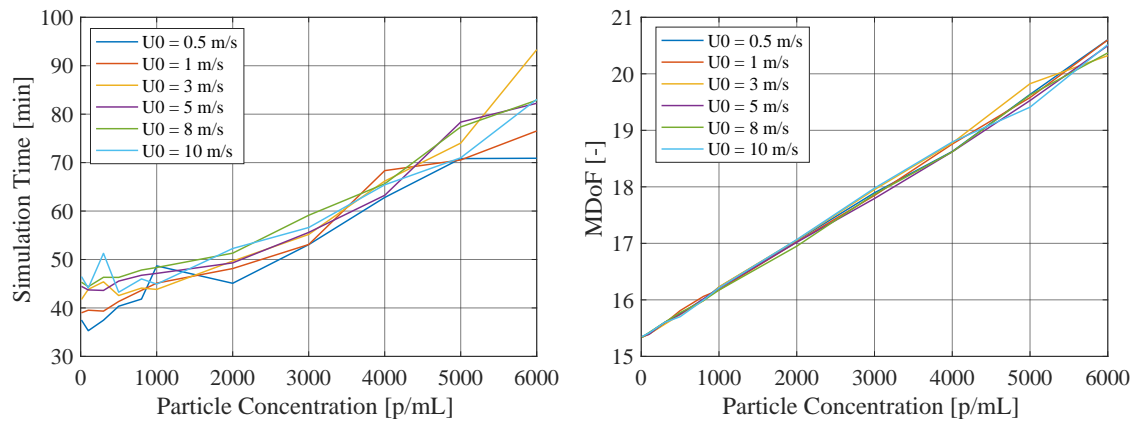


Figure 7.2. Total acoustic simulation time including the meshing sequence as a function of the particle concentration for different inlet flow velocities. **Figure 7.3.** Acoustic problem size (DoF) as a function of the particle concentration for different inlet flow velocities.

In Figure 7.4 four different 3D mirrored acoustic solution-sets can be seen together with

the associated RMS pressure scattering field on the outer fluid domain surfaces for different particle concentrations and with an inlet flow velocity of $1m/s$.

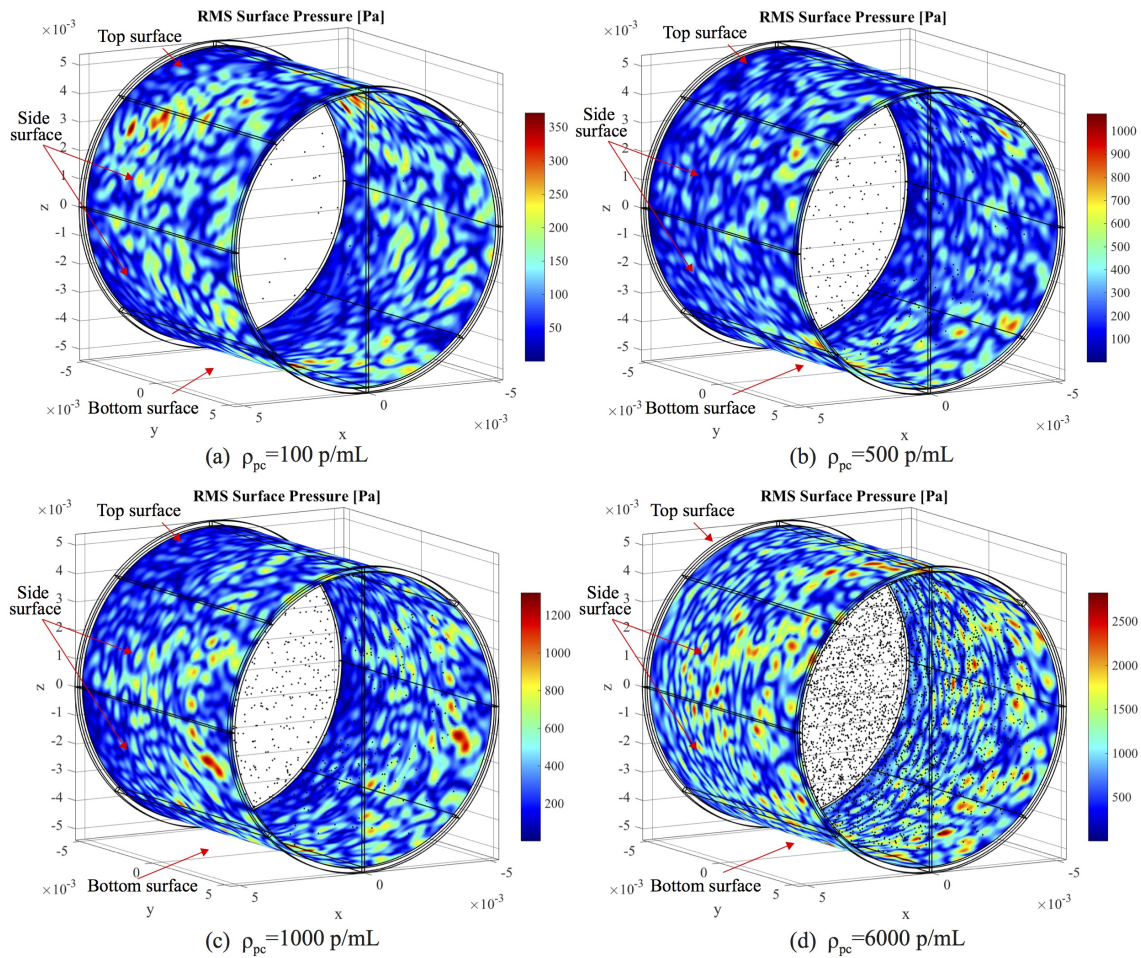


Figure 7.4. 3D mirrored acoustic solution-set with the RMS scattering pressure field on the outer fluid domain surfaces. The particle concentrations range from $100p/mL$ to $6000p/mL$, and an inlet flow velocity of $1m/s$. The particles are assumed rigid and with a particle size of $a = 5\mu m$.

The average of the RMS pressure on the top, side and bottom surfaces in the acoustic solution-sets makes it easier to relate different solution-sets to each other. The average surface RMS pressure can also be related directly to the RMS pressure the piezoelectric transducer would experience if placed on the surface.

Figure 7.5 shows the average RMS scattering pressure on the top surface (see Figure 7.4) as a function of the particle concentration with different flow velocities. Figure 7.6 shows the corresponding average RMS scattering pressure on the side and bottom surfaces respectfully.

Figure 7.7 shows the mean and standard deviations of the average RMS scattering pressure on the top, side and bottom. The mean and standard deviation is taken over the flow velocities, thus indicating the expected perturbation the flow gives to the average RMS acoustic pressure on the surface of the geometry.

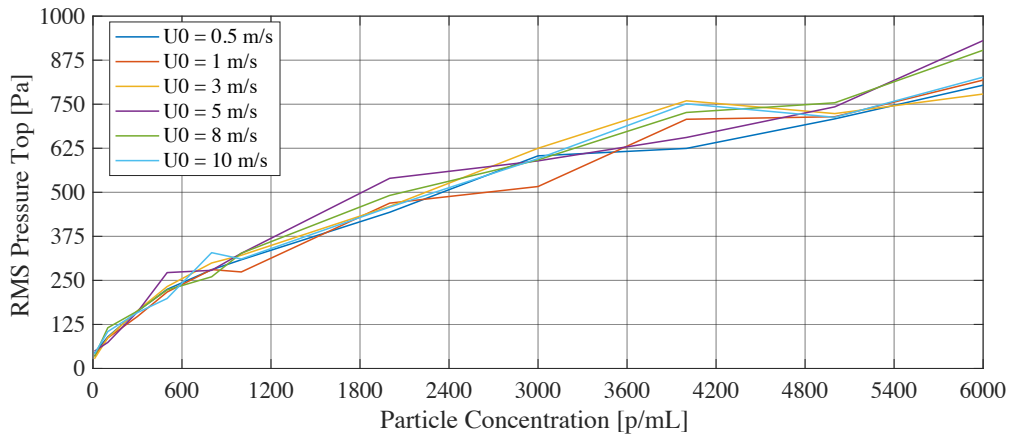


Figure 7.5. The average RMS pressure on the top surface as a function of the particle concentration and with different flow velocities. The particles is assumed rigid and with the size $a = 5\mu m$.

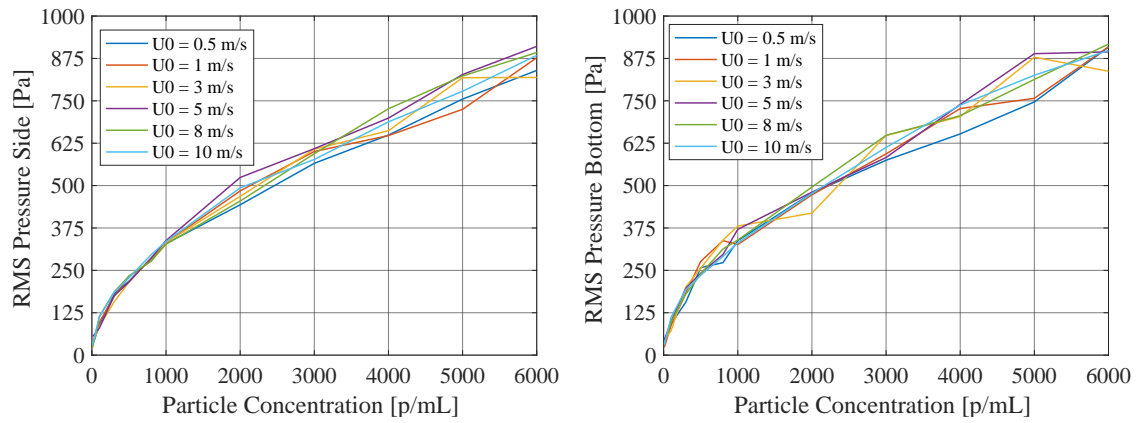


Figure 7.6. The average RMS scattering pressure over different flow velocities on the side and bottom surfaces as a function of the particle concentration. The particles are assumed to be rigid and with the size $a = 5\mu m$.

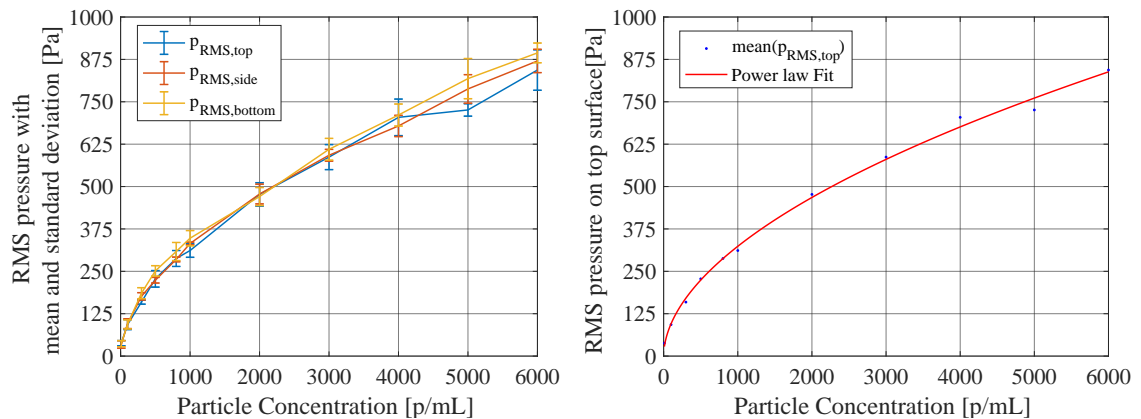


Figure 7.7. Mean and standard deviations over the flow velocities for the average RMS scattering pressure on the top, side, and bottom. Rigid particles with size $a = 5\mu m$.

Figure 7.8. One term power fit on the flow mean RMS scattering pressure on the top surface of the measurement tube. Rigid particles with size $a = 5\mu m$.

Figure 7.8 shows that the flow-mean RMS scattering pressure on the top surface of the measurement tube can be well approximated using the one term power fit with one term for rigid particles with size $a = 5\mu\text{m}$. The fit result for the flow mean average RMS scattering pressure on the top surface with a background pressure amplitude of 1MPa , gives:

$$p_{\text{sc,rms}} = \alpha \cdot \rho_{\text{pc}}^\beta \quad \text{where } \alpha = 8.273 \quad \beta = 0.5309 \quad (7.3)$$

$$R^2 = 0.9963$$

Rigid particle and $a = 10\mu\text{m}$

Increasing the particle radius from $5\mu\text{m}$ to $10\mu\text{m}$ should increase the scattering pressure by a factor of $2^3 = 8$ according to the far-field approximation (see Section 2.2.2). In Figure 7.9, four different 3D mirrored acoustic solution-sets with the associated RMS scattering pressure field on the outer fluid domain surfaces can be seen. The particle sizes are $a = 10\mu\text{m}$ and the particles are assumed rigid.

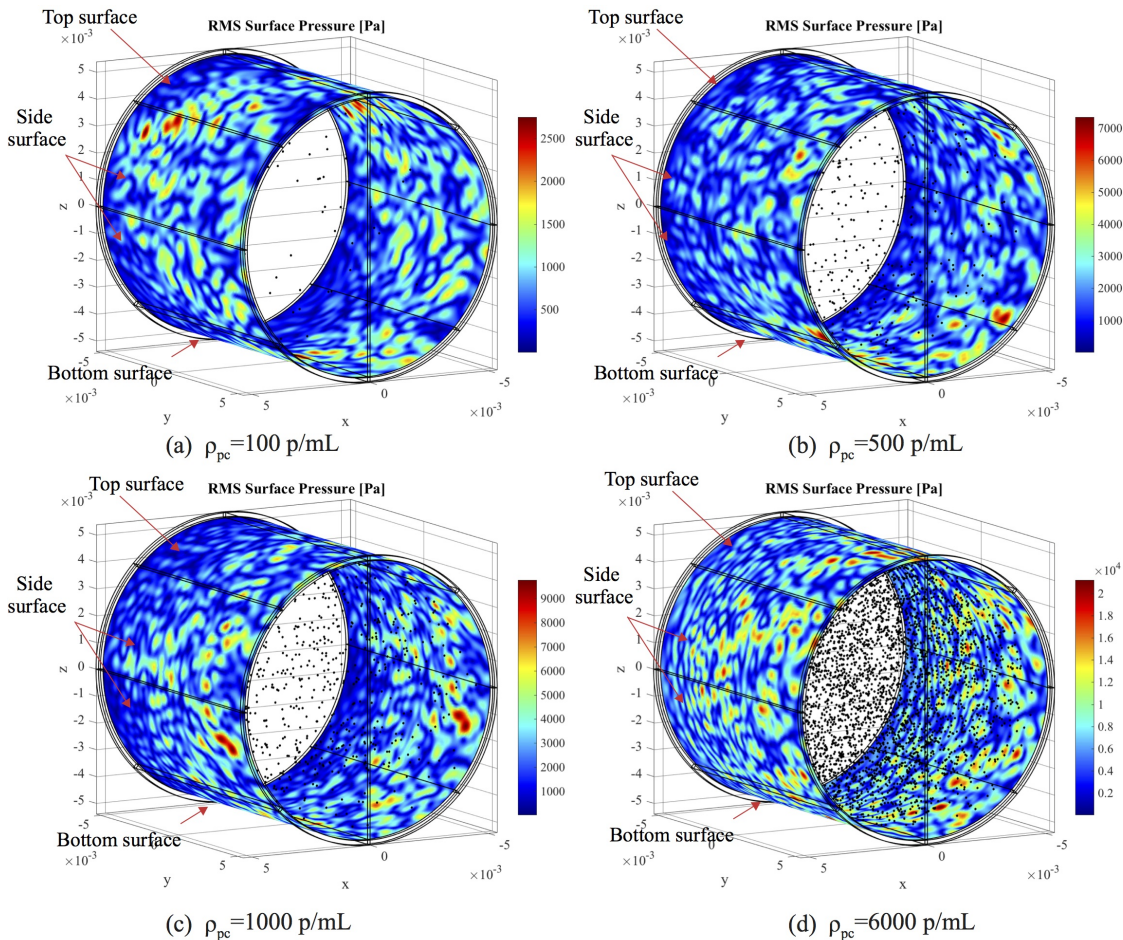


Figure 7.9. 3D mirrored acoustic solution-set with the RMS scattering pressure field on the outer fluid domain surfaces. The particle concentrations from 100 p/mL to 6000 p/mL, and an inlet flow velocity of 1 m/s. Rigid particles with size $a = 10\mu\text{m}$.

The flow mean average RMS scattering pressure for the top surface with $a = 5\mu\text{m}$ and with $a = 10\mu\text{m}$, can be seen in Figure 7.10. In Figure 7.10, the flow mean average RMS

scattering pressure for the top surface using $a = 5\mu\text{m}$ multiplied with the factor $2^3 = 8$ can also be seen. It can be seen that there is a good agreement between the flow mean average RMS scattering pressure for the top surface with $a = 5\mu\text{m}$ multiplied by the factor of 2^3 and the flow mean average RMS scattering pressure for the top surface with $a = 10\mu\text{m}$, indicating that the far-field approximation does apply to this problem.

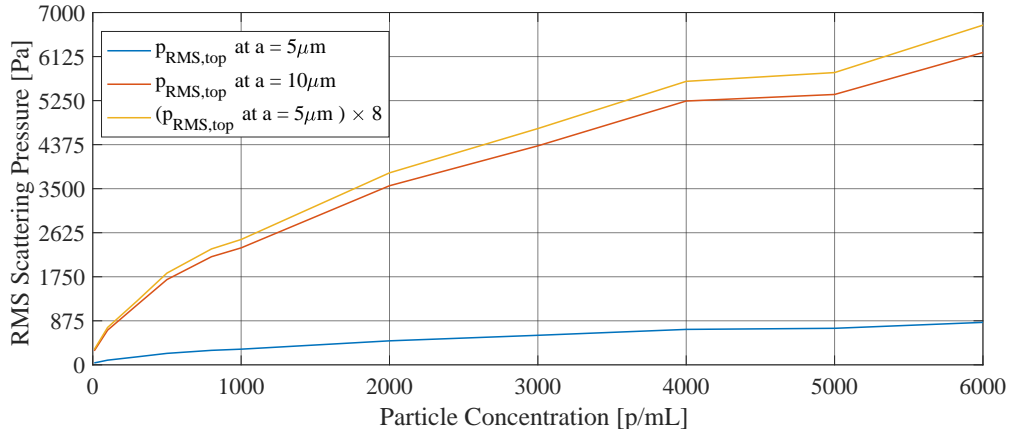


Figure 7.10. The average RMS pressure on the top surface as a function of the particle concentration and with different flow velocities. Rigid particles with size $a = 5\mu\text{m}$.

Figure 7.11 shows the flow mean and standard deviation of the average surface RMS scattering pressure for the top, side and bottom surface.

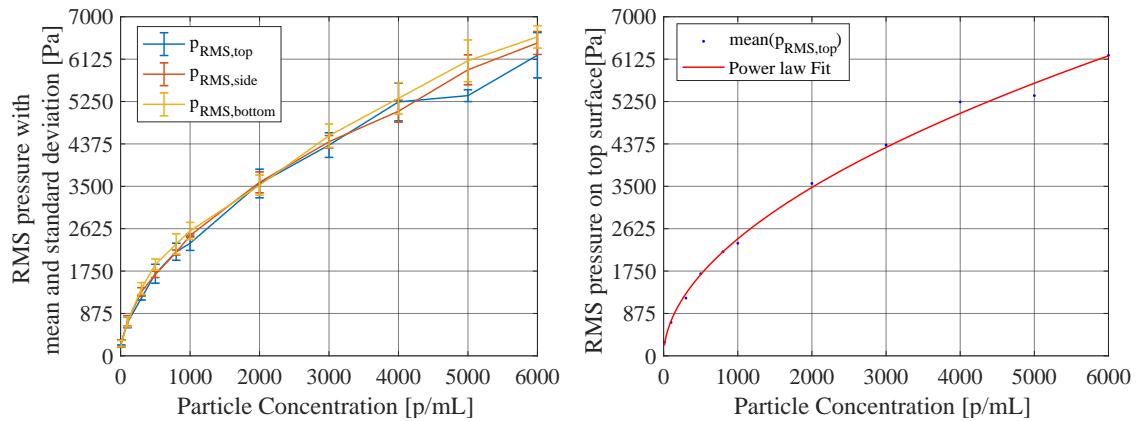


Figure 7.11. Mean and standard deviations over the flow velocities for the average RMS scattering pressure on the top, side and bottom surface. **Figure 7.12.** one term power fit on the flow mean RMS scattering pressure on the top surface of the measurement tube.

As for the sweep with $a = 5\mu\text{m}$, a one term power fit using the flow mean average RMS scattering pressure for the top surface can be seen in Figure 7.12. The fit result for the flow mean average RMS scattering pressure on the top surface with a rigid particle with

size $a = 10\mu m$ and a background pressure amplitude of $1MPa$, gives:

$$\begin{aligned} p_{sc,rms} &= \alpha \cdot \rho_{pc}^\beta \quad \text{where} \quad \alpha = 64.0475 \quad \beta = 0.5255 \\ R^2 &= 0.9964 \end{aligned} \quad (7.4)$$

Relating the one term power fit in Equation 7.3 with Equation 7.4, it can clearly be seen that the coefficient α in the case of a particle size $a = 10\mu m$ is close to a factor of 8 times larger than the coefficient α in the case of a particle size $a = 5\mu m$ ($\alpha = 8.273$, thus $8.273 \cdot 8 = 66.184$) as predicted by the far-field approximation.

Non-rigid particle and $a = 5\mu m$

In the problem statement (see Chapter 3) it can be seen that two material types are of interest for the turbidity measurements. The two materials are Silica with a density of $2500kg/m^3$ and speed of sound of $5960m/s$ and Polystyrene with at density of $1050kg/m^3$ and speed of sound of $2400m/s$. Figure 7.13, shows the 3D mirrored acoustic solution-set with the RMS scattering pressure field on the outer fluid domain surfaces, using (a) Silica to the left and (b) Polystyrene to the right. The particle concentration and inlet flow velocity seen in Figure 7.13, is of $1000p/mL$ and $1m/s$ respectively and the particle size is $a = 5\mu m$.

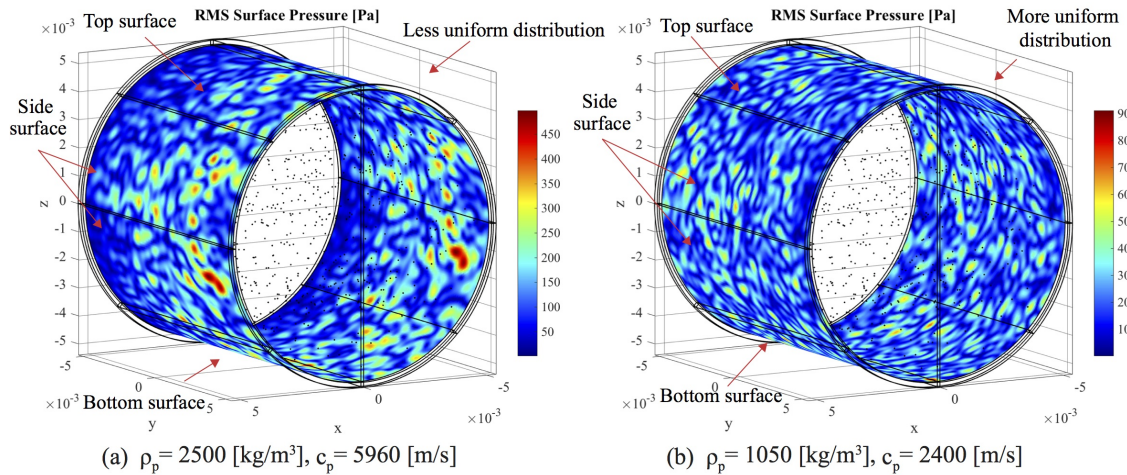


Figure 7.13. 3D mirrored acoustic solution-set with the RMS scattering pressure field on the outer fluid domain surfaces. The particle properties are to the left (a) Silica and to the right (b) Polystyrene. In both figures are the particle concentration $1000p/mL$ employed with a flow velocity of $1m/s$ and a particle size of $a = 5\mu m$.

In Figure 7.13 to the left, it can be seen that the RMS scattering pressure field is non-uniformly distributed and mainly concentrated at the entrance of the tube. In Figure 7.13 to the right, it can be seen that the RMS pressure is more uniformly distributed. This may be due to the small relative difference in the density of the particle and the fluid. In Section 2.2.2, it was found that the $\cos(\theta)$ term of the far-field approximation depends on the density difference between the particle and the fluid. Thus as seen in Figure 2.5 in

Section 2.2.2, the scattering is more evenly distributed in the far-field when the density difference is small as also evident in Figure 7.13.

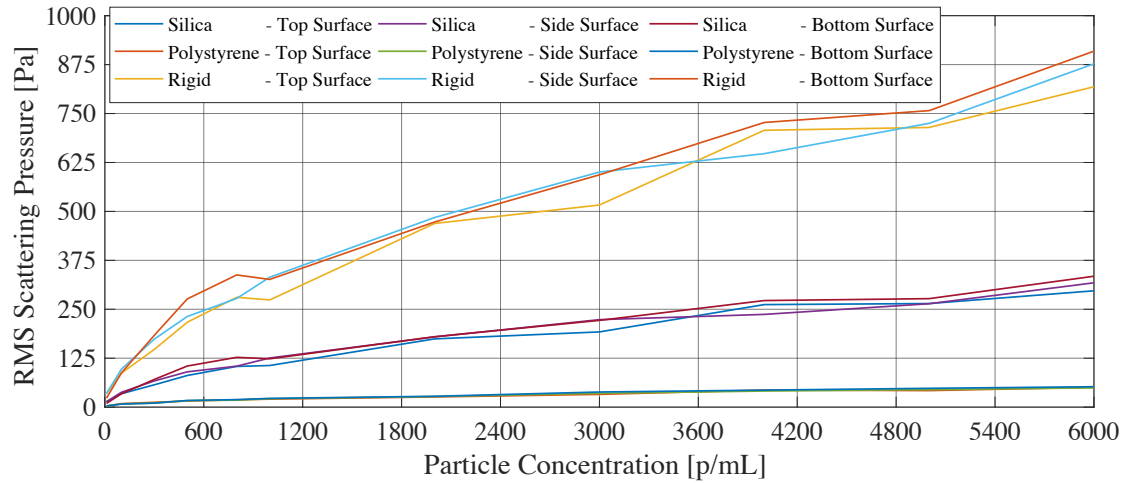


Figure 7.14. The average RMS scattering pressure on the top, side and bottom surface as a function of the particle concentration using the particle materials Silica, Polystyrene and rigid. The particle size is $a = 5\mu\text{m}$ and the flow inlet velocity is 1m/s .

Figure 7.14, shows the average RMS scattering pressure on the top, side and bottom surface as a function of the particle concentration using the particle materials Silica and Polystyrene, and assuming rigid particle. Figure 7.14, clearly shows that the amplitude scales as the particle properties gets less rigid. This characteristic can also be seen in the far-field approximation (see Section 2.2.2). In the far-field approximation, it can be seen that the scattering amplitude decreases as the bulk modulus of the particle approaches the bulk modulus of the fluid.

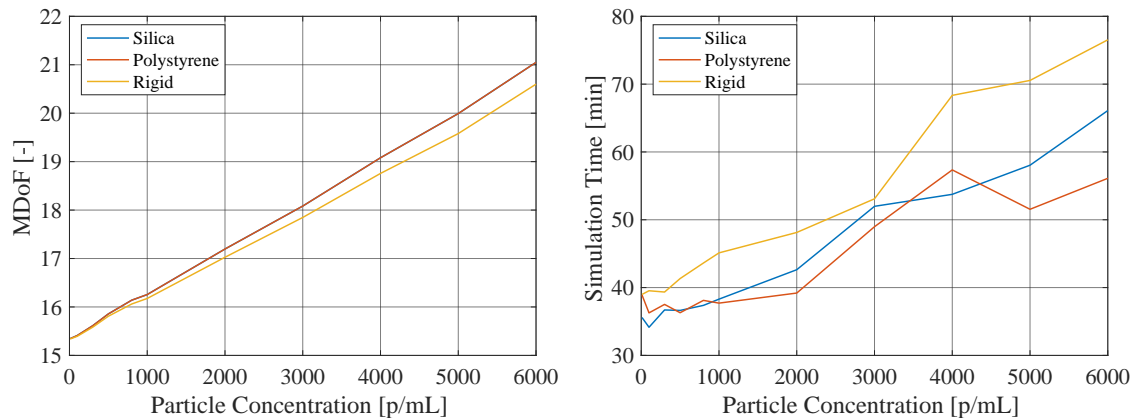


Figure 7.15. The figure to the left shows the problem size for the non-rigid and rigid simulations. The figure to the right shows the simulation time also for the non-rigid and rigid simulations. Particle size $a = 5\mu\text{m}$ and flow velocity of 1m/s .

Figure 7.15 to the left shows the problem size using non-rigid particle properties and the

rigid particle properties. It is expected that the problem size of the non-rigid particles is larger since the internal domains of each particle have to be meshed and simulated. It can, however, be seen in Figure 7.15 to the right that the simulation time is lower for the non-rigid simulations even though the problem size is larger. The decrease in simulation time may be a result of a higher convergence rate for the iterative solver due to lower gradients at the surface of the particles.

CONCLUSION

The primary purpose of this project has been to create a modeling framework that can be used as a model-based design tool for the development of an ultrasonic turbidity sensor.

An analytical solution to the scattering by a sphere in fluids has been found using separation of variables, together with the far-field approximation. Using the far-field approximation important properties of the scattering field amplitude has been identified. It has been found that the scattering field scales inverse proportional to the distance from the particle, scales with the frequency squared and scales with the particle size cubic.

A two stages modeling framework consisting of a CFD simulation and Particle Tracing simulation stage, and an Acoustic simulation stage, has been presented. In the first stage, it has been found that the flow is mainly turbulent and that a $k - \omega$ turbulence model, with wall-functions, is the most appropriate turbulence model for the fluid flow in the given geometry. The second part of the first stage, a time-domain particle simulation using the static flow solution has been conducted. It has been found that the Schiller-Naumann drag law is the most suitable drag law for the particle-fluid interaction. The particle release strategy has been chosen such that a continuous stream of particles is released into the computational domain.

For the acoustic simulations, only a static particle solution has been required. To retain a consistent static solution, a particle convergence analysis has been conducted. The convergence analysis has shown that the particle concentration is consistent after $N_{\text{sim}} = 3$ that is related to the simulation time by $t_{\text{sim}} = \frac{L_{\text{sensor}}}{U_0} \cdot N_{\text{sim}}$. Results from the particle tracing simulations have shown that the particle trajectories seem to circulate the surface of measurement tube as the fluid velocity increases.

It has been found that a frequency domain simulation is adequate for the purpose of scattering field simulations. Using a simplified model, critical parameters such as mesh size, problem size, and perfectly matched layers has been analyzed. Utilizing interpolated data from the numerical solution of the scattering field from a single particle, together with interpolated data from the corresponding analytical solution a relative accumulated error has been calculated indicating that the mesh size should have approximate eight nodes per wavelength. Taking the difference between the numerical and analytical solution of

the scattering problem have shown that numerical artifacts can be found in the scattering solution if the mesh resolution is inadequate.

An investigation of the PML thickness and layer thickness showed that a low number of layers affects the convergence rate of the iterative solver together with noneffective damping. It has also been found that a high number of layers increases the computational time due to a larger problem size. A trade-off between the effectiveness of the non-reflective properties of the PML, convergence and low simulation time, have been found using eight layers in the PML domains with only a small difference between the simulations using different PML thickness.

A solver analysis for the numerical acoustic scattering problem has been conducted using the simplified model. It has been shown that iterative solvers should be utilized due to the large problem size and that the iterative GMRES solver with Geometric Multigrid as preconditioner and PARADISO as coarse Solver, is the most usable solver for the problem in this work.

In the analysis of the particle distribution, it has been found that the particle spread changes significantly as a function of the flow velocity with a large section of the measurement tube not occupied by particles at high flow velocities. It has also been found that the size of the acoustic geometry is mainly limited by the memory available for the computation. Using a plane background wave frequency of 2MHz and 77GB of RAM, it has been found that a geometry consisting of a half cylinder with the radius equal to the radius of the measurement tube (5mm) and a length of 10mm, can be simulated. A base geometry has been conducted, and an automatic particle geometry generation algorithm has been developed in order to transform particle coordinates exported from the particle tracing simulation into a geometry that can be used in the acoustic stimulation. Meshing the combined acoustic base geometry with the particle geometry using the parameters found in the mesh convergence analysis gives a problem size of around 20M DoF.

A decrease in scattering amplitude as a consequence of the reduction in frequency from 10MHz to 2MHz has been compensated for by scaling the particle size. It has been found from the far-field approximation that the particle size should be scaled according to $a_s = a \cdot \left(\frac{10MHz}{2MHz}\right)^{2/3}$. Since the scaling approximation only applies in the far-field, an analysis of the particle-particle distances has been conducted. From the analysis of the particle distribution, it has been concluded that the majority of the particles are within in the far-field and that the expected backscattering error should be at most 5% using the scaling approximation, assuming a rigid particle.

It has been shown that the combined simulation can be used to sweep through different parameters like particle concentration, flow velocity, particle material and particle size, with the average RMS scattering pressure at various surfaces as the output of the combined simulation. From the combined simulation, it has been found that the average RMS

scattering pressure follows a one term power fit with $R^2 = 0.9963$, using rigid particles with a radius of $5\mu m$. It has also been found that the flow velocity does not disturb the average RMS scattering pressure significantly. The particle size has been found to some degree to follow the size scaling of the far-field approximation. The simulations of the non-rigid particles show that the average RMS scattering pressure scale significantly with the rigidity of the particles with an average RMS scattering pressure of $50Pa$, $297Pa$, $818Pa$ for Polystyrene, Silica, and a rigid particle respectively, at a particle concentration of $6000p/m^3$. It has also been found that the simulation time seems to decrease as the particles get less rigid.

DISCUSSION AND FUTURE WORK

In the fluid flow (CFD) analysis, severe convergence problems have occurred throughout the project. Much effort has been put into a mesh convergence analysis for the CFD simulation, yet limited by numerical convergence problems. An algebraic residual analysis has been used to pinpoint the areas in the geometry with large algebraic errors, which may indicate insufficient mesh resolution or sharp corners in the geometry [Ringh, 2016]. The algebraic residual analysis did, however, not lead to better convergence. An explanation is that the mesh convergence problems may be a result of non-linearities arising from an unsteady flow which is suppressed using a coarser mesh [COMSOL-Support, 2017]. Mesh convergence may, thus be found using a time domain simulation which should be exploited to gain more confidence in the CFD simulation results.

In the combined simulation, it was found that the average RMS scattering pressure did not change much with the inlet flow velocity. Relating the distribution of the particles for different flow velocities with the average RMS scattering pressure on the surface of the sensor shows that even though the internal distribution of particles varies significantly with the flow, it does not influence the surface pressure significantly. Thus indicating that the particle-particle multi-scattering interactions are limited to local scattering and that the RMS scattering pressure experienced on the surface is mainly due to particle scattering in the near vicinity of the surface. Beside interesting physical interpretations, the local scattering may be used to truncate the acoustical computational domain further by constructing a hollow cylinder geometry. It should, however, be noted that the fluid flow is anticipated to be more fluctuating, due to unsteady phenomenon's that is not resolved using the static CFD simulation. Fluctuations in the fluid flow may have a direct impact on the particle distribution in the near vicinity of the surface and can potentially influence the scattering pressure significantly.

In the scaling approximation, rigid particles are assumed. The error of the scaling approximation for non-rigid particles may, however, vary from this approximation since the $\cos(\theta)$ term of the particle-fluid density difference changes the amplitude in different directions. The scaling approximation should, therefore, be investigated using material types of interest to gain more confidence in the errors related to the scaling approximation.

The investigation of the particle release showed that even after particle convergence the

number of particles (NoP) as a function of time varies with up to 5% of the NoP target. Inconsistency may, therefore, be found in the scattering solution if another time instance after particle convergence is chosen. A more thorough investigation of the particle release strategy should hence be conducted. It is anticipated that an even more random release strategy would solve the problem.

The particle tracing simulation assumed a sparse flow. At high particle concentrations may other flow types, however, be more suitable which should be examined in future works.

MATHEMATICS FOR THE DERIVATION OF THE SCATTERING PROBLEM

The boundary condition problem described in Section 2.2.1 will be solved in this appendix, together with some properties and background theory about Bessel, Hankel and Legendre functions.

A.1 The Derivation of the Scatter Field Coefficients

The boundary condition on the surface of the sphere must be continuous, as described in Section 2.2.1. The equations for the incident wave, the scatter wave and flaw wave can be found in Equations 2.27, Equation 2.26 and Equation 2.28, respectively. The pressure on the boundary ($r = a$) of the sphere can be written as:

$$p_{\text{inc}} + p_{\text{sc}} = p_{\text{flaw}} \quad (\text{A.1})$$

$$\sum_{n=0}^{\infty} \left\{ i^n (2n+1) j_n(k_2 a) + C_n h_n^{(1)}(k_2 a) - D_n j_n(k_1 a) \right\} P_n(\cos(\theta)) = 0 \quad (\text{A.2})$$

The normal velocity on the boundary of the sphere can be written as:

$$\frac{1}{\rho_2} \frac{\partial p_{\text{inc}}}{\partial r} + \frac{1}{\rho_2} \frac{\partial p_{\text{sc}}}{\partial r} = \frac{1}{\rho_1} \frac{\partial p_{\text{flaw}}}{\partial r} \quad (\text{A.3})$$

Both the incident, scatter and flaw wave has Bessel and Hankel functions that are dependent on the radius r . It is, however, convenient to differentiate the functions with respect to its entire argument (see the differentiation properties of the Bessel and Hankel functions in Equation A.12). The following relation is therefore used for the Bessel function of the first kind (the relation also applies to j_n , n_n and h_n):

$$\frac{\partial j_n(kr)}{\partial r} = k \frac{\partial j_n(kr)}{\partial kr} = k [j_n(kr)]' \quad (\text{A.4})$$

Using the relation in Equation A.4, the normal velocity on the boundary ($r = a$) can be written as:

$$\frac{1}{\rho_2} \frac{\partial p_{\text{inc}}}{\partial r} + \frac{1}{\rho_2} \frac{\partial p_{\text{sc}}}{\partial r} = \frac{1}{\rho_1} \frac{\partial p_{\text{flaw}}}{\partial r} \quad (\text{A.5})$$

$$\sum_{n=0}^{\infty} \left\{ \frac{i^n(2n+1)k_2[j_n(k_2a)]' + C_n k_2 [h_n^{(1)}(k_2a)]'}{\rho_2} - \frac{D_n k_1 [j_n(k_1a)]'}{\rho_1} \right\} P_n(\cos(\theta)) = 0 \quad (\text{A.6})$$

For the expressions in the breakages in Equation A.2 and Equation A.6 form two equations with two unknown. Solving for the scatter field wave amplitude C_n , gives:

$$C_n = -i^n(2n+1) \frac{[j_n(k_2a)]' j_n(k_1a) k_2 \rho_1 - [j_n(k_1a)]' j_n(k_2a) k_1 \rho_2}{[h_n^{(1)}(k_2a)]' j_n(k_1a) k_2 \rho_1 - [j_n(k_1a)]' h_n^{(1)}(k_2a) k_1 \rho_2} \quad (\text{A.7})$$

Using the relations $k_1 = \frac{\omega}{c_1}$, $k_2 = \frac{\omega}{c_2}$ which as ratio gives $\frac{k_2}{k_1} = \frac{c_1}{c_2}$, the scatter field wave amplitude C_n can be re-written only regarding speed of sound and density:

$$C_n = \frac{i^n(2n+1)}{\Omega} \left\{ \frac{j_n(k_2a)[j_n(k_1a)]'}{\rho_1 c_1} - \frac{j_n(k_1a)[j_n(k_2a)]'}{\rho_2 c_2} \right\} \quad (\text{A.8})$$

$$\Omega = \frac{j_n(k_1a)[h_n^{(1)}(k_2a)]'}{\rho_2 c_2} - \frac{h_n(k_2a)[j_n(k_1a)]'}{\rho_1 c_1} \quad (\text{A.9})$$

A.2 Properties and Background for the Bessel functions, Hankel functions and Legendre functions

A.2.1 Spherical Hankel and Spherical Bessel functions

The spherical Hankel function of the first kind $h_n^{(1)}$ is defined as the solution to a differential equation of the following form [Morse & Ingard, 1968, p. 336]:

$$\frac{d^2 R}{d\zeta^2} + \frac{2}{\zeta} \frac{dR}{d\zeta} + [\zeta + n(n+1)] \frac{R}{\zeta^2} = 0 \quad (\text{A.10})$$

Either the spherical Bessel function of first (j_n) and the second kind (n_n) as well the spherical Hankel function, will have these properties [Morse & Ingard, 1968]:

$$j_{n-1}(\zeta) + j_{n+1}(\zeta) = \frac{2n+1}{\zeta} j_n(\zeta) \quad (\text{A.11})$$

$$\frac{d}{d\zeta} j_n(\zeta) = [j_n(\zeta)]' = \frac{1}{2n+1} [n j_{n-1}(\zeta) - (n+1) j_{n+1}(\zeta)] \quad (\text{A.12})$$

Combining Equation A.11 and Equation A.12 gives a very useful relation without $n < 0$:

$$[j_n(\zeta)]' = n \frac{j_n(\zeta)}{\zeta} - j_{n+1}(\zeta) \quad (\text{A.13})$$

Some of the Hankel functions of the first kind [Morse & Ingard, 1968, p. 336]:

$$h_0(\zeta) = \frac{e(i\zeta)}{i\zeta} \quad h_1(\zeta) = -\frac{e(\zeta)}{\zeta} \left(1 + \frac{i}{\zeta}\right) \quad h_2(\zeta) = \frac{i e(i\zeta)}{\zeta} \left(1 + \frac{3i}{\zeta} - \frac{3}{\zeta^2}\right) \quad (\text{A.14})$$

Some of the spherical Bessel functions [Morse & Ingard, 1968, p. 337]:

$$j_0(\zeta) = \frac{\sin(\zeta)}{\zeta} \quad n_0(\zeta) = -\frac{\cos(\zeta)}{\zeta} \quad (\text{A.15})$$

$$j_1(\zeta) = \frac{\sin(\zeta)}{\zeta^2} - \frac{\cos(\zeta)}{\zeta} \quad n_1(\zeta) = -\frac{\sin(\zeta)}{\zeta} - \frac{\cos(\zeta)}{\zeta^2} \quad (\text{A.16})$$

A.2.2 Legendre functions

The Legendre functions $P_n(\eta)$ is the solution to the differential equation of the following from [Morse & Ingard, 1968, p. 333]:

$$(1 - \eta^2) \frac{d^2 P}{d\eta^2} - 2\eta \frac{dP}{d\eta} + n(n + 1)P = 0 \quad (\text{A.17})$$

where P is the variable solved for, n is an integer and η is independent variable or function. In the case of spherical radiation $\eta = \cos(\theta)$.

Some of the Legendre functions [Morse & Ingard, 1968, p. 334]:

$$n = 0 \quad P_0(\eta) = 1 \quad (\text{A.18})$$

$$n = 0 \quad P_0(\cos(\theta)) = 1 \quad (\text{A.19})$$

$$n = 1 \quad P_1(\eta) = \eta \quad (\text{A.20})$$

$$n = 1 \quad P_1(\cos(\theta)) = \cos(\theta) \quad (\text{A.21})$$

$$n = 2 \quad P_2(\eta) = \frac{1}{2}(3\eta^2 - 1) \quad (\text{A.22})$$

$$n = 2 \quad P_2(\cos(\theta)) = \frac{1}{4}(3\cos(2\theta) + 1) \quad (\text{A.23})$$

A.3 Some Useful Asymptotics

In the determination of the far-field approximation of the scattering field in Section 2.2.2, some asymptotics for the Bessel and Hankel functions was used. The asymptotics is found using by expanding the functions into series. The function *series* in Maple is used for this purpose.

$$j_0(z) = \frac{\sin(z)}{z} \xrightarrow{\text{series}} 1 - \frac{1}{6}z^2 + \dots \quad (\text{A.24})$$

$$j_0(z) \sim 1 \quad \text{as } (z \rightarrow 0)$$

$$j_1(z) = \frac{\sin(z)}{z^2} - \frac{\cos(z)}{z} \xrightarrow{\text{series}} \frac{1}{3}z - \frac{1}{30}z^3 + \dots \quad (\text{A.25})$$

$$j_1(z) \sim \frac{1}{3}z \quad \text{as } (z \rightarrow 0)$$

$$[j_0(z)]' = \frac{\cos(z)}{z} - \frac{\sin(z)}{z^2} \xrightarrow{\text{series}} -\frac{1}{3}z + \frac{1}{30}z^3 + \dots \quad (\text{A.26})$$

$$[j_0(z)]' \sim -\frac{1}{3}z \quad \text{as } (z \rightarrow 0)$$

$$[j_1(z)]' = \frac{(z^2 - 2)\sin(z) - 2\cos(z)z}{z^3} \xrightarrow{\text{series}} \frac{1}{3} - \frac{1}{10}z^2 + \frac{1}{168}z^4 + \dots \quad (\text{A.27})$$

$$[j_1(z)]' \sim \frac{1}{3} \quad \text{as } (z \rightarrow 0)$$

$$h_0(z) = \frac{e^{iz}}{iz} \xrightarrow{\text{series}} -\frac{i}{z} + 1 + \frac{1}{2}iz - \frac{1}{6}z^2 + \dots \quad (\text{A.28})$$

$$h_0(z) \sim -\frac{i}{z} \quad \text{as } (z \rightarrow 0)$$

$$h_1(z) = -\frac{ie(z)}{z} \left(1 + \frac{i}{z}\right) \xrightarrow{\text{series}} -\frac{i}{z^2} - \frac{1}{2}i + \frac{1}{3}z + \frac{1}{8}iz^2 - \dots \quad (\text{A.29})$$

$$h_1(z) \sim -\frac{i}{z^2} \quad \text{as } (z \rightarrow 0)$$

$$[h_0(z)]' = \frac{e^{iz}}{z} \left(1 + \frac{i}{z}\right) \xrightarrow{\text{series}} \frac{i}{z^2} + \frac{1}{2}i - \frac{1}{3}z - \frac{1}{8}iz^2 + \dots \quad (\text{A.30})$$

$$[h_0(z)]' \sim \frac{i}{z^2} \quad \text{as } (z \rightarrow 0)$$

$$[h_1(z)]' = -\frac{e^{iz}}{z^3} (i(z^2 - 2) - 2z) \xrightarrow{\text{series}} \frac{2i}{z^3} + \frac{1}{3} + \frac{1}{4}iz - \frac{1}{10}z^2 + \dots \quad (\text{A.31})$$

$$[h_1(z)]' \sim \frac{2i}{z^3} \quad \text{as } (z \rightarrow 0)$$

GEOMETRY SIMPLIFICATION AND MESH CONVERGENCE FOR FLOW AND PARTICLE SIMULATIONS

The geometry of the ULTRAFLOW 14 flow sensor made by Kamstrup A/S are simplified in order to be more workable for numerical simulations. A side view of the non-simplified geometry and the simplified geometry can be seen in Figure B.1 and Figure B.2, respectively.

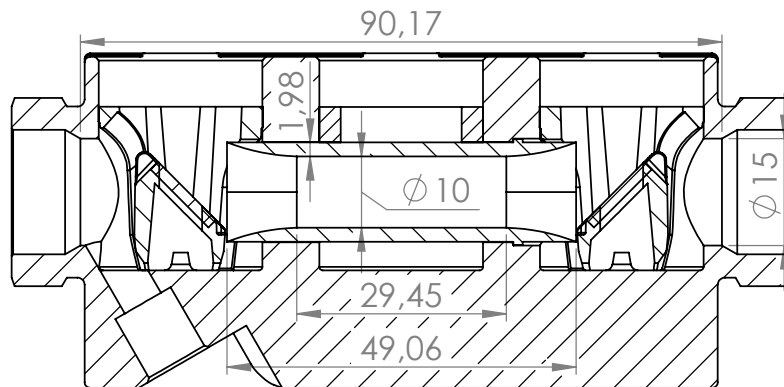


Figure B.1. Side view of Kamstrup ULTRAFLOW 14 flow sensor modified to be used as a turbidity sensor

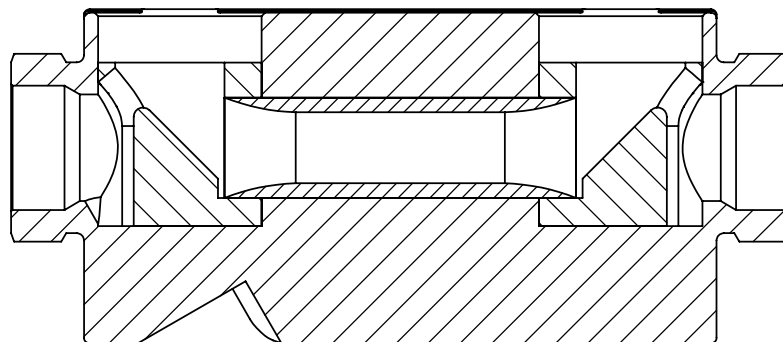


Figure B.2. Side view of the simplified Kamstrup ULTRAFLOW 14 flow sensor, to be used for numerical simulations

FLOW INLET MODEL

The geometry for the inlet flow model is constructed using an axis symmetric 2D model, which is much easier to solve than a full 3D model. The geometry constructed as a long pipe with an inlet diameter of 15mm and a length of 50 times the inlet diameter as described in Subsection 5.2.4.

The inlet condition for the model is the average inlet flow U_0 and the outlet boundary condition set equal to a pressure of zero, with a normal flow. The mesh is constructed as suggested in [COMSOL, 2017e] with two mapped meshes. In the first mapped mesh, the distribution along the symmetry axis and outer wall of the pipe are set equal to 50 nodes with equal distance between each node. Using the second mapped mesh, 20 nodes are allocated on the inlet and outlet, distributed with most nodes on the outer boundary of the pipe as seen in Figure C.1.

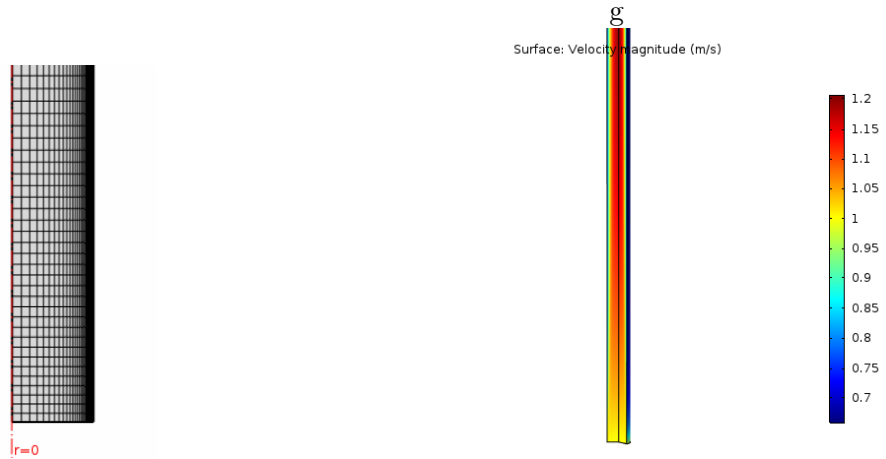


Figure C.1. The mapped mesh of the inlet flow **Figure C.2.** The resulting flow profile using the model. It can be seen that the inlet (and outlet) $k-\omega$ turbulence model with an inlet average flow boundary condition in the model is mapped using of $U_0 = 1m/s$ a non-equal distribution with most mesh nodes closest to the wall.

RELATIVE REYNOLDS NUMBER FOR PARTICLE TRACING

The relative Reynolds number is described in Section 5.3. The drag relations, seen in Section 5.3, are valid for different ranges of relative Reynolds number. Simulating the particle trajectories using the Standard Drag law that combines different drag laws for different relative Reynolds number is very slow, but it is expected that the maximum local relative Reynolds number calculated can be used as a measure of the relative Reynolds generally found in the particle tracing problem.

Figure D.1 shows the relative Reynolds number using the Standard Drag law [COMSOL, 2017g] with an inlet velocity of 0.5 m/s and a particle concentration of 100 particles/mL. The time instance is after particle concentration convergence (see Section 5.3 for more information about particle concentration convergence)

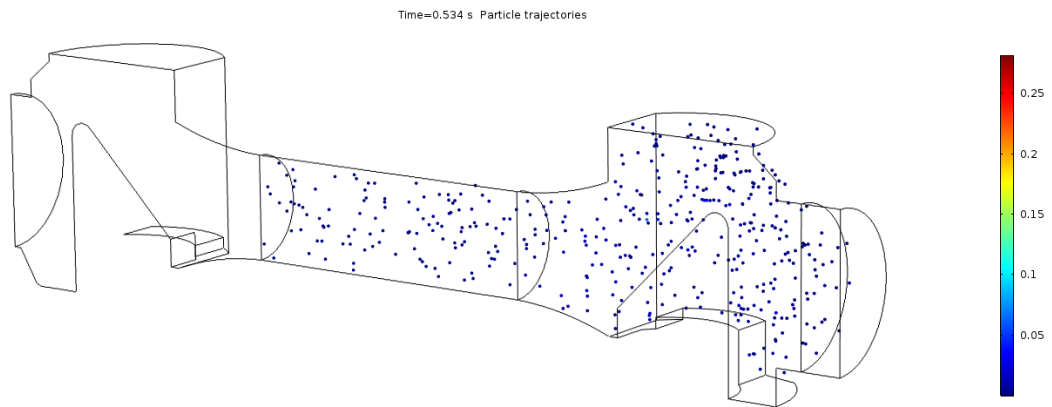


Figure D.1. Relative Reynolds number using a particle concentration of 100 particles/mL and a fluid velocity of 0.5 m/s

Figure D.2 shows the relative Reynolds number using the Standard Drag law [COMSOL, 2017g] with an inlet velocity of 10 m/s.

From Figure D.1 and Figure D.2, it can be seen that the relative Reynolds number does not excite $Re_r = 10$. Assuming that the particle concentration converged time instance can be used to generalize the relative Reynolds number for all other time instances, the

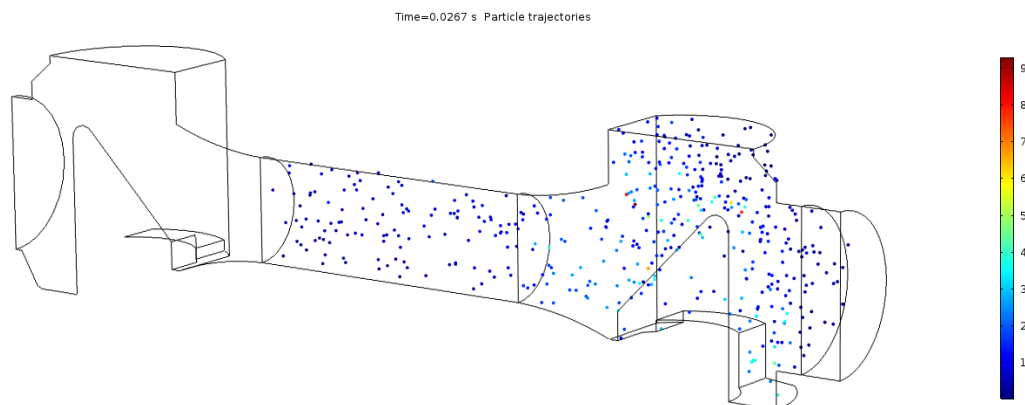


Figure D.2. Relative Reynolds number using a particle concentration of 100 particles/mL and a fluid velocity of 10 m/s. The time instance is after particle concentration convergence.

over limit for the relative Reynolds number in this work is $Re_r = 10$.

INVESTIGATION OF MESH FOR ACOUSTIC SIMULATIONS

As described in Section 6.2.1, the acoustic mesh consist of three different types of mesh, namely a free tetrahedral mesh, a swept mesh in the PML domain, and a boundary layer mesh. The free tetrahedral mesh is controlled using a size node. The size node consists of five different parameters, max size, min size, maximum element growth rate, curvature factor and resolution of narrow regions. The maximum element size n_{\max} is controlled using a Nyquist-like theorem as explained in Section 6.2.1. The minimum element size is control by the size of the particles. The curvature factor and resolution of narrow regions controls the number of elements around the particle. Figure E.1 shows the mesh influence of different curvature factor and growth rate settings. Figure E.2 and Figure E.3 shows the influence of different curvature settings and growth rate settings on the scattering pressure in the 0 deg and 180 deg directions, respectfully. The resolution of narrow regions does not influence the mesh around the particle. Table E shows the settings used in this work.

Parameter	Features
max size	λ_0/N
min size	R_i/N
maximum element growth rate	1.5
curvature factor	1
resolution of narrow regions	1

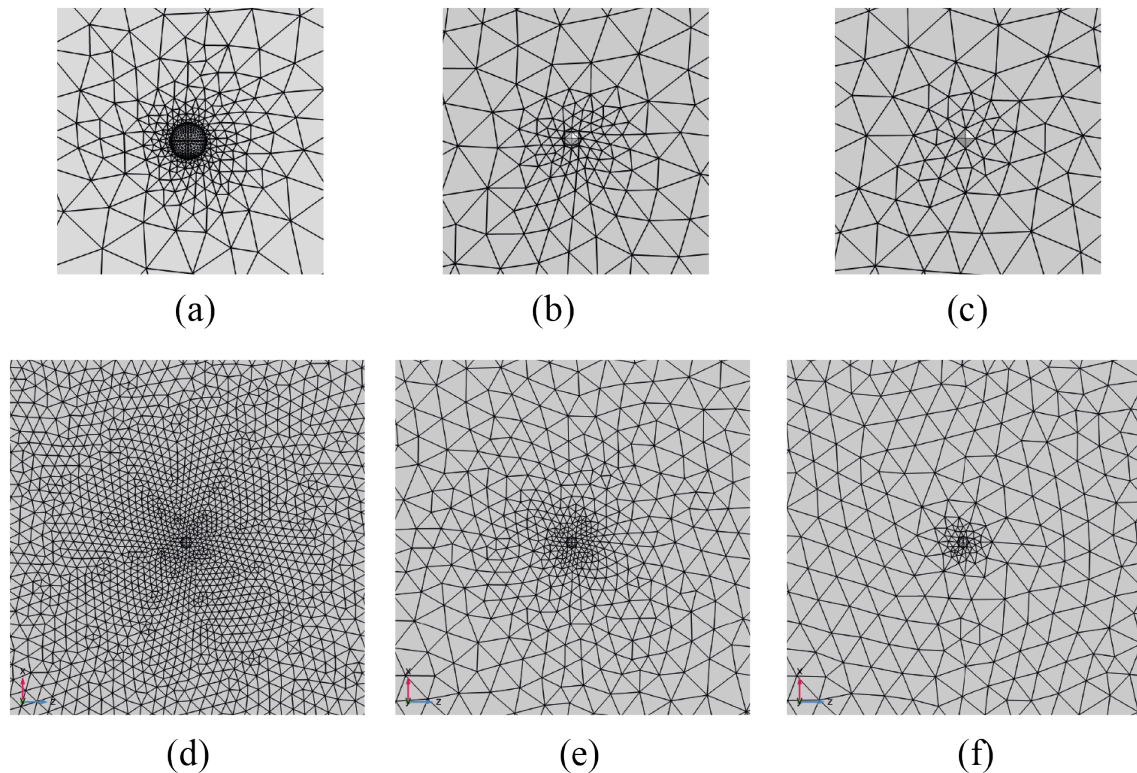


Figure E.1. The influence on the mesh using, from (a) to (c), different curvature settings and from (d) to (e) different growth rate settings.

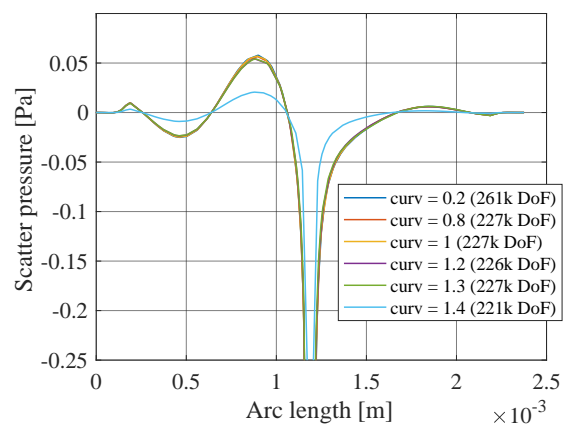


Figure E.2. The influence of different curvature settings on the scattering pressure in the 0 deg and 180 deg directions.

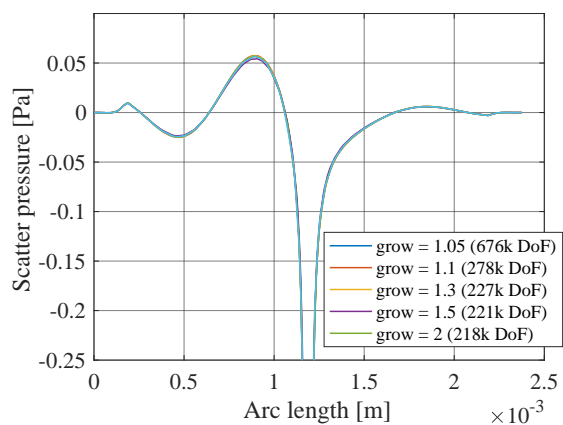


Figure E.3. The influence of different growth rate settings on the scattering pressure in the 0 deg and 180 deg directions.

SCRIPTS AND ALGORITHMS

F.1 Particle Coordinate Selection Function

Script to search through all particle coordinates and find the particles within a selected range on the y-axis. Particle coordinates one particle diameter from the x-axis is ignored as explained in Section 6.3.1.

```
function out = particle_view_selection_fcn(particle)
% out = particle_view_selection_fcn(particle)
% Required variables
% - particle.data;      % Particle coordinates
% - particle.a;        % Radius of particles
% - particle.view_area; % The size of the view area
% Output variables
% - particle.pos       % Selected particle coordinates
% - particle.data_m_pos % Particle coordinates without selected
%% Take only section of particles in scope
j = 0; t = 0;
for i = 1:length(particle.data)
    if particle.data(i,1) < -particle.a*2
        if particle.data(i,2) < particle.view_area/2 ...
            && particle.data(i,2) > -particle.view_area/2
            j=j+1;
            particle.pos(j,1) = particle.data(i,1); %x coordinates
            particle.pos(j,2) = particle.data(i,2); %y coordinates
            particle.pos(j,3) = particle.data(i,3); %z coordinates
        else
            t = t+1;
            particle.data_m_pos(t,1) = particle.data(i,1); %x coordinates
            particle.data_m_pos(t,2) = particle.data(i,2); %y coordinates
            particle.data_m_pos(t,3) = particle.data(i,3); %z coordinates
        end
    end
end
out = particle;
```

F.2 Acoustic Particle Geometry Generation Algorithm

The particle geometry is set up by sweeping through all selected particles and creating a spherical object with radius a at the, of each particle, associated coordinate sets.

```
function comb_acoustic_gen_fcn(particle ,main_path)
% comb_acoustic_gen_fcn(particle ,main_path)
% Auto-generation of the acoustic domain using particle positions
% Required variables
```

```

% - main_path      % Main path
% - particle.pos   % Selected particle coordinates
%% Pre-routine
% Export path and creation of export dictionary
export_path = [main_path 'Results\Acoustic_geom_R10\']; mkdir(export_path)
% Path to selected particle coordinates
particle_path = [main_path 'Results\CFD_particle\'];
particle.data = 0; particle.pos = 0;
% Acquire the list of particles coordinate files
dir_info = dir([particle_path '*.csv']);
particle_coordinate_str = natsort({dir_info.name});
%% Generation of model geometry
for i = 1:length(particle_coordinate_str); tic
    % Export name using selected particle coordinate file
    export_name = ['acoustic_geom_v4_' particle_coordinate_str{i}(...
        strfind(particle_coordinate_str{i}, 'pos'):end-4)];
    % Continue if the file already exist
    if exist([export_path export_name '.mat'])==2
        disp('File already exist!'); continue
    end
    % Clearing old variables
    particle = rmfield(particle, {'data', 'pos'}); clear model gen_data;
    % File selection and particle coordinates
    particle.data = csvread([particle_path particle_coordinate_str{i}], 8);
    % Determination of subsection of investigation
    particle = particle_view_selection_fcn(particle);
    % Create COMSOL geometry and export of geometry to COMSOL .mphbin
    % format
    model = particle_geom_COMSOL_fcn_v2(particle);
    model.geom('geom1').export([export_path export_name '.mphbin']);
    % Generation data
    gen_data.gen_time = toc;
    gen_data.file_name = particle_coordinate_str{i};
    gen_data.N_particles = length(particle.pos);
    % Save data about the generation for later use
    save([export_path export_name '.mat'], 'gen_data')
end

function out = particle_geom_COMSOL_fcn_v2(particle)
% particle_geom_COMSOL_fcn(particle, cyl)
% Function to generate acoustic particle geometry
% Required variables
% - particle.a      % Particle radius
% - particle.pos    % Selected particle coordinates
% Output is a model struct for COMSOL Livelink
%% Initial setup
import com.comsol.model.*
import com.comsol.model.util.*
model = ModelUtil.create('Model');

%% Parameter settings
model.param.set('Rp', num2str(particle.R));
model.modelNode.create('comp1');
model.geom.create('geom1', 3);
%% particle generation
for i = 1:length(particle.pos)
    model.geom('geom1').create(['sph' num2str(i)], 'Sphere');
    model.geom('geom1').feature(['sph' num2str(i)]).set('r', 'Rp');
    model.geom('geom1').feature(['sph' num2str(i)]).set('pos', ...
        {num2str(particle.pos(i,1)) num2str(particle.pos(i,2)) num2str(particle.pos(i,3))});
end
%% Geometry construct
model.geom('geom1').run;
model.geom('geom1').run('fin');
out = model;

```

F.3 Particle-Particle Interaction Analysis

The scripts for the particle-particle analysis calculates the distance between all particles, which is used to analyze the number of particle-particle interactions as seen in Section 6.5.

```

%% Particle-Particle Interaction Analysis
close all; clc; clear all
particle_path = '/Results/CFD_particle/'; delete('particle_result.mat')
rho_str_vec = [10 100 300 500 800 1000 2000 3000 4000 5000 6000];
u0_str_vec = [0.5 1 3 5 8 10];
for j = 1:length(u0_str_vec)
    for i = 1:length(rho_str_vec)
        clear particle
        file_name = [particle_path 'particle_pos_u0_' num2str(u0_str_vec(j)) ...
                    '_rho_pc' num2str(rho_str_vec(i)) '.csv'];
        particle.data = csvread(file_name,8);
        %% Parameters for the loop
        particle.view_area = 10e-3;
        particle.a = 5e-6*(10e6/2e6)^(2/3); % Particle size with scaling
        particle.dist_critical_10d = (1+10)*particle.a*2;
        particle.dist_critical_20d = (1+20)*particle.a*2;
        particle.dist_critical_50d = (1+50)*particle.a*2;
        %% Calculation functions
        particle = particle_view_selection_fcn(particle);
        particle = particle_dist_fcn(particle);
        %% Save to result str
        particle_result.rho_str_vec = rho_str_vec;
        particle_result.u0_str_vec = u0_str_vec;
        particle_result.Ndist_critical_10d(i,j) = particle.Ndist_critical_10d;
        particle_result.Ndist_critical_20d(i,j) = particle.Ndist_critical_20d;
        particle_result.Ndist_critical_50d(i,j) = particle.Ndist_critical_50d;
        particle_result.Npp_critical_10d(i,j) = mean(particle.Ndist_critical_pp10d);
        particle_result.Npp_critical_20d(i,j) = mean(particle.Ndist_critical_pp20d);
        particle_result.Npp_critical_50d(i,j) = mean(particle.Ndist_critical_pp50d);
        particle_result.Ndist_posible(i,j) = particle.Ndist_posible;
        particle_result.N(i,j) = particle.N;
        particle_result.mean_dist_next(i,j) = mean(particle.dist_to_next);
        particle_result.mean_dist_next4(i,j) = mean(particle.mean_dist_to_next4);
        particle_result.std_dist_next(i,j) = std(particle.dist_to_next);
        particle_result.p(i,j) = rmfield(particle, 'data');
    end
end
save('particle_result.mat','particle_result')

function out = particle_dist_fcn(particle)
% Particle distance calculation by means of euclidean norm
% out = particle_dist_fcn(particle)
% required variables
% - particle.dist_critical for 10d & 20d & 50d
% - particle.pos
dist = zeros(length(particle.pos),length(particle.pos));
%% Calculation of distances between particles
for i = 1:length(particle.pos)
    % Display process
    counter = process_line_fcn(i,length(particle.pos),counter);
    start_pos_j = i+1;
    for j = start_pos_j:length(particle.pos)
        dist(i,j) = sqrt((particle.pos(i,1)-particle.pos(j,1))^2+...
                        (particle.pos(i,2)-particle.pos(j,2))^2+...
                        (particle.pos(i,3)-particle.pos(j,3))^2);
    end
end
end
%% Distance to next particle

```

```
% Creates a symmetric matrix and adds ones in the diagonal which is usefull
% later
particle.dist_matrix = dist'+dist;
particle.dist_matrix = particle.dist_matrix+diag(ones(1,length(particle.dist_matrix)));
% Number of particles
particle.N = length(particle.dist_matrix);
% Calculates distance to nearest particle (if there were no ones in the diag
% then this command would return zeros
particle.dist_to_next = min(particle.dist_matrix);
% Calculates distance to nearest four particles
dist_to_next4 = sort(particle.dist_matrix);
if length(dist_to_next4)<=4
    particle.mean_dist_to_next4 = 0;
else
    particle.mean_dist_to_next4 = mean(dist_to_next4(1:4,:));
end
% Calculates the number of distances that are within some limit
particle.Ndist_critical_10d = sum(sum(particle.dist_matrix<particle.dist_critical_10d));
particle.Ndist_critical_20d = sum(sum(particle.dist_matrix<particle.dist_critical_20d));
particle.Ndist_critical_50d = sum(sum(particle.dist_matrix<particle.dist_critical_50d));
% Calcultes the number of distances per particle that are within some limit
particle.Ndist_critical_pp10d = sum(particle.dist_matrix<particle.dist_critical_10d);
particle.Ndist_critical_pp20d = sum(particle.dist_matrix<particle.dist_critical_20d);
particle.Ndist_critical_pp50d = sum(particle.dist_matrix<particle.dist_critical_50d);
% Calculates the total number of possible distances
particle.Ndist_posible = particle.N^2-particle.N;
out = particle;
```

BIBLIOGRAPHY

- Abda, F., Azbaid, A., Ensminger, D., Fischer, S., François, P., Schmitt, P., & Pallarés, A. (2009). Ultrasonic device for real-time sewage velocity and suspended particles concentration measurements. *Water Sci. Technol.*, 60(1), 117–125.
- Arnau Vives, A. (2008). *Piezoelectric Transducers and Applications*. Berlin, Heidelberg: Springer Berlin Heidelberg.
- Berenger, J.-P. (1994). A perfectly matched layer for the absorption of electromagnetic waves. *J. Comput. Phys.*, 114(2), 185–200.
- Bratby, J. (2015). Turbidity: Measurement of Filtrate and Supernatant Quality? In S. Tarleton (Ed.), *Prog. Filtr. Sep.* (pp. 637–657). Oxford: Academic Press.
- Casey, M. & Wintergerste, T. (2000). Best Practice Guidelines.
- Çengel, Y. A., Cimbala, J. M., & Turner, R. H. (2012). *Fundamentals of Thermal-Fluid Sciences 4ed.*
- COMSOL (2017a). Acoustic Scattering off an Ellipsoid - Application note. *COMSOL website*, 5.3.
- COMSOL (2017b). Acoustics Module User Guide. *COMSOL website*, 5.2a.
- COMSOL (2017c). CFD Module User Guide. *COMSOL website*, 5.3.
- COMSOL (2017d). Comsol Multiphysics Reference Manual. *COMSOL website*, 5.2a.
- COMSOL (2017e). Flow Through a Pipe Elbow - Application Note. *COMSOL website*, 5.2a.
- COMSOL (2017f). Introduction to the CFD Module. *COMSOL website*, 5.3.
- COMSOL (2017g). Particle Tracing Module User's Guide. *COMSOL website*, 5.2a.
- COMSOL-Support (2017). Conversation with COMSOL support. *COMSOL Support*, 5.3.
- Fischer, S. (2009). A new high resolution velocity and acoustic turbidity profiler for open-channels. (pp. 35–38).
- Fitch, J. (2011). Control and Management of Particle Contamination in Hydraulic Fluids. In *Handb. Hydraul. Fluid Technol. Second Ed.* (pp. 219–256). CRC Press.

- Frei, W. (2013a). Meshing Considerations for Nonlinear Static Finite Element Problems. *COMSOL BLOG*.
- Frei, W. (2013b). Which Turbulence Model Should I Choose for My CFD Application? *COMSOL BLOG*.
- Homicz, G. F. (2004). Computational Fluid Dynamic Simulations of Pipe Elbow Flow. (August), SAND2004-3467.
- ISO Standard (2016). Water quality — Determination of turbidity (ISO 7027-1).
- Kaltenbacher, M. (2015). *Numerical Simulation of Mechatronic Sensors and Actuators 3ed*. Springer Berlin Heidelberg.
- Kamstrup (2004). Ultraflow 34 Kamstrup Datasheet.
- Kamstrup (2014). TURBUS application Inovation Fond. (Figure 1), 1–15.
- Kamstrup (2017a). Conversation with Sune Dupont and Jens Lykke Sørensen from Kamstrup A/S.
- Kamstrup (2017b). Email correspondence with Sune Dupont from Kamstrup A/S.
- Landau, L. D. & Lifschitz, E. M. (1987). *Fluid Mechanics second edition*.
- Linke, C. & Drusch, S. (2016). Turbidity in oil-in-water-emulsions - Key factors and visual perception. *Food Res. Int.*, 89, 202–210.
- Menter, F. R. (1993). Zonal Two Equation k-omega Turbulence Models for Aerodynamic Flows. *24th Fluid Dyn. Confrence Florida*.
- Morse, P. M. & Ingard, K. U. (1968). *Theoretical acoustics*.
- Pallarés, A., Fischer, S., France, X., Pons, M. N., & Schmitt, P. (2016). Acoustic turbidity as online monitoring tool for rivers and sewer networks. *Flow Meas. Instrum.*, 48, 118–123.
- Pierce, A. D. (1989). *Acoustics - An Introduction to its Physical Principles and Applications*. Acoustical Society of America.
- Pons, M.-N. & Dodds, J. (2015). Particle Shape Characterization by Image Analysis. In S. Tarleton (Ed.), *Prog. Filtr. Sep.* chapter 15. Oxford: Academic Press.
- Ringh, M. (2016). Plotting the Algebraic Residual to Study Model Convergence. *COMSOL blog*, (pp. 1–8).
- Sadar, M. (1999). TURBIDITY STANDARDS Technical. *Tech. Inf. Ser. - Bookl. No. 12*, (12), 7.

-
- Schmerr, L. W. (2016). *Fundamentals of Ultrasonic Nondestructive Evaluation*. Springer Series in Measurement Science and Technology. Cham: Springer International Publishing.
- Settnes, M. & Bruus, H. (2012). Forces acting on a small particle in an acoustical field in a viscous fluid. *Phys. Rev. E - Stat. Nonlinear, Soft Matter Phys.*, 85(1), 1–12.
- Silva, G. T. & Bruus, H. (2014). Acoustic interaction forces between small particles in an ideal fluid. *Phys. Rev. E - Stat. Nonlinear, Soft Matter Phys.*, 90(6), 1–11.